Entangling Nuclear Spins using Photoexcited Triplet States



Vasileia Filidou

St Peter's College

A thesis submitted for the degree of Doctor of Philosophy

at the University of Oxford

Michaelmas Term 2011

© Vasileia Filidou

St Peter's College, 2012.

Typeset in LaTeX 2_ε.

Entangling Nuclear Spins using Photoexcited Triplet States

Vasileia Filidou

St Peter's College

Michaelmas Term 2011

Abstract of a thesis submitted for the degree of Doctor of Philosophy

Entanglement is one of the most technologically important quantum phenomena and its controlled creation brings us a step closer to the realisation of a quantum computer. Hybrid electron and nuclear spin systems which combine long nuclear decoherence times with the high polarisation and rapid processing times of electron spins are considered reliable candidates for the representation of the fundamental building block of a quantum computer, the qubit. In the literature electron spins quite ofter play the role of a mediator which can access, manipulate and couple states with long coherence times, beneficial for storing quantum information.

Despite the fact that an electron spin can be a useful resource for nuclear spin systems, its permanent presence can be a source of decoherence. The use of transient photoexcited electron spins provide an additional advantage and once the operations which involve the electron spin are completed, the electron spin can decay and not interfere further with the evolution of the system.

In this thesis we report magnetic resonance experiments and density functional theory calculations for the demonstration of nuclear - nuclear entanglement using photoexcited triplet states. We study homonuclear and heteronuclear fullerene derivatives and we identify in each case the relevant parameters that can lead to high fidelity entangling operations. The hyperfine interaction in a homonuclear system is the key parameter which determines the degree of entanglement between the nucelar spins according to a recent theoretical proposal. We measure and calculate the hyperfine interaction in homonuclear systems with ^{13}C nuclear spins in order to prove the feasibility of this scheme. Further experiments on a fullerene system with two nuclear spins a

^{31}P and a ^{1}H show that entangling operations of high fidelity which involve the demonstration of CNOT gates, are possible within the lifetime of the triplet state.

Acknowledgements

During the summer of 2006 (the hottest until 2011!) I visited Oxford for the first time to work with Dieter Jacksh on a summer project. I was so amazed by Oxford that when my project came to an end, I knew it I wanted to come back one day and study in this University.

Five years later I thank Prof. Andrew Briggs for making this dream come true and for welcoming me in QIP. I would also like to thank him for making sure that I followed the right paths in order to succeed in my DPhil and for providing the support a student would require.

I am particularly grateful to my supervisor John Morton, it has been an honour to work with him. He inspired me and amazed me by his great knowledge, the insight he has in science and by being right, pretty much, every time. I want to thank him for showing me how proper research is done, for his patience and for being fair. I would also like to thank my third supervisor, Arzhang Ardavan for his great ideas and useful discussions. Apart from thanking them individually they deserve to be thanked for one more reason, for trusting me to undertake a theory project in parallel with my experimental work. For this project I am especially grateful to Feliciano Giustino. I want to thank him for accepting to supervise a D.Phil student three months after he had arrived in Oxford, for teaching me

abinitio calculations, for believing in me and for all the time he dedicated to our project. For this work I also thank Davide Ceresoli who became quickly familiar with the project and for his great contribution finalising the theory paper.

For all the intense work, the laughs and the fun times in the office, I would like to thank Muj, Richard, Rizvi, Hua and Thomas. Muj for being a real friend and for joining me in GBK, Richard for trying to teach me Fantasy football and for the EPR discussions, Rizvi for exchanging ideas on triplet states, Hua for putting up with us whenever we were being noisy and Thomas who was always willing to help. Also I would like to thank Volker (Carlo) for the laughs at conferences. A big thank you also goes to Stephanie for her contribution to the 'phosphine' paper. It was a pleasure to work with such an intelligent, determined and multi-skilled person (most of the time until 5 in the morning) listening to Metallica and eating prawn crackers.

I would also like to thank Steven for providing the great samples used in my experiments (and for storing some in the freezer), Marcus for his theoretical proposals, Richard and Guzman.

My friends back home, Aggeliki, Anastasio, Dionysia, Simeoni, Christos, Billy, Katerina deserve to be acknowledged for standing by me these all these years proving that friendship is stronger no matter what the distance and for making me feel every time I was going back home, like I hadn't never left.

I would also like to thank Simon for all the good times, his support and for not giving up in difficult times.

Last I would like to thank my parents for supporting me and for giving me strength and courage to continue chasing my dreams. I thank them for caring, for being there to hear my fears and my concerns, share my happiness and feel proud of my achievements. After all, where I am standing today, I owe it to them.

Contents

Acknowledgements **v**

1 Introduction **1**

1.1 Quantum Bits 2

1.2 Defining a qubit 4

1.3 Initialisation of the qubit state 4

1.4 Long coherence times 6

1.5 Universal quantum gates 7

1.5.1 Two-qubit gates and Entanglement 9

1.6 Qubit measurement 11

1.7 Coupling spins through a mediator 12

2 EPR and triplet states **17**

2.1 EPR principles 18

2.2 The rotating frame 19

2.3 Spin relaxation effects 21

2.4 Spectral broadenings 22

2.5 Pulsed EPR sequences . . . 23
2.5.1 The spin echo . . . 23
2.5.2 Rabi Oscillations . . . 24
2.5.3 Measuring T_1 and T_2 . . . 24
2.6 Electron Nuclear Double Resonance (ENDOR) . . . 25
2.7 The triplet state . . . 27
2.7.1 Spin Hamiltonian of the triplet state . . . 29
2.8 EPR in triplet states . . . 33
2.8.1 Triplet studies for structural characterization and relaxation kinetics . 34
2.8.2 EPR in the triplet state of fullerenes . . . 35
2.8.3 Triplet states and quantum information . . . 39

3 Density Functional Theory 41
3.1 Density Functional Theory . . . 42
3.2 Kohn-Sham method . . . 43
3.3 Defining E_{xc} . . . 44
3.3.1 Supercells . . . 45
3.4 Basis functions . . . 46
3.4.1 Self consistency . . . 49
3.5 Pseudopotentials . . . 49
3.5.1 Types of pseudopotentials . . . 51
3.6 Projector Augmented Wave (PAW) method . . . 51
3.7 Calculation of Hyperfine Parameters . . . 54
3.8 GIPAW . . . 55

4 Feasibility of scheme to entangle nuclear spins 59
4.1 Introduction . . . 59

4.2 Theoretical Proposal 60
4.3 Preparation 64
4.4 Characterisation 64
4.4.1 Electron spin echo experiments 64
4.4.2 Relaxation Kinetics 67
4.4.3 Hyperfine Studies 70
4.5 Ab initio calculations 70
4.6 Realization of the theoretical proposal 74
4.7 Conclusions 75

5 Hyperfine studies for nuclear entanglement in excited states 77
5.1 Introduction 77
5.2 Calculation of the hyperfine tensor from first principles 78
5.3 Core Polarization 79
5.3.1 Computational method 81
5.4 Calculations on the small radicals 81
5.5 Results and Discussion 82
5.5.1 HFI parameters of small molecules 82
5.5.2 Hyperfine Interaction in Fullerene Derivatives 87
5.6 Discussion 90
5.7 Conclusions 91

6 Demonstration of entangling gates using the triplet state of DMFPH 93
6.1 Sample preparation 94
6.2 Time-resolved spectroscopy 95
6.3 Relaxation Kinetics 101
6.4 Hyperfine interaction 103

6.5 DFT . . . 106
6.6 Relaxation Studies . . . 109
6.7 SEDOR . . . 111
6.8 Phase gates . . . 113
6.9 Summary of characterisation . . . 113
6.10 Quantum State Tomography . . . 114
6.11 Conclusions . . . 116

7 Conclusions **117**

References **121**

1

Introduction

The idea of a quantum computer emerged in the late 80s along with the realisation that the rentless progress of chip technology following Moore's law would break down due to quantum effects. Benioff [Ben82], Feynman [Fey82] and Deutsch [Deu85], laid the foundations of quantum computing and with their work underlined the importance of a computer that could efficiently simulate quantum processes. Despite the development of some simple algorithms based on quantum parallelism [Deu89], the lack of more profound applications limited progress towards building a quantum computer. A few years later Shor [Sho99] made a breakthrough when he demonstrated that a quantum computer can be used to

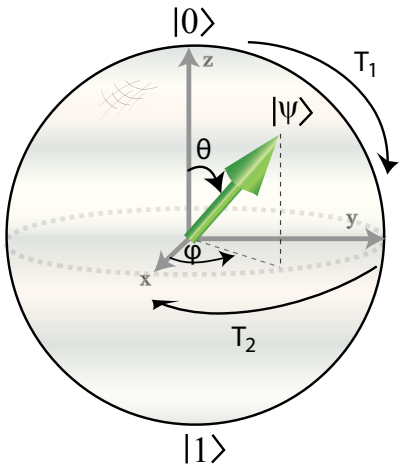


FIGURE 1.1: Bloch sphere representation of a qubit.

efficiently factor large numbers. Further evidence about the potential of quantum computers came a year later when Grover [Gro99] showed that database searches could be performed much faster in a quantum computer. Since then a widespread interest in the scientific community has lead to great progress, something that becomes apparent by noting the numerous architectures proposed for the implementation of a quantum computer. In each of these different architectures, the fundamental building block of the quantum computer is the quantum bit, or qubit.

1.1 Quantum Bits

In classical computers the unit of information is the bit, which takes the value 0 or 1. In a quantum computer the elements that carry quantum information are called quantum bits or qubits. The qubit, just like the classical bit, can exist in two possible states, $|0\rangle$ or $|1\rangle$. However, a qubit can also exist in a plethora of quantum states formed by linear combinations of the states $|0\rangle$ and $|1\rangle$, called superpositions. In general, the qubit can be

described by:

$$|\psi\rangle = \alpha|0\rangle + \beta|1\rangle \tag{1.1}$$

where a and β are complex numbers. The qubit is represented by a vector where the states $|0\rangle$ and $|1\rangle$, called computational basis states, define an orthonormal basis for this vector. A geometric representation of a qubit, shown Fig. 1.1, is known as the Bloch sphere. A point on the surface of the Bloch sphere is described by the state

$$|\psi\rangle = \cos\left(\frac{\theta}{2}\right)|0\rangle + \mathrm{e}^{\mathrm{i}\varphi}\sin\left(\frac{\theta}{2}\right)|1\rangle \tag{1.2}$$

where the angles θ and ϕ denote the orientation of the vector.

For description of an ensemble of quantum states, (i.e. a collection of independent identical quantum systems), we use the density matrix representation

$$\rho = \sum_i p_i|\psi_i\rangle\langle\psi_i| = \begin{pmatrix} \overline{|a|^2} & \overline{a\beta^*} \\ \overline{a^*\beta} & \overline{|\beta|^2} \end{pmatrix} \tag{1.3}$$

.

This matrix can, in general represent a mixed state, where each term is the weighted sum of states in pure superposition with the wavefunction ψ_k, i.e. $\overline{|a|^2} = \sum_i p_i|a|^2$. The diagonal elements of the density matrix are called populations while the off-diagonal elements, coherences. The sum of populations is always equal to one.

For the implementation of a qubit, a physical two level system is required. Systems under investigation include, among others, trapped ions [CZ02, Ste97], superconducting circuits [PGHM07], photons [CY95], electron and nuclear spins [Llo93, Kan98]. In this thesis we consider electron and nuclear spins as representations of qubits. In the following sections, we will see how such spins satisfy the basic requirements for qubits, known as the Di Vincenzo criteria.

1.2 Defining a qubit

The idea of the use of spins and particularly nuclear spins through nuclear magnetic resonance (NMR) arose in 1985 when Cory suggested an ensemble quantum computer. Nowadays, some of the most well known algorithms, (Shor' s, Grover's, Deutsch's algorithm) have been implemented using NMR.

Electron and nuclear spins are well-defined two-level systems with states $|\downarrow\rangle$ and $|\uparrow\rangle$ which correspond to the parallel or antiparallel alignment of the magnetic moments to an external magnetic field. The two states of an electron (nuclear) spin can be accessed and controlled by microwave (radiofrequency) irradiation.

Electron spin qubits exhibit large spin polarization compared to nuclear spins due to their larger gyromagnetic ratio. They can also be manipulated much more quickly than nuclear spin (leading to more rapid processing times for a quantum computing) but suffer from shorter decoherence times as they are more greatly affected by unwanted environmental interactions. On the other hand, the natural isolation of nuclear spins from the environment provides long decoherence times. Scaling up an NMR system to multiple qubits has been especially challenging due to the exponentially decreasing signal strength as the number of qubits grows (a result of the pseudo-pure preparation used to create initial states).

1.3 Initialisation of the qubit state

Before proceeding to the manipulation of the qubits, an essential requirement is their preparation into some well defined initial state. A natural choice for an initial state is the ground state, $|0\rangle$, which can be achieved by some cooling process that brings the system to its thermodynamic ground state.

In NMR, is impractical to cool the system down to low enough temperatures to achieve a

highly initialized ground state, as the Zeeman energy ΔE, between two nuclear spin states, which depends on their magnetic moment, is much smaller compared to $k_B T$. Therefore, in NMR, a thermally populated state is considered as the initial state. Although, a pure ground state is highly desirable, a "pseudo-pure" state which behaves in the same way as a pure ground state could be proven satisfactory [CFH96][1]. EPR does not suffer from this limitation as the larger magnetic moment of the electrons gives rise to a larger Zeeman energies which can exceed $k_B T$ and allow for the initialisation of the qubits into a pure state.

The enhanced electron spin polarization can be transferred to the nuclear spin by a family of techniques called Dynamic Nuclear Polarisation (DNP). The central idea behind these techniques, which are based on Overhauser's proposal [Ove53], is that the large Boltzmann polarization of unpaired electrons can be transferred to nuclei by the saturation of an EPR transition. For protons, the maximum enhancement is 660 and corresponds to the ratio of γ_e/γ_I.

Several continuous and pulsed DNP schemes have been proposed. Among these are the solid effect [AG78, DBD$^+$80], the integrated solid effect [HLSW90] and nuclear spin orientation via spin locking (NOVEL) [KLMT63]. High nuclear spin polarization can also be achieved via optically excited triplet states. This approach was successfully demonstrated in pentacene-doped naphthalene reaching enhancements of 2×10^5 times greater than the proton polarization limit [TTT04](see Chapter 2).

In a recent paper nuclear spin hyperpolarization was achieved by exploiting the different relaxation times of electron and nuclear spins in Si:P [SBR$^+$11]. The spin lattice relaxation T_1 of the donor electron in Si:P is much faster compared to the relaxation time of the nuclear spin. Initially, the electron thermal polarization is swapped to the nuclear spin and

[1]The pseudo pure state is the sum a small polarised component and an identity component which can be ignored (pseudo-pure approximation)

after a period of time, which is much larger than the relaxation time of the electron but shorter than the relaxation time of the nuclear spin, the electron spins are repolarised while the nuclear spins become hyperpolarized.

High electron spin polarisation can also be generated by optical pumping, as has been demonstrated in NV^- centers. The NV^- system possesses a spin-conserving optical excitation from the ground triplet state $^3A_2$, to the excited triplet state ^3E, at 637nm. Transitions between the $m_s = \pm 1$ sublevels of ^{3}E to an intermediate singlet state $^1A_1$, occur with high probability due to the higher rate of intersystem crossing compared to the state $m_s = 0$. Finally, state $^1A_1$ relaxes to $m_s = 0$. This spin selective decay path in combination with a few optical cycles preserves the electron spin state and generates polarisation greater than 88% in the $m_s = 0$ sublevel of the $^3A_2$ ground state [NKN+10, NBM06].

1.4 Long coherence times

Decoherence describes the degradation of a quantum state due to interaction of the system with the environment and is one of the main obstacles that needs to be addressed for the realisation of a viable quantum computer. The ratio of the decoherence time to the elementary operation time, is a relative measure of the operations that can be performed before unwanted coupling effects occur. This ratio can be as high as 10^7 for nuclear spins and 10^{13} for trapped ions [Bar96a] .

The decoherence times T_1 and T_2 describe processes which corrupt the desired evolution of the qubit. In the Bloch sphere representation, the decoherence time T_1 is described as the corruption of θ while T_2 describes the loss of phase information mapped in ϕ.

There are several strategies that can effectively elongate the decoherence times — these can be divided into two categories: 'passive' and 'active' . The active methods involve error correcting codes which have a two fold duty: to detect and correct computational errors (for

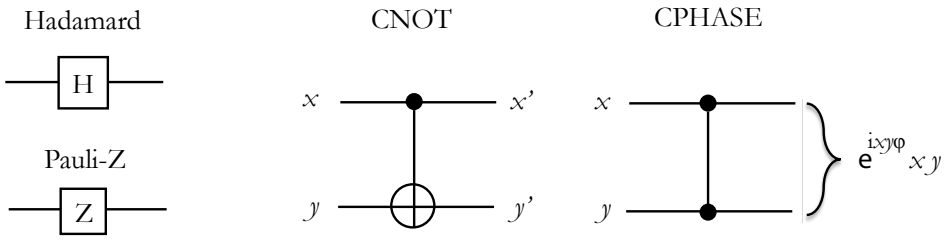


FIGURE 1.2: Circuit representation of single and two qubit gates. The black lines correspond to a wire that carries a single qubit.

example, qubit flips and phase errors [Sho95, Ste95]). An example of a passive method is the use of decoherence-free subspaces, where the qubits are encoded within subspaces which do not decohere due to the exploitation of symmetries in the evolution [LCW97, ZR97].

Between these two categories, there are methods that involve the design of gating processes stable against specific decoherence mechanisms [PCD+03] and dynamic decoupling schemes which make use of arrays of pulses to minimize unwanted interactions of the system with the environment [VKL99, Zan99]. An example of the first method will be given later on, in the last section.

1.5 Universal quantum gates

In classical computers, bits interact through gates which implement Boolean logic operations. The basic gates NOT (single bit) and OR , AND (two bits) form a complete set of gates, in such way that any logic operation can be performed by a combination of these three gates.

A quantum gate is a unitary transformation which acts onto the quantum states ($|1\rangle, |0\rangle$ or a superposition of the two) and takes the system from one state to another. It is convenient to describe quantum gates using a matrix representation written in the computational basis. Going back to the Bloch sphere representation, one-qubit gates can be implemented

as single spin rotations by the application of microwave or RF pulses. The power and the length of the pulse defines the rotation angle. Contrary to classical case where only one (non-trivial) single-bit gate exists, there is an infinite class of single-qubit logic gates including Pauli- X, Y, Z gates and the Hadamard gate H (Fig. 1.2).

The Pauli-X or (quantum-NOT) gate interconverts the qubit states $|0\rangle, |1\rangle$ and can be implemented by the application of a π pulse (a π rotation about the x axis.) The matrix which describes the Pauli-X gate is

$$X = \begin{pmatrix} 0 & 1 \\ 1 & 0 \end{pmatrix}. \tag{1.4}$$

The Pauli-Z gate is a particular case of a phase shift gate R which applies θ rotations about the z axis:

$$R = \begin{pmatrix} 1 & 0 \\ 0 & e^{i\theta} \end{pmatrix}. \tag{1.5}$$

Z gates are realised when $\theta = \pi$ and rotate the phase of the qubit around the z axis by π such that state $|0\rangle$ remains unchanged while the phase of state $|1\rangle$ is inverted.

The application of a Hadamard gate on a qubit takes the qubit state, $|0\rangle$ or $|1\rangle$ to a uniform superposition of states and is equivalent to the application of a $\pi/2$ pulse.[2]

$$|0\rangle \rightarrow (|0\rangle + |1\rangle)/\sqrt{2} \tag{1.6}$$

$$|1\rangle \rightarrow (|0\rangle - |1\rangle)/\sqrt{2} \tag{1.7}$$

Furthermore, the application of two Hadamard gates to the state $|00\rangle$ for example, yields the state $|00\rangle \rightarrow (|00\rangle + |01\rangle) + |10\rangle + |11\rangle)/\sqrt{2}$.

Although single spin rotations of nuclear spins are generally slow (in the tens of microseconds regime), they can be manipulated more quickly if coupled to an electron spin [MTA+06].

[2]The exact definition of a Hadamard gate is a $\pi/2$ rotation about y axis followed by a rotation of π around x axis.

For example, phase shifts can be introduced onto a nuclear spin through the application of selective microwave pulses which rotate one transition of the coupled electron spin. The application of a 2π microwave pulse introduces a global phase on the levels of the relevant electronic transition, leaving all populations unchanged. Depending on whether the microwave pulse is on resonance with the electronic transition, phase shifts of π (or less than π in the off resonance regime) will be applied on to the nuclear spin. The effectiveness of such phase gates was demonstrated while driving nuclear Rabi oscillations: the application of a number of phase gates under the presence of an RF pulse, suppresses the nuclear evolution and freezes the system in a particular state at will.

1.5.1 Two-qubit gates and Entanglement

Entanglement lies at the heart of quantum computing and is a peculiar form of correlation between two or more quantum systems which means that they cannot be described individually. Maximally entangled states of a two qubit system include the Bell states:

$$\Psi^{\pm} = \frac{1}{\sqrt{2}}(|\uparrow\downarrow\rangle \pm |\uparrow\downarrow\rangle) \qquad \Phi^{\pm} = \frac{1}{\sqrt{2}}(|\uparrow\uparrow\rangle \pm |\downarrow\downarrow\rangle) \tag{1.8}$$

Entangling operations, which create such states, have been the demonstrated in a number of systems like NV centers [TCT+10, NMR+08], endohedral fullerenes [MSW04], malonic acid crystals [MMS03], quantum dots [LWS+03], photons [RZB09] and donor spins in silicon [SBR+11].

Entanglement can be created by the application of CNOT gates (Fig. 1.2). The controlled-NOT or CNOT gate is a conditional two qubit gate meaning the operation performed on the second qubit depends on the state of the first qubit. The CNOT gate takes two inputs, x and y (which correspond to the control and the target qubits respectively), and produce two outputs x' , y'. The state of the first qubit is copied directly to the output

bit $x' = x$, while a NOT gate is applied to the second qubit only when the first qubit is in state $|1\rangle$. The CNOT gate is represented by the unitary matrix

$$U_{CNOT} = \begin{pmatrix} 1 & 0 & 0 & 0 \\ 0 & 1 & 0 & 0 \\ 0 & 0 & 0 & 1 \\ 0 & 0 & 1 & 0 \end{pmatrix}. \tag{1.9}$$

In NMR, a CNOT gate can be realized by a series of radiofrequency pulses which act on the control (A), and target (B), qubits [MDPC99]. Initially, a $\pi/2$ pulse rotates the B spin onto the xy plane which then precesses under the influence of the magnetic field of the control spin A. After a period of time, B picks up a phase shift of π which depends on the state of A. Another pulse of $-\pi/2$ brings B back to the $\pm z$ axis depending on the accumulated phase. In NMR, such spin couplings are typically permanently on. In order to overcome this issue refocusing schemes can be applied to reverse the time evolution and cancel out unwanted coupling effects [JK99, DWLY00].

CPHASE gates are also important in quantum computing as they create maximally entangled states by introducing phase changes on a particular basis state, leaving the other states unchanged. The C_{11} CPHASE gate is shown below and introduces a phase shift of ϕ when both qubits are in state $|1\rangle$[3]

$$C_{11}(\phi) = \begin{pmatrix} 1 & 0 & 0 & 0 \\ 0 & 1 & 0 & 0 \\ 0 & 0 & 1 & 0 \\ 0 & 0 & 0 & e^{i\phi} \end{pmatrix} \tag{1.10}$$

In the ideal case, a CPHASE gate applies a relative π phase shift to the state $|11\rangle$, so that the state changes its sign $|11\rangle \rightarrow -|11\rangle$.

[3]There are three more similar C-PHASE gates, C_{00}, C_{01}, C_{10} which apply a phase shift when the qubits are in the states $|00\rangle, |01\rangle, |10\rangle$, respectively.

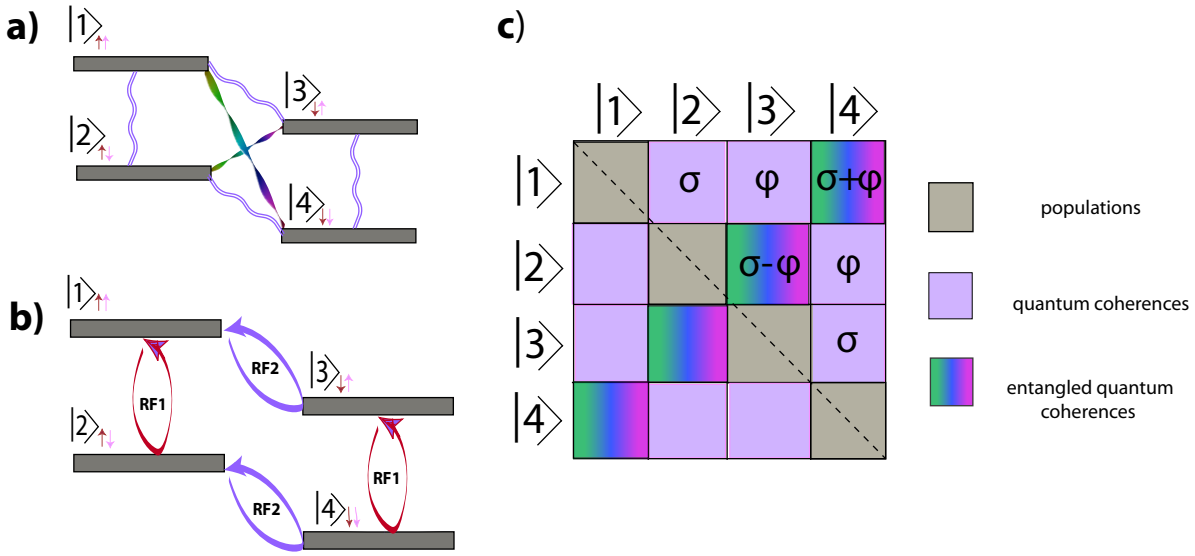


FIGURE 1.3: a) Illustration of the energy levels of a two-qubit system. The grey boxes represent the populations of the levels and the purple twisted lines the single-qubit coherences between them. The gradient coloured lines are represent the zero and double quantum coherences between the qubits. b) If the two qubits have different energy splittings, they can be independently driven using RF1 and RF2, as shown. Given a strong coupling between them, all four allowed transitions can be selectively addressed. c) Representation of the density matrix for this two-qubit system. The different colours denote the populations, the quantum coherences and the mutiple quantum coherences (zero or double). σ and ϕ show the relationship between the different phases acquired by the various coherences.

In the experiments described in Chapter 5 we will present two methods for implementing a CNOT gate in a heteronuclear fullerene system. The first directly exploits the J-coupling between two nuclear spins while the second makes use of CPHASE gates and Hadamard rotations.

1.6 Qubit measurement

Once the computation has been performed, a reliable measurement is required to readout the final quantum state. The fidelity of the measurement depends on factors such as decoherence and gate operation errors as well as errors related to the experimental setup, e.g.

inefficient photon counters. For spins, the measurement of single qubits is highly desirable but very challenging. Ensemble measurements which are performed simultaneously on a very large number of copies of the quantum computer is substantially easier, but has scaling limitations.

The result of a quantum algorithm is determined by single measurements on the various qubits, however in order to fully map out the effect of various quantum gates it is necessary to extract the full density matrix of a multi-qubit system through a series of sequential measurements, known as quantum state 'tomography' [SM08].

Quantum tomography of an electron-nuclear spin density matrix was used to demonstrate entanglement in P-doped Si [SBR$^+$11]. In that work, the diagonal elements of the density matrix, the populations, were mapped to observable EPR spin echo amplitudes. In order to improve the fidelity of the coherences, phase shifts were applied to the two qubits at some well-defined rate, such that the multiple quantum coherences acquired phase at the sum or difference of these rates, as shown in Figure 1.3.

1.7 Coupling spins through a mediator

The difficulty of controlling spin couplings directly, gave rise to proposals which incorporate intermediate objects to couple neighbouring spin qubits. In these proposals, the intermediate system can play the role of a switch that turns on and off the interactions when needed, providing an additional degree of control.

Following such ideas, all-optical spin-based QIP has been proposed using the spin of an excess electron contained in InAsGaAs arrays of quantum dots [CDF$^+$03, PBC$^+$03]. The two qubit states $|0\rangle, |1\rangle$ represent the two spin states of the conduction band electron. The gating between two quantum dots is achieved through optical excitation of electron-hole pairs which, under the presence of an external electric field, acquire a dipole moment that

permits interactions with each other (Fig. 1.4a). The two-qubit gating time is in the picosecond range as determined by the dipole-dipole interaction. The ability to switch on/off the excitonic states is based on the Pauli blocking effect, which acts as a spin-dependent mechanism. In the ideal case where only one state is perfectly selective, coupling to the excited state turns on the interaction between the quantum dots when the qubits are in the state $|11\rangle$. Despite the fact that spins in quantum dots appear robust against decoherence, two possible mechanisms, the hole mixing and the phonon coupling are responsible the loss of coherence. A later study, which is based on the above proposal, demonstrates the impact of each individual decoherence mechanism to single and two qubit gates and proposes a method to bypass these effects by using an adiabatic laser excitation scheme [PCD$^+$03]. Similar studies are carried out in Reference [NLB$^+$04] and a CPHASE gate is implemented by exploiting the intra-dot Föster coupling.

Defects in semiconductors have also been proposed to generate mediated coupling through an optically excited electron spin. Stoneham *et al.* [SFG03] proposed a scheme for entangling deep donor spins in silicon, where qubit interactions can be turned on and off through a control electron. The qubits and the control electron don't interact in the ground state but in the excited state an effective exchange interaction between the qubit spins is activated (Fig. 1.4b). The interaction can be turned off by stimulated de-excitation of the control electron. Although this proposal is quite interesting its feasibility is limited to specific parameter regimes.

These have been generalised and shown to be applicable to molecules with coupled electron and nuclear spins [GRSL08]. In this study two cases are considered: the first involves a dynamic excitation and de-excitation while the other operates adiabatically so that the laser intensity changes slowly. In the first case, it is found that even an unequal coupling can maximally entangle the two states contrary to what is proposed in the previous scheme, which is only valid for systems of equal coupling to the mediator. In the second case,

a less constrained system is considered and it is demonstrated that any coupling realises the proposal. In both cases maximally entangling gates are presented and the entangling power as a function of the coupling strengths is shown in Figure 1.4c.

A parametric tunable coupling of optimally biased superconducting qubits is discussed in [NHY$^+$07]. The effective coupling between the intial qubits is induced via use of a third qubit of higher energy difference. The coupling is the sum of the inductive coupling between the qubits and the indirect coupling through the inductance of qubit 3 (Fig. 1.4d). Two-qubit operations are possible through the application of microwaves at either the sum or the difference frequency transition between qubits 1,2 (Fig. 1.4d). The application of a microwave can switche the coupling on and off. Other techniques involve the use of an electrostatic transformer which provides a gate-voltage controlled coupling of two Josephson charge qubits [AB03].

Recently, two proposals have been described which exploit a photoexcited mediator to entangle two nuclear spins which do not interact directly [SLG11a]. In the first case (the 'symmetric' case, discussed in detail in Chapter 3) the nuclear spins couple with equal strengths to the mediator. The other case refers to asymmetric systems with different nuclear spins and/or different hyperfine interaction strengths. Although the first case relies on the free time evolution of the system for the creation of entanglement, in the asymmetric case a suitable sequence of radio-frequency and microwave control pulses is applied. Furthermore, the decay to the ground state for an asymmetric system invariably destroys the nuclear coherences, unless controlled de-excitation is performed. Entanglement in the asymmetric case can be performed through a dynamic approach (by the application of a single 2π pulse) or an adiabatic approach, in a similar way as in [GRSL08]. A third approach for the generation of a Bell state is described below (see Fig. 1.4e) and belongs to the dynamic methodology.

Assuming that the initial spin state is in the triplet T_0 state on the nuclear subspace

$|\downarrow\downarrow\rangle$, the application of a microwave $\pi/2$ pulse generates a coherence between the $|T_+\downarrow\downarrow\rangle$ and $|T_0\downarrow\downarrow\rangle$. The application of two successive π pulses on the nuclear subspace of the T_0, transfer the coherence from $|T_0\downarrow\downarrow\rangle$ to the state $|T_0\downarrow\uparrow\rangle$ and finally the state $|T_0\uparrow\uparrow\rangle$. The last microwave pulse moves the coherence entirely to the T_0 triplet state, resulting a Bell state $1/\sqrt{2}(|T_0\downarrow\downarrow\rangle + |T_0\uparrow\uparrow\rangle)$. This approach is practically challenging, as it relies on the coherence time T_2 of the triplet electron spin being long compared to the nuclear spin π pulse duration.

In this thesis, I examine the practical implementation of such optically-mediated nuclear spin coupling using molecular systems, through a combination of density functional theory calculations, combined with EPR and NMR experiments on triplet states of fullerene derivatives.

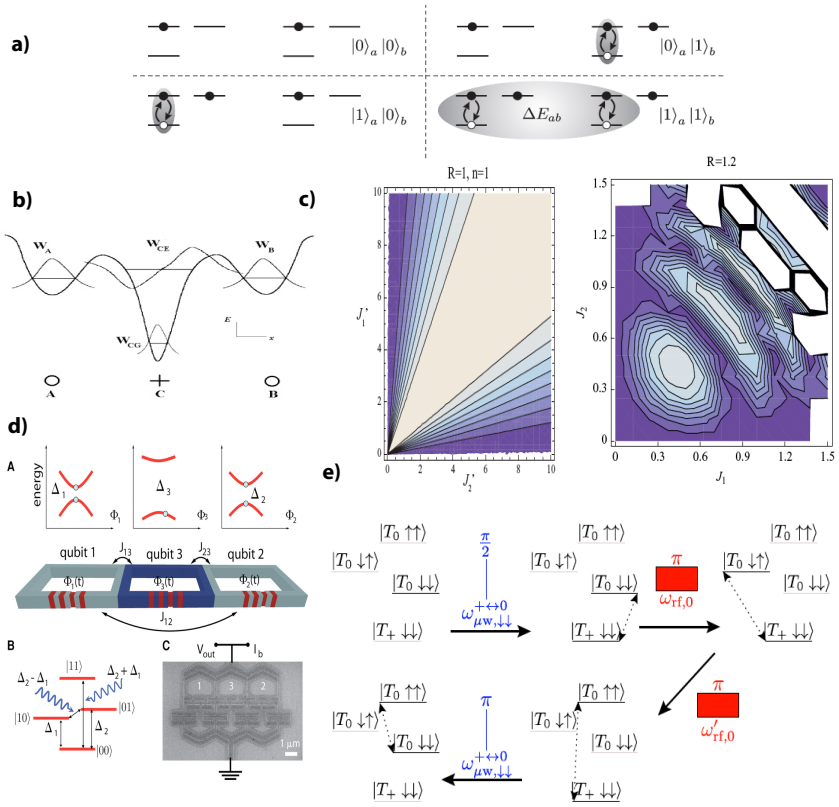


FIGURE 1.4: a) An illustration of a two-qubit gate using an auxiliary state. In the ideal case of an efficient spin selective Pauli blocking the effective dipole-dipole coupling is activated only if the excess electrons in both QDs are in state $|11\rangle$.(From [EUROPHYSICS LETTERS 2003, Europhys. Lett., 62 (2), pp. 175181 (2003), Spin-based optical quantum computation via Pauli blocking in semiconductor quantum dots, E. Pazy, E. Biolatti, T. Calarco, I. DAmico, P. Zanardi, F. Rossi and P. Zoller], Reprinted with permission from EPL) b) Schematic representation of the wavefunctions of the spin qubits of the donors A, B and the control atom C. In the ground state the control electron doesn't interact with the donors. Upon excitation the control electron is in a charge transfer molecular like state and overlaps with both electrons creating entanglement. From [A.M. Stoneham, A. J. Fisher and P. T. Greenland, Institute of Physics Publishing Journal of Physics: Condensed Matter, 15 (2003) L447L451, PII: S0953-8984(03)64964-7, Optically driven silicon-based quantum gates with potential for high-temperature operation]. Reprinted with permission from IOPP) . c) Average entangling power of the two qubit gates in the dynamic (left) and adiabatic (right) regime with respect to the exchange coupling. In the dynamic case the most entangling region is along the diagonal where $J_1 = J_2$. In contrast, in the adiabatic gate an oscillatory motion is observed. The behaviour reflects the way that phase accumulates. From [E. M. Gauger, P. P. Rohde, A. M. Stoneham, and Brendon W Lovett. New Journal of Physics, 10, 073027, (2008), DOI : 10. 1088/1367-2630/10/7/073027, Strategies for entangling remote spins with unequal coupling to an optically active mediator]. Reprinted with permission from IOPP) d) The system consists of three qubits. Qubits 1,2 with energies Δ_1 and Δ_2 are coupled to the third qubit of higher energy Δ_3. The level diagram of qubits 1 and 2 is also presented and the two qubit operations are performed using microwaves at the sum or the difference of their frequencies. (From [A. O. Niskanen, K. Harradi, F. Yoshihara, Y. Nakamura, S. Lloyd and J. S. Tsai, *Science*, Vol. 316 no. 5825 pp. 723-726, DOI: 10.1126/science.1141324 Quantum Coherent Tunable Coupling of Superconducting Qubits]. Reprinted with permission from AAAS). e) Pulse sequence for the generation of a Bell state. The black energy levels are populated while the grey ones are empty. The dotted arrows represent the coherences. [Reprinted with permission from PRA]

2

EPR and triplet states

Electron paramagnetic resonance (EPR) is a spectroscopic technique widely used for the evaluation of the structural information and the dynamics of species with unpaired electrons. EPR has applications in chemistry, biology, medicine and physics, involving studies of radicals, transition metal ions, defect centres and impurities in semiconductors. In this Chapter we describe the basic EPR principles and present EPR studies in photoexcited triplet states. We give a detailed description of the triplet state of the fullerene C_{60} and finally we discuss the possibility of using triplet states in quantum computing schemes.

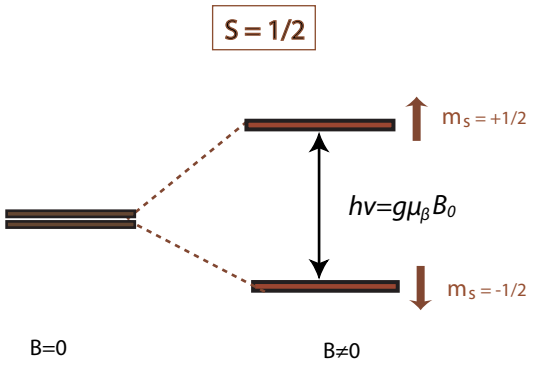


FIGURE 2.1: a) Schematic representation of the Zeeman effect in a $S = 1/2$ system. At zero field the spin states have the same energy. Upon the application of a magnetic field the levels split with an energy difference which is proportional to the intensity of the magnetic field B_0.

2.1 EPR principles

The basic requirement for EPR is the presence of unpaired electrons with total spin of $S \geqslant 1/2$. For a spin $S = 1/2$ system, the presence of a magnetic field B_0, causes the magnetic moments μ, to align parallel or antiparallel to the field creating two distinct energy levels, with energy difference of $\Delta E = g\mu_B B_0$ (Zeeman effect).

The application of an additional oscillating microwave magnetic field B_1, perpendicular to the static field, induces transitions between these two levels when the resonant condition is met (microwave photon energy $h\nu$ is equal to the Zeeman energy splitting between the two sublevels ΔE (Fig. 2.1).

Due to large the magnetic moment of an electron, a microwave frequency in the order of 3 - 100 GHz is required to fulfil the resonance condition for typical magnetic fields 0.1 to 5 T. Using 10 GHz (X-band), which is a standard frequency in many EPR spectrometers and for a g-factor of 2.0023 (free electron), the magnetic field is 0.35 T. Other bands like Q-band and W-band correspond to higher frequencies of 34 GHz and 95 GHz, respectively. The resonance condition in a typical EPR spectrometer is achieved by varying the magnetic field

at a fixed microwave frequency. The reverse is also possible, where the frequency is varied at a fixed magnetic field, but is not widely applied due to the use of a narrow-bandwidth microwave resonator.

EPR experiments can be conducted in two modes, continuous wave (CW) and pulsed. In continuous wave (CW) experiments, microwave irradiation is applied continuously while the external magnetic field is swept until the resonance condition is matched. The CW spectrum is recorded as the derivative of the absorption curve (and not the absorption directly) with respect to the magnetic field intensity. The CW spectrum gives an insight into the splittings of the energy levels of the electron spin but lacks resolution compared to pulsed methods, as well as the ability to manipulate the electron spin state through coherent control. Time resolved EPR is also CW without field modulation (more details about this method will be given in chapter 6.)

In a pulsed EPR experiment, high power microwave pulses are applied to the sample to drive the spins out of equilibrium. In this case, the signal arises from the weak microwave signal emitted from the spins precessing in the static magnetic field. Pulsed EPR experiments are best understood by considering a reference frame rotating at the microwave frequency.

2.2 The rotating frame

The spin properties of macroscopic systems are described by the magnetisation M, a vector which represents the sum of the magnetic moments of the individual electron spins

$$M = \sum \mu_i \tag{2.1}$$

The time evolution of the magnetization at any magnetic field is given by the following

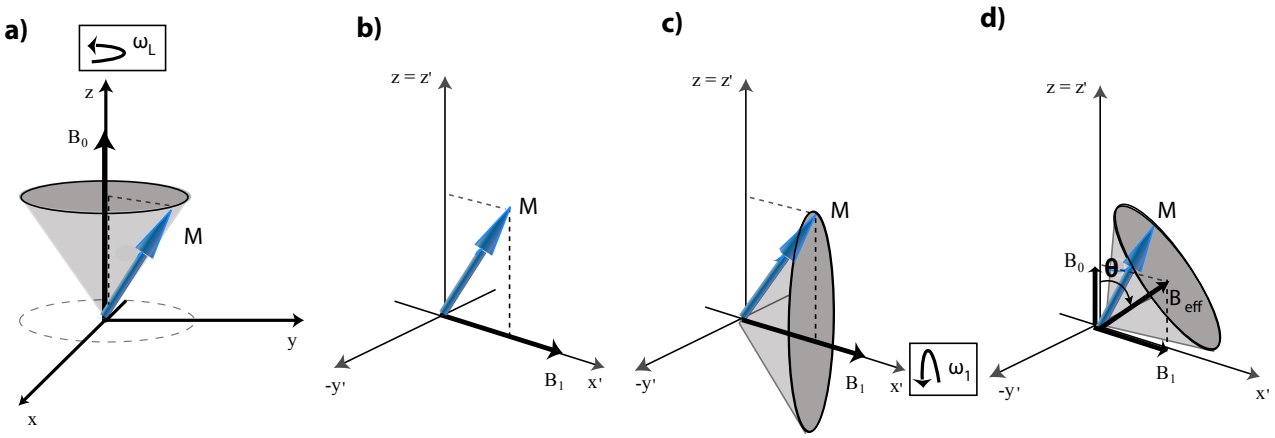


FIGURE 2.2: a) The magnetization vector M precesses around a magnetic field B_0 with the Larmor frequency ω_L. b) A reference frame (x', y', z') which rotates around the z axis at the same frequency as the magnetization, sees the magnetization M stationary. c) The application of a magnetic field B_1 perpendicular to B_0 which rotates with the Larmor frequency causes the magnetization to presess around B_1 at a frequency ω_1. d) When B_1 doesn't rotate at the exact Larmor frequency the magnetization precesses at an effective field B_{eff} tilted by an angle θ with respect to the z axis.

equation

$$\frac{dM}{dt} = M \times g\mu_B B \tag{2.2}$$

In the presence of a static magnetic field the magnetisation M rotates around the z axis at an angular frequency, ω_L, the Larmor frequency (Fig. 2.2a):

$$\omega_L = g\mu_B B/\hbar, \tag{2.3}$$

The spin system experiences, in addition to the static magnetic field, an oscillating microwave magnetic field B_1 perpendicular to the z axis with components:

$$B_{1,x}(t) = B_1 \cos(\omega t) \tag{2.4}$$

$$B_{1,y}(t) = B_1 \sin(\omega t) \tag{2.5}$$

$$B_{1,z}(t) = 0 \tag{2.6}$$

where ω is the microwave frequency. The application of both fields complicates significantly the motion of the magnetisation. In order to understand the behaviour of the individual components we make use of the rotating frame, along with the rotating wave approximation (RWA), such that the B_1 field becomes time independent.

In the rotating reference frame (given by coordinates x', y', z') we consider that x', y' rotate around z with frequency ω, while $z = z'$. In this frame, the magnetisation precesses about the z' axis at a much lower frequency given by the detuning $\Omega_s = \omega_L - \omega$. In the simple case where $\omega_L = \omega$ the field along B_0 vanishes and B_1 is now static. The magnetisation then precesses around B_1 with frequency ω_1 (Fig. 2.2c)

$$\omega_1 = g\mu_B B_1/\hbar. \tag{2.7}$$

If the Larmor frequency does not coincide with the microwave frequence ω the magnetization precesses at an effective field B_{eff} with frequency $\omega_{eff} = \sqrt{(\Omega_s)^2 + \omega_1^2}$ tilted by an angle $\theta = tan^{-1}(\frac{\omega_1}{\Omega_s})$ with respect to the z axis (see Fig. 2.2d).

2.3 Spin relaxation effects

The motion of the magnetisation vector in the rotating frame is described by the Bloch equations

$$dM_z/dt = M_y\omega_1 - (M_z - M_0)/T_1 \tag{2.8}$$

$$dM_x/dt = -M_y(\omega_L - \omega) - M_x/T_2 \tag{2.9}$$

$$dM_y/dt = -M_z(\omega_1) - M_x(\omega_L - \omega) - M_z/T_2 \tag{2.10}$$

There are two physical processes that drive the spin magnetisation M towards its equilibrium state. The first is called the spin-lattice, or longitudinal, relaxation time T_1 and

is related to the dissipation of energy via the thermal vibrations of the lattice (i.e. spin-phonon coupling). The relaxation time T_1 shows how quickly the M_z magnetisation recovers towards its thermal equilibrium value ($+z$), causing the M_x and M_y magnetic components to vanish

$$M_z(t) = M_z(0)(1 - 2e^{-\frac{t}{T_1}}) \tag{2.11}$$

The second relaxation mechanism, the transverse relaxation T_2 corresponds to the decay of the M_{xy} component caused by the spin flip-flops and arises from the dipolar and exchange interactions between spins in the sample

$$M_{xy}(t) = M_{xy}(0)e^{-\frac{t}{T_2}} \tag{2.12}$$

2.4 Spectral broadenings

The linewidth of an EPR transition can be determined by homogeneous, or inhomogeneous broadening. A homogeneously broadened line arises from magnetically equivalent spins of the same Larmor frequency. This leads to a Lorentzian EPR lineshape whose width is inversely proportional to the T_2 relaxation time (assuming $T_2 \ll T_1$).

A number of mechanisms are responsible for inhomogeneously broadened lines. The unresolved hyperfine couplings of an electron with many nuclear spins is one of the main sources of an inhomogeneously broadened line. Different spin environments can lead to variation in some parameter in the spin Hamiltonian (such as the g-tensor) which also leads to inhomogeneous broadening. For narrow EPR lines, the presence of an inhomogeneous external magnetic field, can also affect the linewidths. Finally, in randomly oriented systems with spin anisotropy, like the ones studied in this thesis, the EPR spectrum is considered as a broad inhomogeneous line arising from molecules at different orientations. Typically an inhomogeneously broadened spectrum has a Gaussian lineshape.

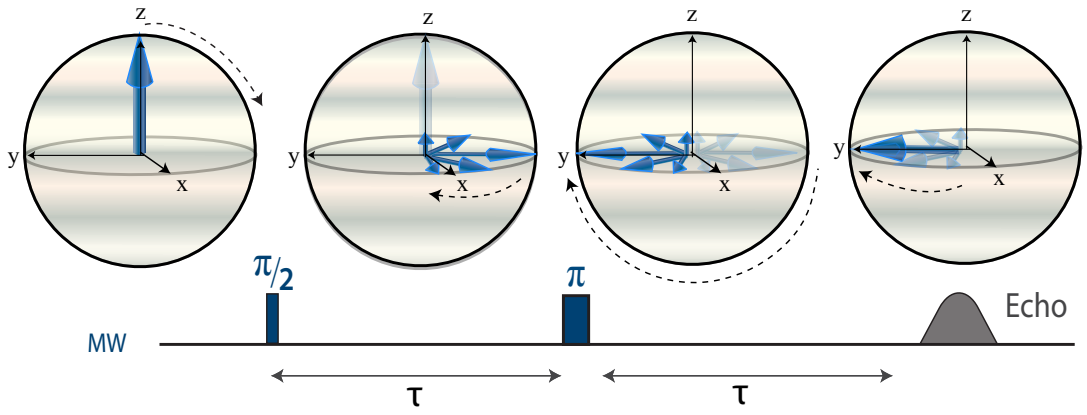


Figure 2.3: a) The Hahn echo experiment. Initially the spin packets are aligned with the magnetic field. The application of a $\pi/2$ pulse brings the magnetization to the xy plane where the spin packets start fanning out. A subsequent π pulse is applied after time τ which inverts the direction of the spins. The inversion pulse refocuses the spins and after another time interval τ an echo is formed.

2.5 Pulsed EPR sequences

Pulsed EPR involves the application of a sequence of pulses developed for the extraction of a particular structural or dynamic parameter of the paramagnetic compound under investigation. The development of pulse sequences requires an in-depth understanding of the evolution of the spins as series of pulses can generate signals irrelevant to the parameter we intend to measure.

2.5.1 The spin echo

The basic pulsed EPR experiment is the two-pulse Hahn echo (Figure 2.3). The first microwave pulse converts the longitudinal magnetization to transverse magnetization in the xy plane. The spins then start to dephase in the xy plane but the application of a π pulse after time τ, inverts their direction and consequently the phase of each spin packet, so at the end of another time interval τ all the spins converge. This convergence corresponds

to an observable transverse magnetization, the spin echo. The spin echo can be recorded at different magnetic fields yielding a field-swept electron spin echo (FS-ESE) and the acquired spectrum provides information about the characteristics and the interactions of the spin system, similar to the absorption spectrum whose first derivative is measured in CW EPR.

2.5.2 Rabi Oscillations

The spin precession upon the application of a transverse microwave field produces an oscillatory motion in the z-magnetization known as Rabi oscillations. The Rabi oscillations depend on the resonant condition of the static magnetic field with the microwave B_1 field. In the resonant condition we observe a full inversion of the magnetisation from the $+z$ and $-z$ orientation and back. In the off-resonant condition the oscillations are not complete and evolve in smaller cycles on the Bloch sphere.

We perform Rabi oscillations on the electron spin by varying the duration of the first pulse in a Hahn echo experiment. The observation of Rabi oscillations is one of the initial tests we perform to demonstrate the control we have over the electron spins under microwave pulses of certain magnitude and the duration. In a similar way we can also observe Rabi oscillations of a nuclear spin by varying only the duration of the radiofrequency pulse, using the ENDOR sequences described below.

2.5.3 Measuring T_1 and T_2

The relaxation time T_1, is measured by a technique called inversion recovery ($\pi - T - \pi/2 - \tau - \pi - \tau - echo$). In this pulse sequence, the role of the first π pulse is to invert the initial magnetization. The inversion pulse is applied at a fixed time before a Hahn echo measurement while the Hahn echo sequence and the detection window are shifted by a time delay T. The T_2 relaxation time is extracted by varying the time τ between the two pulses

in a Hahn echo experiment and the decay time corresponds to the time required for the magnetization to decay in the xy plane. The relaxation time T_1 is usually longer than T_2.

2.6 Electron Nuclear Double Resonance (ENDOR)

ENDOR complements EPR, as it provides a way to measure the response of nuclear spins by transferring the polarisation of the electron spins to a nuclear subspace. As with EPR, ENDOR can be conducted in continuous wave (c.w) and pulsed modes. In both types of experiments the magnetic field is kept constant and the EPR signal is plotted as a function of the radiofrequency, (RF).

In CW ENDOR, an EPR transition is partially saturated while a second (frequency-swept) RF irradiation excites nuclear spin transitions. The intensity of CW ENDOR depends on a balance among the relaxation pathways of the electron and the nuclear energy levels.

Pulsed ENDOR experiments can be performed in short timescales compared to CW ENDOR, this is advantageous as the experiment time doesn't exceed the spin relaxation times and systems with short relaxation times can be studied. An ENDOR measurement is made at selected field positions in an FS-ESE spectrum.

In pulsed ENDOR experiments, two pulse sequences are primarily used, those due to Davies [Dav74] and Mims [Mim65]. In a Davies experiment the first microwave pulse inverts the polarization of one EPR transition while a selective RF π pulse, inverts the polarization of an NMR transition (Fig. 2.4a). This has an effect on the electronic spin polarization (as the RF pulse equalizes the populations) causing a decrease in the inverted echo. The radiofrequency is swept and upon resonance the decrease of the inverted echo is measured via an electron spin echo pulse sequence. The effect of the radiofrequency excitation on the echo intensity is defined by the 'ENDOR efficiency'

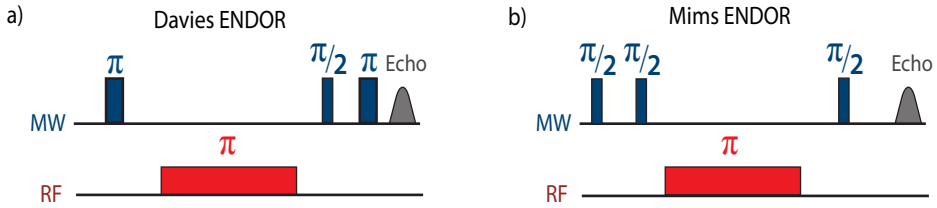


FIGURE 2.4: a) Davies ENDOR pulse sequence. A Davies ENDOR experiment is similar to an inversion recovery experiment: the first microwave pulse inverts the electron spin magnetization and an RF pulse is applied thereafter. The ENDOR signal, which is detected via a Hahn echo sequence as RF is swept, corresponds to the partial recovery of the inverted echo. b) Mims ENDOR pulse sequence. The Mims ENDOR is a stimulated echo experiment ($\pi/2 - \tau - \pi/2 - T - \pi/2 - \tau - echo$) in which an RF pulse is applied during the delay period T. The application of an RF pulse changes the resonance frequency of an electron spin that is coupled to a nuclear spin. The ENDOR signal again reveals the decrease of the echo intensity upon the application of the RF pulse.

$$F_{ENDOR} = \frac{1}{2}|[I_e - I_e(RF)]/I_e| \tag{2.13}$$

I_e corresponds to the intensity of the echo in the absence of an RF pulse and $I_e(RF)$ is the intensity of the echo upon the application of the RF pulse. The range of the ENDOR efficiency is from 0 to 1 and $F_{ENDOR} = 1$ corresponds to the inverted echo.

By performing an inversion recovery experiment we are able to determine the available time to apply radiofrequency pulses and invert the nuclear polarization. The length of a radiofrequency pulse is given by $t_p = \frac{\pi}{\gamma_N B_2}$ where t_p is the pulse length, γ_N the nuclear gyromagnetic ratio and B_2 the RF magnetic field. The optimum RF pulse can be determined by nuclear Rabi oscillations. The echo will oscillate with $I_{echo} \sim 1 - \cos(\gamma_N B_2 t_p)$ and the first minimum indicates the length of the π pulse. Typical lengths of RF pulses are in the order of tens of μs and depend on the RF amplifier used in the experiment.

For a successful Davies ENDOR experiment an important requirement is the inversion of one of the two electronic transitions. In order to achieve that, we use to long (frequency-selective) pulses to help ensure that the excitation bandwidth of the pulse is narrower than

the hyperfine splitting.

In a Mims ENDOR experiment three non-selective $\pi/2$ microwave pulses are applied forming a stimulated echo, while the π radiofrequency pulse is applied after the second microwave pulse (Fig. 2.4b). The first two microwave $\pi/2 - \tau - \pi/2$ pulses result a polarization grating in the M_z magnetisation with period $1/\tau$ while the last $\pi/2$ pulse brings the magnetization back to xy plane where the stimulated echo is created. The RF pulse frequency is swept and upon resonance with the nuclear transition, the change in the polarisation pattern of the two microwave pulses is recorded. In a Mims experiment the ENDOR efficiency depends on the hyperfine coupling and the time τ. Mims ENDOR is more sensitive to small couplings, but is less quantitative due to blind spots, while Davies ENDOR is better for larger couplings.

2.7 The triplet state

Most organic molecules have an even number of electrons and closed shell singlet electronic ground states S_0. When an electron is promoted from a doubly occupied orbital to a vacant orbital of higher energy the two unpaired electrons give rise to singlet or triplet excited states depending on if their antiparallel or parallel. A schematic representation of the energy level diagram is shown in Figure 2.5.

A photon excites the system from the ground state S_0 to the first excited singlet state through a mechanism called intersystem conversion (IC), which involves transitions between states of the same multiplicity. From the first excited singlet state the levels of the lowest excited triplet state (T_x, T_y and T_z) are populated via a process called intersystem crossing (ISC). The ISC is a non-radiative passage between states of different multiplicity and originates from the spin-orbit coupling. Usually the ISC rates are within the range of 10^4 – 10^{12} s^{-1} [GAK69]. Since any transition between states of different multiplicity

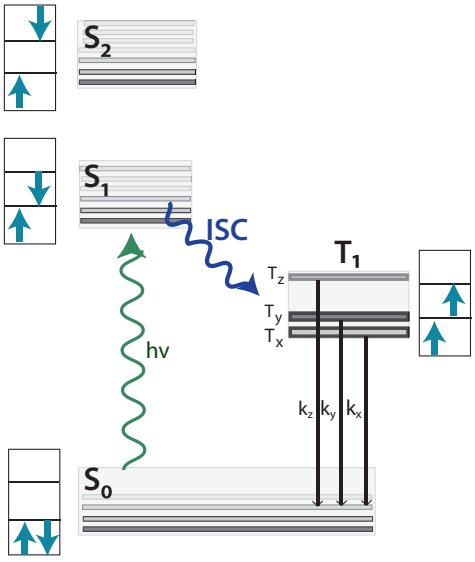


FIGURE 2.5: a) Energy level diagram of the triplet state. The arrows in the grey boxes represent the possible configuration of the spins in occupied and unoccupied orbitals. The laser pulse ($h\nu$) excites the molecules into the first excited singlet state which relaxes through ISC to the first excited triplet state T_1. The ISC crossing populates the triplet sublevels T_x T_y and T_z which decay to the singlet state with rates k_x, k_y and k_z. An additional T_1 relaxation mechanism between the sublevels (not shown here) relaxes further the triplet sublevels though this can be much longer than the lifetime of the triplet state and in such cases, ignored.

is highly forbidden the lowest triplet state is often long-lived (for example the lifetime of triplet state of napthalene at 77 K is in the order of seconds [HM61]). The lifetime of triplet states allows their study via electron paramagnetic resonance.

Studies of the lowest triplet state of crystal structures, which provide an excellent orientation selection, uniaxial media such as nematic liquid crystals and randomly oriented frozen solutions will be discussed in the following sections. The work in this thesis focuses on the study of randomly oriented frozen solutions.

A typical FS-ESE triplet spectrum of a disordered powder consists of inhomogeneously broadened lines where at each field position of the spectrum, signal arises from spins of molecules with different orientations with respect to the applied field (see for example

Fig. 2.6, measured using the phosphine oxide fullerene, DFMPH). The orientation dependence creates characteristic peaks which correspond (in general) to a magnetic field parallel to one of the three principal axis of the triplet. These are called 'canonical orientations'. For example, in a triplet spectrum with four characteristic peaks (marked with * in Fig. 2.6), the edges correspond to molecules with their z-axis parallel to the magnetic field, while at the inner maxima the x, or y axis is parallel to the magnetic field. The presence of six peaks [KGTW01], assigns every peak to one canonical orientation.

From an FS-ESE spectrum we can directly extract information about the zero-field splitting parameters (ZFS), D, E and the polarization of the triplet state (Fig. 2.7). Figure 2.6 reveals that the triplet levels are polarized in absorption at low fields and in emission at high fields with a non Boltzmann population distribution.

2.7.1 Spin Hamiltonian of the triplet state

For a complete understanding of the structural parameters and the interactions that govern a spin system in the triplet state, we need to extract the terms of the spin Hamiltonian.

The first term is the electronic Zeeman interaction, which describes the interaction of an electron spin with the magnetic field. Often this is the dominant term, describing the splitting of the electron spin sub-levels.

$$H_{EZ} = \mu_B B.g.S \tag{2.14}$$

μ_B is the Bohr magneton, B is the static field vector, g, is the g tensor a second rank tensor with principal values g_{xx}, g_{yy} and g_{zz} and S is the total spin vector.

In a system with more than one unpaired electron, the zero field splitting term (ZFS) represents the interaction between the electron spins

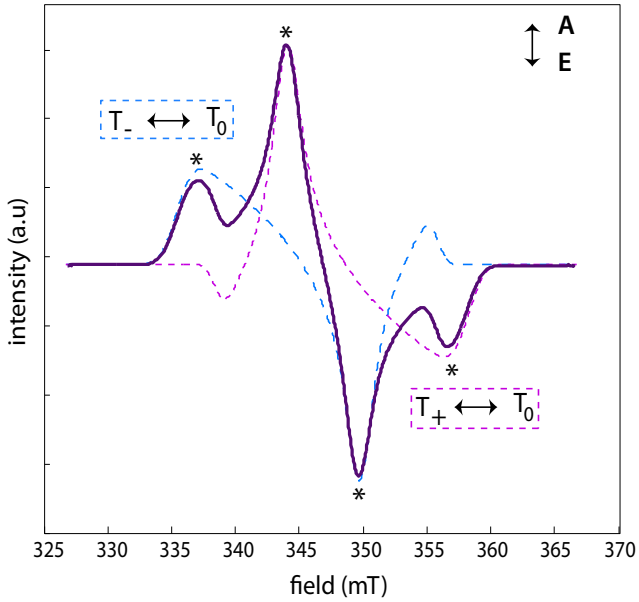


FIGURE 2.6: FS-ESE spectra of the phosphine oxide fullerene (DFMPH). The spectrum has an absorption/ emission pattern. The lineshape of the spectrum is a combination of two transitions marked with dashed blue and pink traces. The peaks marked with * correspond to molecules with their canonical orientations oriented parallel to the magnetic field.

$$H_D = S.D.S \tag{2.15}$$

D is a symmetric tensor called the zero field splitting tensor. In terms of the principal axes, this term of the Hamiltonian term can be characterised by two independent constants, the zero field splitting parameters, D, E (for the case of two $S = 1/2$ spins):

$$H_D = D\left(S_{zz}^2 - \frac{1}{3}S(S+1)\right) + E\left(S_{xx}^2 - S_{yy}^2\right) \tag{2.16}$$

where $D = 3D_{zz}/2$ and $E = (D_{xx} - D_{yy})/2$.

A non-zero value of the D term indicates that the system under consideration does not have spherical symmetry while E quantifies the deviation from axial symmetry. The sign of the zero field splitting D provides information about the order of the triplet sublevels. For

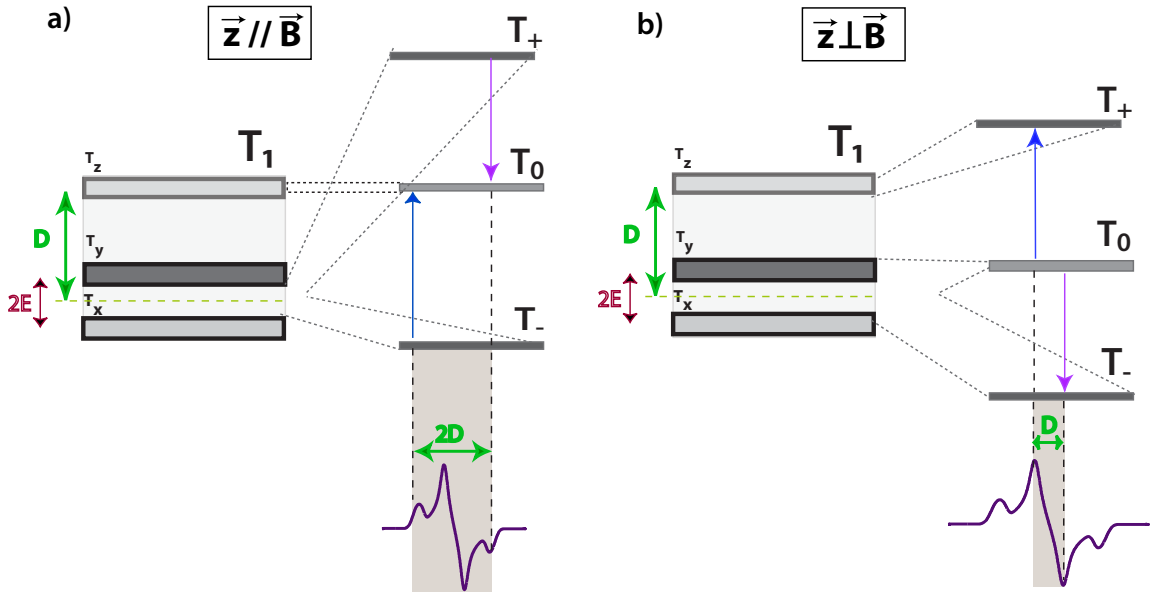


Figure 2.7: Schematic representation of the zero field and the in-field triplet state. a) The edges of the spectrum correspond to molecules with their z axis parallel to the magnetic field. Since the z axis is parallel to the field the T_z state becomes T_0 while the T_x and T_y mix to give the T_+ and T_-. The distance between the absorption (blue arrow) and emission (pink arrow) at the edges of the spectrum is twice the ZFS, D. b) At higher fields the inner maxima of the spectrum correspond to a z axis perpendicular to the field and a x or y parallel to the magnetic field. The absorption in this case originates from the T_0 to T_+ transition while the emission in low fields comes from the T_0 to T_- transition. The corresponding width defines the D tensor.

a positive D the z sublevel has the lowest energy while when D is negative, the z sublevel has the highest energy.

In Figure 2.7a we assume a triplet state oriented with the z axis of the D tensor parallel to the magnetic field. In this case the T_z state corresponds to the high field m_s=0, T_0 state while T_x, T_y mix to produce the $m_s = -1$, T_- and $m_s = +1$, T_+ levels. The whole width of the EPR spectrum is $2D$ and its intensity is proportional to the population difference between the triplet sublevels. As we move to the inner maxima the picture changes as these field positions correspond to a x or y axis of the D tensor parallel to the magnetic field (Fig. 2.7b).

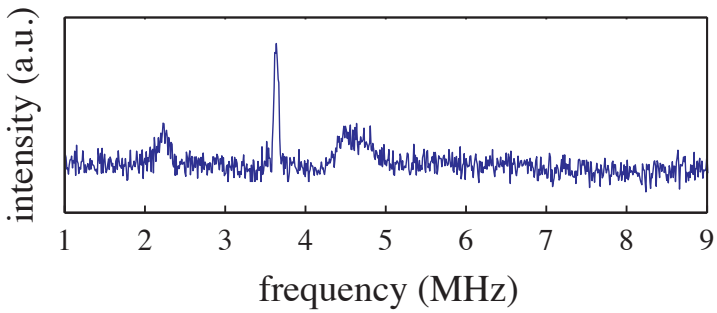


FIGURE 2.8: ENDOR spectrum of the diethyl fullerene malonate (DEFM). The main sharp peak is the Larmor frequency of the ^{13}C and the broad peak on the right the hyperfine interaction.

The third term of the Hamiltonian is the interaction of the magnetic moment of electron spins with nearby nuclear magnetic moments, through the hyperfine interaction (HFI):

$$H_{HFI} = S.A.I \tag{2.17}$$

A is the second rank hyperfine tensor. The hyperfine interaction consists of two terms: the isotropic Fermi contact term and the dipolar term (for their analytical expressions see Chapter 5). The isotropic hyperfine interaction is proportional to the spin density at the nucleus

$$\rho(\mathbf{r}) = |\psi(\mathbf{r}))|^2 . \tag{2.18}$$

In analogy to the Zeeman interaction, the nuclear Zeeman term describes the coupling of a nuclear spin I to the applied magnetic field

$$H_{NZ} = g_N \mu_N B_0 I_z. \tag{2.19}$$

For the determination of the hyperfine tensor, ENDOR methodology is employed. In photoexcited triplet states a typical ENDOR spectrum consists of sharp lines which correspond to the nuclear Larmor (Zeeman) frequency ω_L of the nuclear spins as well as additional peaks at different frequencies arising from the hyperfine couplings (Fig. refdemfendor). Usually these peaks are distributed normally around ω_L in radicals [KKL88] but

in photoexcited triplet states, they appear on certain sides of the Larmor frequency. The frequency difference between the Larmor peak and the side peaks provides information on the strength and sign of the hyperfine constants.

The interpretation of the hyperfine spectra can be quite difficult, even in single crystals, in cases were the principal axis of the hyperfine tensor does not coincide with the ZFS principal axis. In these cases, sets of Euler angles need to be incorporated in the analysis.

The last term we are going to discuss in this section, is the interaction between nuclear spins or the J-coupling

$$H_J = I_1 J I_2 \tag{2.20}$$

where J is the nuclear coupling tensor. The J-coupling often provides the smallest contribution to the Hamiltonian and is difficult to resolve through EPR. The presence of the electrons influences the local magnetic field between two nuclear spins, changing the orientation dependence of their interaction, thus there is often little relationship between the J-coupling and the inter-nuclear distances [Lev08].

A complete description of the principles of pulsed EPR and CW EPR can be found in references [SJ01, BG09].

2.8 EPR in triplet states

Several EPR studies have been performed in photoexcited triplet states of organic molecules for the characterization and the identification of structural properties for applications in chemistry and biophysics. In this Section we present general work based on the study of triplet states, we describe studies performed on the triplet state of the fullerene C_{60} and finally we will go through some techniques that show how triplet states might be beneficial for quantum computing.

2.8.1 Triplet studies for structural characterization and relaxation kinetics

Crystal structures are ideal for EPR studies due to their enhanced signal intensity (many spins contribute to signal at the same field) and their high orientational selectivity. A time-resolved CW ENDOR study of the triplet state of the freebase tetraphenyl-chlorin was made using partially oriented samples for the characterization of the molecular structure. The zero field splitting tensor and the hyperfine interaction were determined, while an observed lowering in symmetry was attributed to the state mixing of several triplet states which are close in energy to the lowest triplet state [KVM97]. Pulsed EPR experiments in pentacene hosted in two different crystals have been performed by Yago *et al.* [YLKL07]. Angular dependent ENDOR measurements using modified Davies-type pulse sequence and the various peaks in the ENDOR spectra were assigned to equivalent and non-equivalent protons in the structure.

In the work of Kay *et al* [KGTW01], CW EPR studies were performed on the free base porphycene in order to reveal whether is cis- or trans- configured (NH tautomerism), in the ground and triplet states by performing ENDOR experiments and DFT calculations. The study of the triplet state of photosynthetic systems attracts an interest as the underlying chemical reactions which are related to the energy conversion form a link between chemistry and biochemistry. An example is the study of the photoexcited triplet states in Plant Photosystem II, 3P680, and chlorophyll in a frozen organic solutions [VKGM96].

Apart from the determination of the terms of the spin Hamiltonian and the extraction of structural information, EPR expreriments are performed for the determination of properties like the triplet decay times, the population of the triplet sublevels and their fluorescent and phosphorescent nature.

CW time-resolved EPR studies (TR-EPR) have been performed for the determination of

the magnetic and decay properties of the lowest excited triplet state of pyridazine [TYH85a] and dichoropyridazine [TYH85b]. Both molecules undergo extremely fast non-radiative transitions from the first triplet to the ground state. This explains the lack of phosphorescence of the structures deviating from the strong phosphorescent character of their isomers pyrazine and pyridimine. The lack of phosphorescence initially was attributed to the inefficient intersystem crossing (ISC) [KP76, MS75]. An interesting observation was that the EPR spectra recorded at 0.4 μs and 2 μs after the laser excitation were identical but inverted, due to the fast triplet decay and the slow spin-lattice relaxation T_1. After the laser excitation, the T_y sublevel is mostly populated and the EPR signal has an absorption/emission profile. For a fast k_y decay rate ($k_y, k_x > k_y$, $p_y > p_z, p_x$) the T_y level empties out and the observed polarity becomes emissive/ absorptive. This polarity inversion was also observed in the work of Sloop *et al* in pentacene at higher temperature [SYalW84]. Another finding of the same study is that for temperatures up to 30 K, the decay rates remain constant which indicates that the spin-lattice relaxation doesn't affect the signals. In temperatures higher than 30 K, the rise of slow component of the time profile of the signal shows the impact of the spin-lattice relaxation.

2.8.2 EPR in the triplet state of fullerenes

Fullerenes, some of the most fascinating chemical structures, are widely known for their numerous photophysical and photochemical properties. The fullerene C_{60} has icosahedral symmetry (I_h) which suggests that in the ground state all atoms are equivalent. The high symmetry indicates that both the zero field splitting parameters, D and E should be zero. However, several EPR studies predict non-vanishing zero-field splitting (ZFS) parameters which reveal a lowering in symmetry upon excitation. This is attributed to the Jahn Teller effect which causes a slight distortion of the ground state structure in such way that

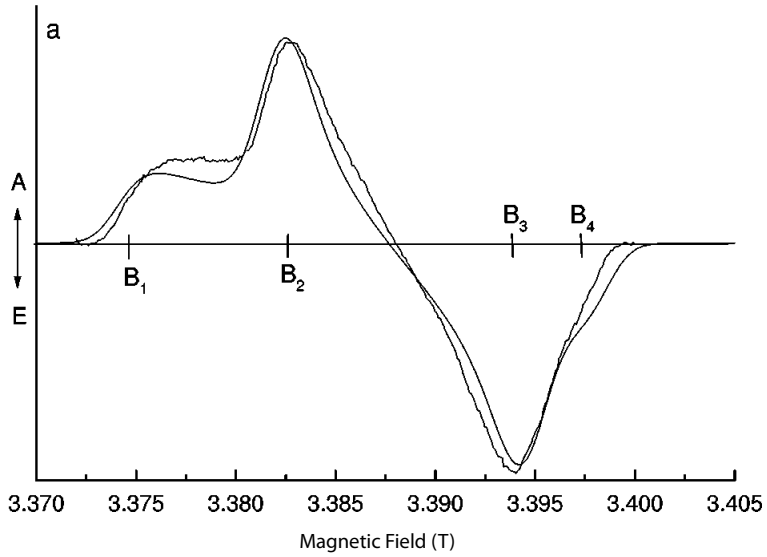


FIGURE 2.9: FS-ESE, W-band spectrum of the fullerene C_{60} at 1.5 K and the simulated spectrum. The spectrum is asymmetric in high and low fields. For the simulation the ZFS parameters proposed by Wasielewski [WOL$^+$91] were adopted.(original source : [DvdBvdH$^+$00]) Reprinted with permission from AIP : X. L. R. Dauw, G. J. B. van den Berg, and D. J. van den Heuvel, O. G. Poluektov, E. J. J. Groenen, The triplet wave function of C60 from W-band electron nuclear double resonance spectroscopy, Vol. 112 16 , Page 22, (April 2000) . Copyright [2000], American Institute of Physics.

the orbital character of the triplet excited state becomes non-degenerate [CO97]. The I_h symmetry of the ground state becomes D_{5d} or D_{3d} in the triplet state. Recent studies showed that the lowest triplet state, which has D_{5d} symmetry, is of an A_{2g} orbital character [SUN94].

An important characteristic of the triplet C_{60} is the significant narrowing of the EPR spectra observed at high temperatures (>100K). This phenomenon is attributed to a pseudorotation [THSS92, ACP96, RGM95], in other words, a shift of the triplet C_{60} ZFS axis which leads to five symmetry equivalent distortions.

The observation of the symmetry lowering of the C_{60} in the triplet state was made in EPR studies at X-band [WOL$^+$91], which showed that at low temperatures the ZFS

parameters are not zero but have the values $D = |340|$ MHz, $E = |15|$ MHz. Despite the fact that these parameters were confirmed by absorption detected magnetic resonance (ADMR) [AvSW$^+$94] studies, a number of simulations failed to reproduce successfully the experimental results using these values. For the simulation of the EPR spectra a number of attempts involving large linewidths, [THSS92, LMM$^+$92] as well as a combination of different D and E values [BGM$^+$92] arising from the presence of nearby triplet states and pseudorotation effects were adopted [RGM95, BGM95a]. What seems to reproduce better the asymmetric EPR spectra is the combination of different ZFS parameters resulting from the combination of different triplet species.

Experimental evidence of the presence of triplet states that lie close to the first excited triplet state come from studies at elevated temperatures up to 210 K [BGM$^+$92]. Initially, two triplet states were observed which correspond to the different mutual orientations that form the exciton. Later on, EPR experiments showed that there is an additional triplet state that differs due to the different orientation of the ZFS principal axis with respect to the crystal axis [MFG$^+$93].

Other studies were performed for characterization of the triplet exciton using W-band EPR [BHP$^+$98, GPM$^+$92] and photoluminescence [MFG$^+$93] experiments. These studies showed that upon photoexcitation below 80 K, the triplet exciton is delocalized over two, or over a chain of, C_{60} molecules, creating different spin densities and different hyperfine interactions. As far as the extension of the triplet excitation is concerned, previous studies have shown that the optical excitation of a pure single crystal which populates triplet states is delocalized [GPM$^+$92].

The sign of the fine structure parameters could not be confirmed by the EPR data and a detailed hyperfine investigation through ENDOR experiments was required. Pulsed Mims ENDOR experiments performed at 95 GHz [BHP$^+$98] revealed that the ENDOR spectra could be reproduced only by a negative D.

For a complete understanding of the dynamics of the fullerene C_{60}, flash-delay and inversion-recovery experiments were used to determine the lifetime and spin population of the triplet state. The negative zero field splitting obtained from ENDOR studies should result in a small population in the T_z sublevel compared to T_x, T_y which is in agreement with the studies of [RGM95, BGM95b] that predict $p_x : p_y : p_z = 1 : 1 : 0$. Terazima *et al.* [THSS92] report population of $p_x : p_y : p_z = 7 : 6.6 : 6$ (equivalent to $1 : 0.6 : 0$) with a triplet lifetime of 620 μs, very close to the 550 μs reported from W-band studies [Dau02]. The decay rates in these cases were $k_x = 1700s^{-1}$, $k_y = 1600s^{-1}$, $k_z = 1500s^{-1}$ and $k_x = 1500s^{-1}$, $k_y = 2300s^{-1}$ and $k_z = 1650s^{-1}$, respectively.

TR-EPR experiments were performed in the triplet states of C_{60} (and C_{70}) [THSS92] completing the work of Wasielewski *et al.* [WOL$^+$91] who reported similar EPR spectra using a light modulation technique. Both Terazima and Wasielewski agree that the strong EPR signal arises from the distortion of the molecular structures at least in the lowest excited triplet state. An interesting observation is that the polarity inversion that was observed in the case of pyridazine [TYH85a] and pyridimine is also present in C_{60} (and not present in C_{70}). The authors consider that this phenomenon is related to a thermally activated anisotropic spin lattice relaxation which is related to the T_x and T_y characters of the sublevels between which the relaxation takes place. The same explanation was given by Verbeek *et al.* in the case of triplet state of naphthalene in durene [VDS78, VdBS79].

The understanding of the characteristics of the fullerene C_{60} is the first step towards the study of more complicated, chemically modified fullerene structures. Functionalized fullerenes depending on the substitution group, exhibit greater solubility, smaller aggregation and are less affected by Jahn Teller distortions due to their lower symmetry [HE99, KBdR$^+$01].

2.8.3 Triplet states and quantum information

In quantum computing, high electron and nuclear polarization are essential requirements for efficient quantum operations. Upon laser excitation the ISC populates selectively the triplet levels and if the electron spin lattice relaxation of the triplet state is slower than the lifetime of the triplet state, high electron spin polarization is created and retained even at high temperatures. The electron spin polarization can then be used to polarize nuclear spin, through the DNP methods described above.

For example the Integrated Cross Polarization method [HLSW90] has been used for DNP with triplet states. It is particularly effective because electron spin packets participate in the polarization transfer due to adiabatic sweeping of the magnetic field under microwave irradiation. The polarization of the protons is localized initially around the photoexcitable molecules and then is spread via spin diffusion to the host material. The success of this method was demonstrated in pentacene dopped nafthalene at room temperature, through a 5000 times polarization enchancement, much higher than the limit of 660 achieved by using paramagnetic impurities. Later on Iinuma [IST$^+$95] achieved a 80,000 times larger polarization compared to the thermal ^{1}H polarization, on the same crystal at lower temperatures. This enhancement was further increased reaching 2×10^5 at one third of the experimental time. This significant enhancement was achieved by using more concentrated samples and optimized laser conditions [TTT04]. With such significant nuclear polarization enhancements, nuclear spin quantum computing schemes can be realized under the presence of highly initialized triplet states.

A different type of study was performed by Kothe *et al.* [KYW$^+$10, YWL$^+$07] who observed nuclear quantum oscillations in the transverse electron spin mangetization of pentacene crystals in the photoexcited EPR triplet state. Their analysis reveals that laser excitation generates oscillatory nuclear spin polarization. For the detection of the nuclear

spin polarization, in-situ NMR experiments were performed (the ENDOR resonator was tuned to the proton frequency and connected to an NMR spectrometer). The oscillatory nuclear spin polarization produces large NMR signal enhancement factors determined from the FID amplitude under laser excitation and in the dark. The 1100-fold enhancement and the formation of quantum oscillations are attributed to the light excitation and an additional mixing of the zero field triplet states with the hyperfine interaction.

3

Density Functional Theory

Density Functional Theory (DFT) is widely used for the simulation of the electronic structure of materials and molecules. Its scope is very large and covers mainly the prediction of properties of the ground state of any electron system. In this chapter we are going to present the basic principles of the density functional theory and describe the plane wave pseudopotential methodology. The plane wave pseudopotential methodology which has made a great progress the past years, allows for the prediction of properties of materials based on first-principles. The results are accurate and permit a direct comparison with

experimental measurements. First-principles calculations have recently met with a number of successes in the calculation of the magnetic properties of materials, in particular when it comes to the building blocks of the spin Hamiltonian such as chemical shifts, [ZPA09, DMM07, SYT07, MPL96, TPB07, RMPF05] J-couplings, [JYPB08] and g-tensors [GRMS09, GSC+10, PM02].

3.1 Density Functional Theory

The use of the many body wavefunction $\Psi(\mathbf{r_1}, \mathbf{s_1} ... \mathbf{r_N}, \mathbf{s_N})$ for obtaining information about atomic and molecular systems, in the Hartree [Har28a, Har28b] and Hartree-Fock [Low78] approximations, made these methods computationally very expensive even in small molecules.

P. Hohenberg and W. Kohn formulated the foundations of the modern density functional theory in 1964 through the presentation of two theorems [HK64]. In the first theorem it was stated that the ground state electronic density distribution $\rho_0(\mathbf{r})$ contains the same information as the ground state wavefunction Ψ_0 and can be used alternatively for the complete description of the ground state of the system. The second theorem shows that for a given number of electrons in an external potential, the ground state energy of the system is the global minimum value of the energy functional $E^{HK}[\rho]$, and the density ρ which minimises the functional, is the exact ground state density ρ_0

$$E^{HK}[\rho] \geq E^{HK}[\rho_0] = E_0 \tag{3.1}$$

Given the above theorems, we now have a way to calculate the energy of a system $E^{HK}[\rho]$ in an external potential using the electronic density

$$E^{HK}[\rho] = F[\rho] + V_{ext} \tag{3.2}$$

V_{ext} is the external potential energy and F the internal electronic energy functional of the system. In the above equation the internal electronic energy is yet unknown but its evaluation would lead us to a good approximation to the determination of the ground state energy and density.

In principle, the term 'density-functional theory' refers to all theories that are based on the approximation of the HK density functional $E^{HK}[\rho]$.

3.2 Kohn-Sham method

The Kohn Sham [KS65] method provides a way of approximating the unknown functional $F[\rho]$. Within this framework the complicated many body problem of interacting electrons in a static external potential, can be simplified by assuming that non interacting electrons move in a fictitious external potential, in a way that the true ground-state density distribution ρ_0 is identical to the ground state ρ of this non interacting fictitious system. The total electronic ground state energy of this system is given by the following expression

$$E[\rho] = -\frac{1}{2}\sum_i \langle\psi_i|\nabla^2|\psi_i|\rangle - \sum_I \frac{Z_I\rho(\mathbf{r})}{|\mathbf{r}-\mathbf{R_I}|} + \int d\mathbf{r}d\mathbf{r}'\frac{\rho(\mathbf{r})\rho(\mathbf{r}')}{|\mathbf{r}-\mathbf{r}'|} + E_{xc}[\rho] \tag{3.3}$$

where

$$\rho(\mathbf{r}) = \sum_i \psi_i^*(\mathbf{r})\psi_i(\mathbf{r}) \tag{3.4}$$

The index I represents the atomic nuclei of the system that carry Z_I charge, placed in sites R_I, while i represents the occupied electronic states. The expression of the total energy $E[\rho]$ contains the kinetic energy of the non interacting electrons, the potential energy of the interaction between electrons and nuclei and the Hartree repulsion between the electron i and the charge density distribution of every other electron. The last term E_{xc}, is an unknown functional of the density and represents the exchange and correlation energy. The

kinetic energy, the Hartree repulsion and the E_{xc} construct the functional $F[\rho]$. Most of the terms in the above expression can be estimated from a single particle picture. The E_{xc} contains contributions from the Hartree-Fock (HF)-like exchange of electrons of same spin, and the correlation of the individual electrons, due to Pauli repulsion. Upon minimisation of the above expression we obtain a Schrödinger-like equation for the ψ_i

$$[-\frac{1}{2}\nabla^2 - \sum_I \frac{Z_I}{|\mathbf{r_i} - \mathbf{R_I}|} + \int d\mathbf{r}' \frac{\rho(\mathbf{r}')}{|\mathbf{r} - \mathbf{r}'|} + V_{xc}[\rho]]\psi_i = \epsilon_i \psi_i \tag{3.5}$$

The only term that remains to be determined now is the unknown exchange correlation potential $V_{xc}(\mathbf{r}) = \frac{\partial E_{xc}}{\partial \rho(\mathbf{r})}$ or the equivalent functional E_{xc}.

3.3 Defining $\mathbf{E}_{\mathrm{xc}}$

Although Kohn Sham formalism provides a practical tool for the solution of the many-body problem it is still not of any practical use since the exchange correlation term contains the many-body wavefunctions. Several methods are proposed for the definition of the exchange correlation functional. The most common approximation of the E_{xc} is the local density approximation (LDA) [KS65].

Central idea to the LDA method is that that the exchange correlation energy of a non uniform system at any point in space coincides with the exchange correlation energy ϵ_{xc} of a homogeneous electron gas that has the same density ρ at this point of space.

$$E_{xc}^{LDA}[\rho] = \int \rho(r)\varepsilon_{xc}[\rho(r)]d^3r \tag{3.6}$$

The exchange correlation energy has been calculated [CA80] and parametrized through Monte Carlo simulations for a uniform electron gas for a variety of electron densities and for that it is expected to be accurate for systems with slow varying electron density [[CA80]].

An extension of the LDA can be obtained by including local density gradient corrections to the exchange corelation energy. The so called GGA approximation [Per86], which in a number of cases improves the results obtained with LDA, converts the E_{xc} functional to a semi-local functional of the density

$$E_{xc}^{GGA}[\rho] = \int \rho(r), \varepsilon_{xc}(\rho(r), \nabla\rho(r))dr^3 \tag{3.7}$$

A great number of GGA functionals exist but the most widely used are those of Perdew, Burke, and Ernzerhof (PBE) [PBE96] and Perdew and Wang [PW86] . The PBE functional is quite reliable and will be used in the work presented in chapter 5.

Other types of functionals, called hybrid functionals like the B3LYP [LYP88] give results in good agreement with the experiment. The term hybrid is used because these functionals incorporate a mixture of Hartree Fock and DFT exchange and bring together the non-interacting and fully interacting states. One of the main differences between the hybrid and the other types of functionals is that they include a portion of the exact exchange corelation term.

3.3.1 Supercells

In cases like solids are studied where there is an infinite number of non interacting electrons, the huge computational cost forces us to consider an approach based on the generation of supercells. A unit cell which is a box in which we place the a portion of structure we study and is repeated periodically in space, is described by three vectors $\mathbf{a_1}$, $\mathbf{a_2}$ and $\mathbf{a_3}$. The volume of the cell is $\Omega = \mathbf{a_1} \cdot (\mathbf{a_2} \times \mathbf{a_3})$ and the general lattice vector R is defined as $R = n_1\mathbf{a_1} + n_2\mathbf{a_2} + n_3\mathbf{a_3}$, where n is any integer number. The translational symmetry of the atomic configurations can be used to reduce the computational cost and lead us to the solution of the KS equations. For the purposes of this work despite the fact that we don't

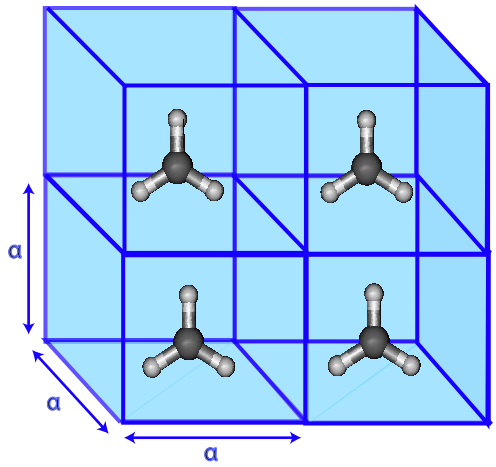


FIGURE 3.1: Schematic illustration of supercell that contains an array of unit cells repeated periodically in space. The structure under investigation, an isolated molecule in this case, is placed into the unit cell of dimension a.

study systems with periodic boundary conditions we still make use of supercells in which we place the whole molecular structure. We define the cell dimensions in such way that our structure doesn't interact with the structures in neighbouring cells.

3.4 Basis functions

Having determined the exchange correlation energy, E_{xc} and by making use of the periodic boundary conditions we can move towards to the solution the Kohn Sham equation 3.5. In order to achieve that, we first need to find a representation, an expansion of wavefunction in a convenient basis, a basis set. The basis sets are divided into two popular categories, the plane waves and the localized atomic orbitals.

Plane waves

In a periodic system the total wavefunction can be constructed by a periodic part $u_k(\mathbf{r})$ and a plane wave contribution $e^{-2\pi i \mathbf{k}\cdot\mathbf{r}}$

$$\psi_{\mathbf{k}}(\mathbf{r}) = u_{\mathbf{k}}(\mathbf{r})e^{-2\pi i\mathbf{k}\cdot\mathbf{r}} \tag{3.8}$$

By applying Fourier transformation to $u_k(\mathbf{r})$ we obtain the following representation

$$u_{\mathbf{k}}(\mathbf{r}) = \frac{1}{\sqrt{\Omega}}\sum_{\mathbf{G}} c_{\mathbf{k}}(\mathbf{G})e^{-2\pi i\mathbf{G}\cdot\mathbf{r}} \tag{3.9}$$

where G is a reciprocal lattice vector and Ω the volume of the cell. The KS wave functions can be expanded in a discrete set of plane waves using the following expression

$$\psi_{\mathbf{k}}(\mathbf{r}) = \sum_{\mathbf{G}} c_{\mathbf{k}+\mathbf{G}}\frac{1}{\sqrt{\Omega}}e^{-2\pi i(\mathbf{k}+\mathbf{G})\cdot\mathbf{r}} \tag{3.10}$$

where $c_{\mathbf{k}+\mathbf{G}}$ are complex coefficients and the functions $e^{i(\mathbf{k}+\mathbf{G})\cdot\mathbf{r}}$ representt the plane waves basis functions.

In principle an infinite basis set should be used to expand the KS wavefunction but it is possible to constrain the size by including only a number of plane waves with kinetic energies less than a defined cutoff energy E_{cut}(a.u)

$$\frac{1}{2}|\mathbf{k}+\mathbf{G}|^2 \leqslant E_{cut} \tag{3.11}$$

The advantage of plane waves basis sets has to do with their simplicity, their extended (they cover all space equally) and their ability to systematically converge with respect to one parameter, the cutoff energy E_{cut}. However, a large number of plane waves is needed in order to achieve convergence. Plane wave methodology is extremely succesful in the calculation of systems with periodic boundary conditions but in finite systems, large cells need to be incorporated into the calculations in order to avoid interactions between structures in neighbouring cells.

For calculations in periodic systems a specific k-point mesh is required for the description of the first Brillouin zone. This k-point mesh is a continuous set of points which maps the

region of the reciprocal space. In molecular structures the first Brillouin zone is sampled only at one k-point (Γ calculation).

Localized basis

Another type of basis is the localised orbital basis. In this approach, the molecular orbitals of the system are synthesised by a Linear Combination of Atomic Orbitals (LCAO), which in turn, are expressed as suitable linear combinations of either Gaussian-type functions (GTO) or Slater-type functions (STO) [Boy50, Jen07]. STOs and GTOs form a complete basis set and are commonly used in electronic structure calculations. Slater type orbitals have the form

$$\chi_{\zeta,n,l,m}(r,\theta,\phi) = NY_{l,m}(\theta,\phi)r^{n-1}e^{-\zeta r} \tag{3.12}$$

where N is a normalization constant, Y are the spherical harmonics, ζ a factor which depends on the width of the orbital and n is the principal quantum number. The two important points about STOs is that the exponential dependence of the distance between the nucleus and the electron coincides with the hydrogen orbitals and second, the accurate representation of the radial nodes of the wavefunction through the use of a linear combination of STOs. The difference between an STO and a GTO is in the description of the radial decay which converts the atomic orbitals to Gaussian functions

$$\chi_{\zeta,n,l,m}(r,\theta,\phi) = NY_{l,m}(\theta,\phi)r^{2n-2-l}e^{-\zeta r^2} \tag{3.13}$$

The calculation of the hyperfine interaction using STOs seems to outperform GTOs for two reasons [**?**]cramer) At the point of the nucleus GTOs are smooth due to their gaussian nature, differentiable and they don't reproduce the behaviour of a hydrogenic atomic orbital which has a cusp at $r = 0$. The other characteristic is related to the fast decay of GTOs compared to STOs which fails to represent accurately the wavefunction far from the nucleus.

The computational efficiency achieved through the use of GTOs though, and the interesting observation that one STO can be represented by a linear combination of GTOs (roughly 3 GTOs are required to reproduce accurately one STO) reveal a way of merging the best characteristics of both basis functions and develop codes which combine both types of orbitals.

3.4.1 Self consistency

In density functional theory in order to minimize the total energy, the Kohn Sham equations need to be solved iteratively until self consistency is reached. The self-consistent calculation starts with an initial guess of the electron density which is used to construct the effective potential. For the representation of the wavefunctions a finite set of plane waves is used obeying the cutoff energy restriction of Eq. 3.11. The KS equations are solved at each k-point and the new KS wavefunctions are used to construct a new electron density. Convergence is reached until a specified criterion which compares the energy or (and) the electron density of one iteration with the one of the previous cycle, is reached.

3.5 Pseudopotentials

Most of the chemical properties of the systems depend to a significant extend to the distribution of the valence electrons. The core electrons are localized around the nucleus and the distribution of the wavefunction does not change with the chemical environment as it doesn't overlap with the wavefunctions of nearby atoms.

The core electrons are responsible for the presence of nodes in the valence and core wavefunctions. For example in figure 3.4.1 the 3s wavefunction of Si oscillates while the 1s wavefunction appears to be smoother. In general the expansion of the localized wavefunctions in plane waves would be of a quite high computational cost since a high energy

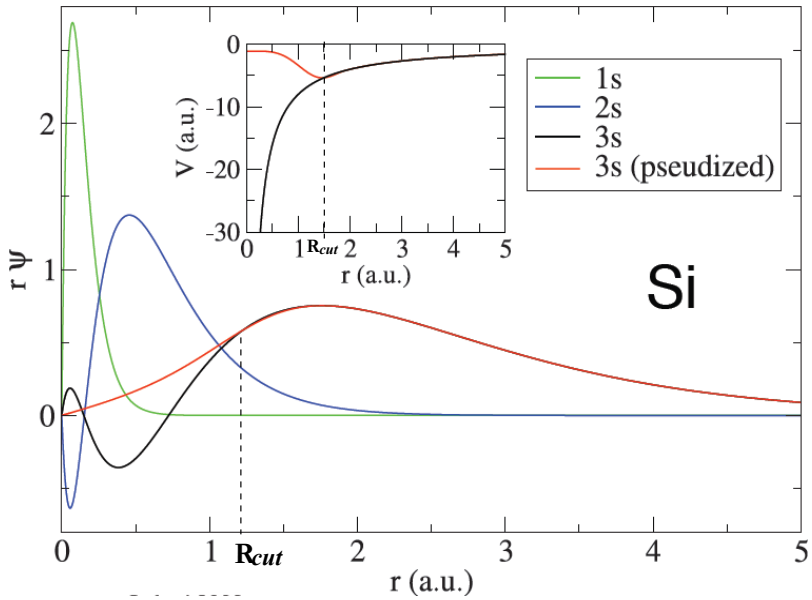


FIGURE 3.2: Graphical representation of the 1s, 2s, 3s AE wavefunctions of the Si atom. The 3s pseudo wavefunction is shown in red. The AE and PS 3s wavefunctions coincide outside the region R_{cut}. The nodless character of the 3s PS wavefunction indicates that less plane wave are required for its representation. (inset) AE potential (black) and pseudopotential (red) of the 3s atomic state of Si atom. The pseudopotentials also coincide outside the cutoff region (original source : Presentation slides: 'GIPAW : A solid state theory for NMR, Jonathan Yates, 2011').

cutoff E_{cut}, and hence a very large set of plane waves could represent accurately the strong oscillations near the nucleus.

The goal in the pseudopotential (PS) approach [Phi58, PK59, CH70] is to replace the Coulomb potential with an effective, pseudopotential, which incorporates the potential of the nucleus, the screening and the repulsion by the core electrons. The core electrons are pre-calculated in an atomic environment and kept frozen in the course of the remaining calculations (*frozen core approximation*) so the KS equations don't need to be solved for the core electrons. In the pseudopotential approximation only the valence electrons outside the core region are considered and the pseudo wavefunction can be represented by a nodeless function inside the core regions which coincide with the true all electron wavefunction

outside a cutoff radius R_c. (Fig. 3.4.1). The advantange of this method is that allows the use of fewer plane waves for the description of the wavefunction reducing this way the computational cost.

3.5.1 Types of pseudopotentials

A type of pseudopotentials introduced by D. R. Hammann et al. are the norm conserving pseudopotentials [HSC79] in which the wave function and its radial derivative are continuous at R_c, the charge is conserved in the core region and the normalised AE and PS orbitals are equal outside the core region. The most popular type of norm conserving pseudopotentials are the Troullier and Martins [TM91] which generalize ideas from G. P. Kerker [Ker80] to propose a smooth analytical form for the projector functions. In 1990 Vanderbilt [Van90] introduced the ultrasoft pseudopotentials (US-PP) which relax the norm conservation condition. Ultrasoft pseudopotentialsfewer plane waves but are of the same accuracy. In US-PP the cutoff radius is chosen according to the covalent radius and becomes progressively softer as we move to atoms in higher periods. In general for accurate and transferable pseudopotentials the choice of small cut off radius leads to hard pseudopotentials and consequently a large basis set is required for the representation of the wavefunction. Smoothness, generally leads to larger cut-off radius, fewer basis functions are required and rapid convergence is achieved. All the above underline the challenge that is introduced in atomistic calculations and concerns the balance between accuracy and computational efficiency.

3.6 Projector Augmented Wave (PAW) method

In 1994 Bloch developed a method called Projector Augmented Wave (PAW) method [Blö94]. The key point of this method is that it combines the plane wave pseudopotential approach with the linear augmented projected wave (LAPW) method [SB92]. The PAW

method is considered as the most general augmentation scheme which makes the LAPW a special case of the PAW incorporating at the same time the pseudopotential approach by a well defined approximation.

The smooth behaviour of the wavefunctions in the bonding region compared to the rapidly oscillating wavefunction close to the nucleus poses a challenge to the electronic structure methods. Augmented wave methods divide the wavefunction into two parts. A partial wave expansion in a sphere that includes the atom, named the core region and envelope functions outside the sphere expanded into plane waves basis sets. Right at the sphere radius two boundary conditions need to be satisfied where the partial waves and envelope function are matched with value and derivate.

Upon the application of a transformation $\boldsymbol{T}$ the AE wavefunction is mapped to a computationally convenient pseudowavefunction that is smooth and has rapidly convergent plane wave expansion $|\Psi_f\rangle = \boldsymbol{T}|\tilde{\Psi}_f\rangle$. Using this formula we are able to obtain physical quantities and calculate the expectation value of an operator W from pseudowavefunctions

$$\langle W\rangle = \langle\tilde{\Psi}_f|\tilde{W}|\tilde{\Psi}_f\rangle \tag{3.14}$$

where $\tilde{W}$ the pseudo operator

$$\tilde{W} = \mathbf{T}^{+}W\mathbf{T} \tag{3.15}$$

The next step is to define the transformation $\boldsymbol{T}$ in a way that the smooth pseudowavefunction in each region can represent accurately the correct nodal structure of the wavefunction. The transformation $\boldsymbol{T}$ takes the form

$$\mathbf{T} = 1 + \sum_{R}\hat{T}_R \tag{3.16}$$

is expressed as a sum of atomic contributions of R atomic sites which act within some augmentation region enclosing the atom Ω_R. This criterion ensures that AE and PS wavefunctions coincide outside the augmentation region. For each augmentation region the term

$\hat{T}_R$ is defined and satisfies the following relation

$$|\phi_i\rangle = \tilde{T}_R|\tilde{\phi}_i\rangle \tag{3.17}$$

where $|\phi_i\rangle$ a set of partial waves, solutions of the radial Schrödinger wavefunction for the isolated atom multiplied by the spherical harmonics. For each AE partial wave there is a corresponding pseudo partial wave $|\tilde{\phi}_i\rangle$ which is identical to the AE partial waves outside the augmentation region.

Within the augmentation region the pseudo wavefunction takes the form

$$|\tilde{\Psi}\rangle = \sum_i |\tilde{\phi}_i\rangle c_i \tag{3.18}$$

and c_i describe a set of the expansion coefficients.

The all electron AE wavefunction then becomes

$$|\Psi\rangle = \boldsymbol{T}|\tilde{\Psi}\rangle = \sum_i |\phi_i\rangle c_i \tag{3.19}$$

Combining the above equations the AE wavefunctions can be described in a form which includes the pseudo wavefunction and the partial waves

$$|\Psi\rangle = |\tilde{\Psi}\rangle - \sum_i |\tilde{\phi}_i\rangle c_i + \sum_i |\phi_i\rangle c_i \tag{3.20}$$

The expansion coefficients c_i have the form of linear functionals and are products of the PS wavefunction with projector functions $\langle\tilde{p}_i|$

$$c_i = \langle\tilde{p}_i|\tilde{\Psi}\rangle \tag{3.21}$$

These functions are localized in the core region and break the gauge invariance (this will be discussed in the next section). The projector functions probe the local character of the pseudowavefunctions and satisfy the following condition , for $r > R_c$

$$\sum_i |\tilde{\phi}_i\rangle\langle\tilde{p}_i| = 1 \tag{3.22}$$

so that the the expansion of the pseudo wavefunction using projected functions and partial waves to be identical to the pseudo wavefunction

$$|\Psi\rangle = \sum_i |\tilde{\phi}_i\rangle\langle\tilde{p}_i|\tilde{\Psi}\rangle \tag{3.23}$$

and satisfy the relation

$$\langle\tilde{p}_i|\tilde{\phi}_i\rangle = \delta_{ij} \tag{3.24}$$

Finally by incorporating the above relations to the transformation $\boldsymbol{T}$ we can write

$$\mathbf{T} = 1 + \sum_i (|\phi_i\rangle - |\tilde{\phi}_i\rangle)\langle\tilde{p}_i| \tag{3.25}$$

The final expression of the AE wavefunction is presented as a function of the partial waves and the projected functions for every partial wave localised in the augmentation region

$$|\Psi\rangle = |\tilde{\Psi}\rangle + \sum_i (|\phi_i\rangle - |\tilde{\phi}_i\rangle)\langle\tilde{p}_i|\tilde{\Psi}\rangle \tag{3.26}$$

In this expression the pseudo partial waves $|\tilde{\phi}_i\rangle$ coincide with the all electron partial waves outside the defined augmentation region.

3.7 Calculation of Hyperfine Parameters

While all electron methods based on localised basis sets are quite reliable for the calculation of the hyperfine parameters there isn't a definite approach towards the calculation of the hyperfine parameters by pseudopotential methods. The reason for this, lies in the nature of the (isotropic) hyperfine interaction which requires the knowledge of the spin density at and in the vicinity of the nucleus. The calculation of the isotropic hyperfine interaction

using pseudopotential methods turns to be quite challenging for two reasons. The first one is related to the behaviour of the wavefunction within the core region which differs from the all electron one and the second concerns the complete elimination of the core electrons and consequently the neglect of core polarisation effects.

Bloch and Walle [WB93] were the first to provide a sufficient solution to the problem by addressing the first challenge by introducing PAW. Their method is considered quite reliable and it has been successfully applied to systems with s-like singly occupied molecular orbitals (SOMO). The second challenge, the inclusion of core spin polarisation effects seems to be approaching the goal for the extraction of an accurate isotropic hyperfine interaction somewhat faster. O. V. Yazyev et al. [YTHR05] proposed a method which uses a reconstruction of the all-electron wave functions and the frozen valence spin-density approximation to solve the Kohn-Sham equations for core electrons only. This method predicts the correct isotropic hyperfine interaction for a series of small radicals but its application to more complicated systems has yet to be determined.

3.8 GIPAW

Recently C. J. Pickard and F. Mauri developed an extension of the PAW method called Gauge Including Projector Augmented Waves (GIPAW) [PM01] for the calculation of NMR chemical shifts. In their work they address the change in the local electronic environment of magnetic nuclei placed in an external applied magnetic field. The difference of this method comparing to Blöchl's method is that in this case the gauge invariance is restored.

Gauge invariance

The magnetic parameters may depend on the choice of vector and scalar potentials. The origin of these potentials is located on the nucleus which is independent of the molecular structure. In the presence of a magnetic field the PAW method is not invariant under gauge

origin transformations but GIPAW restores the translational invariance by introducing a field dependent transformation operator. For the derivation of the GIPAW transformation the starting point is the PAW transformation $\mathbf{T}$,(Eq 3.25), which becomes invariant by the inclusion of a phase factor that compensates the gauge term

$$\mathbf{T_G} = 1 + \sum_R e^{(i/2c)\mathbf{rR}\times\mathbf{B}}(|\phi_\mathbf{R}\rangle - |\tilde{\phi}_\mathbf{R}\rangle)\langle\tilde{p}_R|e^{(i/2c)\mathbf{rR}\times\mathbf{B}} \tag{3.27}$$

$\mathbf{R}$ runs over all atoms in the system, $\mathbf{r}$ is the position operator and $\mathbf{B}$ the magnetic field. The development of this method became essential as there hasn't been a full theory for the calculation of the NMR chemical shifts in extended periodic systems. As an improvement to the conventional theories Mauri, Pfommer and Louie presented a theory for the calculation of the NMR chemical shifts in condensed matter system with periodic boundary conditions using norm conserving pseudopotentials [MPL96]. This method was restricted to the calculation of NMR shifts of light elements (hydrogen, carbon, nitrogen and silicon) due to certain complications inherent within the pseudopotential approximation. Some years later studies of Gregor et al. [GMC99] showed that the core and valence contributions are not individually gauge invariant as expected and the core contributions are rigid and a pseudopotential approach can exist. Taking this into consideration, the work of Blöchl mentioned before, which provides a useful framework for the unification of the pseudopotential approach with the linearised plane waves, gave the opportunity to Pickard and Mauri to develop their theory in finite and extended systems.

Apart from the calculation of NMR parameters GIPAW is also extended to the calculation of EPR parameters. There is an ongoing effort to apply GIPAW to the calculation the g-tensor and D tensor and the hyperfine parameters. So far GIPAW has been successfully used for the calculation of the g-tensor for defects in solids [PM02] but its application to the calculation of hyperfine parameters requires some thought.

In chapter 5 for the calculation of the hyperfine tensor, we are going to employ the method proposed by Barhamy [BSK07]. In this method the PAW methodology is applied for the reconstruction of the frozen-core all-electron wave functions in the core regions while the contributions of the core orbitals to the charge density at the nucleus are evaluated through first-order perturbation theory. In our calculations this method is incorporated in the GIPAW module and is performed as a post processing step of a self consistent PAW calculation. More details about this method can be found in Chapter 5.

4

Feasibility of scheme to entangle nuclear spins

4.1 Introduction

In this chapter I will present briefly a theoretical proposal for entangling two nuclear spins in the presence of a photo-excited mediator and describe in detail pulsed EPR experiments and ab-initio calculations, that would allow us to put into practice the theoretical proposal. The experiments have been performed on the diethyl fullerene malonate (DEFM), a test molecule with one nuclear spin. Our studies identify the conditions that have to be met in order to create high power entangling gates under optical, microwave and radiofrequency

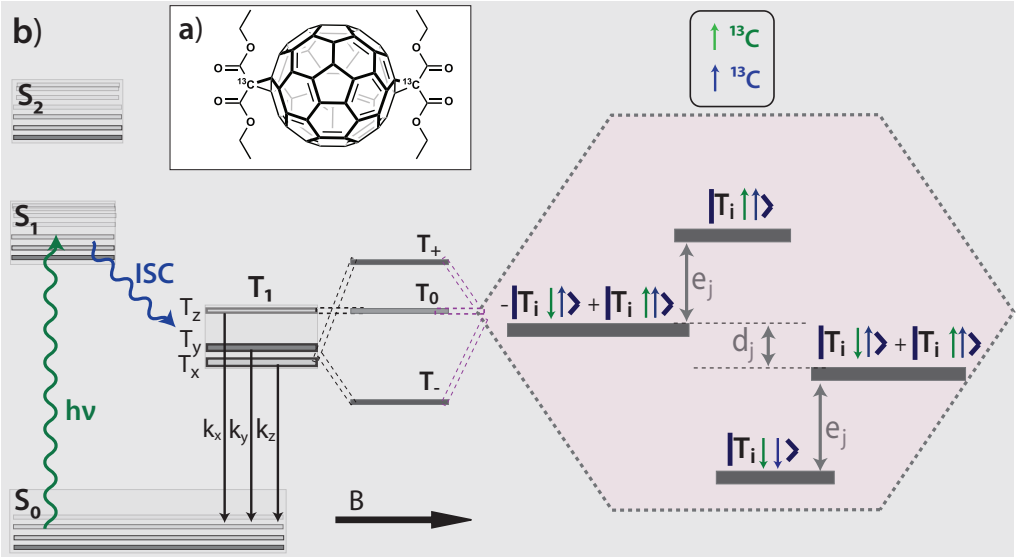


FIGURE 4.1: a) Trans-1 DEFM, a molecule with two ^{13}C nuclear spins. b) Representation of the energy level diagram. Upon photoexcitation to the first singlet state ISC populates preferentially the triplet subleves T_x, T_y, T_z. The application of a mangnetic field creates the T_+, T_0 and T_- levels which are orientation dependent linear combinations of the zero field sublevels T_x, T_y, T_z. The in-field triplet levels are coupled to the two nuclear spins ^{13}C. In the figure, T_i is the in-field triplet state with i=+,0,− and with blue and green arrows we denote the two nuclear spins. For the determination of e_j and d_j we use the expressions of Ref. [SLG11b] : $e_- = \omega_n - A + 2\alpha_-$, $e_0 = \omega_n + 2\alpha_+$ and $e_+ = \omega_n + A$ and $d_- = -2\alpha_1$ d_0 = - 2α and $d_+ = 2\alpha$ for each nuclear subspace. a_+, a_- and a_0 are determined by eqs (4.2),(4.3).

pulses.

4.2 Theoretical Proposal

The theoretical scheme was proposed by Schaffry et al. [SFK$^+$10] and suggests a method for switchable optical control of two nuclear spins, fast quantum gates compared to NMR analogues and large energy transitions which allow for efficient polarisation transfer to the nuclear spins.

We consider a system with two nuclear spin qubits which interact through a photo-excited mediator and not directly, via the isotropic hyperfine interaction (HFI). The mediator which is diamagnetic ($S_z = 0$) in the ground state, becomes paramagnetic ($S_z = 1$) upon photoexcitation. Depending on the system under consideration, the two nuclear spins can be coupled with equal (symmetric case) or unequal hyperfine strengths (asymmetric case) to the mediator.

For this proposal, we consider the symmetric case, where two nuclear spins are coupled with the same HFI strength to the triplet state. Figure 4.1 shows an example of a molecule with two ^{13}C nuclear spins the $trans-1$ DEFM as well as the level diagram for this system. Upon excitation the system relaxes from the first excited singlet state, to the lowest triplet state through ISC. Upon the application of the magnetic field the levels mix in an orientational dependent manner. Each of the triplet levels, T_+, T_0 and T_- is coupled to the nuclear subspace of two ^{13}C nuclear spins via the hyperfine interaction.

In this work the strength of the HFI is directly correlated to the degree of entanglement between the two nuclear spin qubits. In order to quantify the entanglement we use the term 'entanglement of formation' [1].

The time evolution of the entire system can be decomposed into three different unitary actions on the nuclear spin, one for each spin projection of the electron spin $|T_i\rangle$, $(i = -, 0, +)$.

$$U(t) \approx U_-(t) \bigoplus U_0(t) \bigoplus U_+(t) \tag{4.1}$$

The triplet state T_i and the nuclear spins, $|T_i \downarrow\uparrow\rangle$ and $|T_i \uparrow\downarrow\rangle$ are coupled with a matrix element

[1] According to the Ref. [Woo98], the entanglement of formation of a mixed state is the minimum average entanglement of an ensemble of pure states that represents the mixed state.

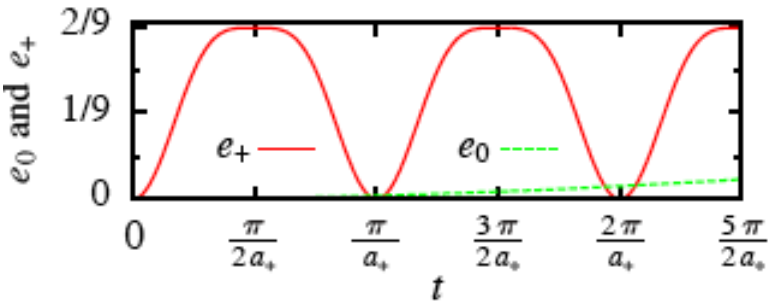


FIGURE 4.2: Entangling power of the time evolution operators U_+ (solid curve) and U_0 (dashed curve). The first maximum occurs for $t = \frac{\pi}{2\alpha_+}$. The periodic nature of the entangling power allows the application of the protocol twice or more in succession.

$$a_\pm = \frac{2A^2}{\mp D + 2\omega_e + 4\omega_n} \tag{4.2}$$

$$a_0 = a_+ - a_- \approx \frac{DA^2}{\omega_e^2} \tag{4.3}$$

where ω_e is the electronic Zeeman splitting, ω_n the nuclear Zeeman splitting, D the ZFS and A the hyperfine interaction. The coupling a_i, which depends on the triplet state and the hyperfine interaction, takes an initial product state, to an entangled state of nuclear spins. The entangling power of a unitary transformation U_i is denoted by e_i and is given from the relation $e_i(t) = \frac{1}{9}\left(3 + cos(2a_i t)\right) sin^2(a_i t)$. The power of a maximally entangling gate is 2/9 [ZZF00].

According to Figure 4.2, the unitary transformation $U(t)$ which represents the time evolution of the system is maximally entangling at odd integers multiples of $\frac{\pi}{2a_i}$. Assuming that the state of the excitation is in the $|\mathrm{T}_0\rangle$ state, no entanglement is created, as indicated by the green trace. Upon the application of a microwave pulse, we flip the state of excitation to the $|\mathrm{T}_+\rangle$ state and wait for time $\frac{\pi}{2a_+}$ until the nuclear spins are entangled (Figure 4.2, red trace). The application of a second microwave pulse flips the excitation back to the

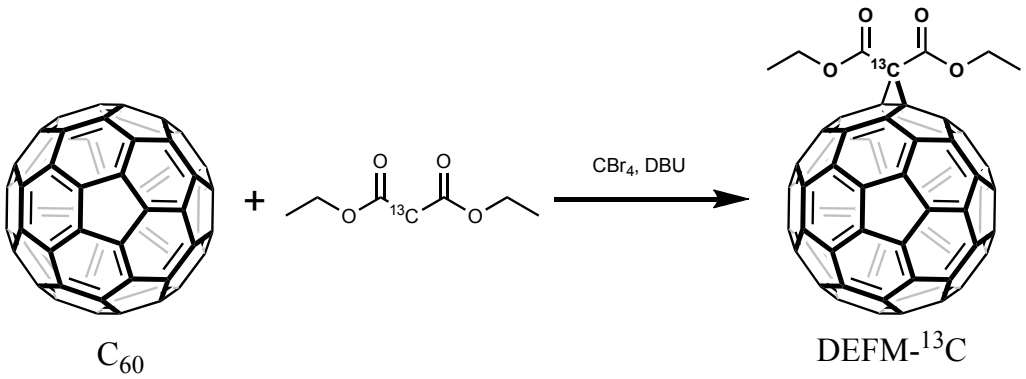


Figure 4.3: Diethyl fullerene malonate (DEFM) with a spin labeled ^{13}C nuclear spin on the diethyl malonate adduct. The system is spin silent in the ground state and spin active in the triplet state. The electron spin is delocalized over the fullerene cage.

$|\mathrm{T}_0\rangle$. For an excitation lifetime of

$$\frac{\pi}{2\alpha_{\pm}} < \tau \ll \frac{\pi}{2\alpha_0} \tag{4.4}$$

the nuclear spins remain entangled for the duration of the nuclear coherence. After the flipping the excitation back to the $|\mathrm{T}_0\rangle$ the excitation eventually will decay away. In general the decay of the triplet destroys the coherence and produces distinguishable photons. However, the decay of the states $|\mathrm{T}_i \downarrow\uparrow\rangle$ and $|\mathrm{T}_i \uparrow\downarrow\rangle$ produces indistinguishable photons within the limits of Eq. 4.4. Therefore the coherences between the nuclear spin states $|\downarrow\uparrow\rangle$ and $|\uparrow\downarrow\rangle$ survive the decay and the nuclear spins remain entangled. The limits of Eq. 4.4 can be explained in terms of the hyperfine interaction. For small hyperfine couplings the generation of nuclear spin entanglement is slow and is possible that triplet state has already decayed before sufficient entanglement is formed. This violates the left hand side of the Eq. 4.4. On the other hand very large hyperfine couplings would produce distinguishable photons and in that case the decay of the triplet cannot preserve the nuclear coherence (violation of the right hand side of Eq. 4.4).

4.3 Preparation

In order to test the feasibility of the above proposal we perform pulsed EPR experiments on the diethyl fullerene malonate (DEFM) a molecule with one spin labeled ^{13}C, I = 1/2 nuclear spin (Fig. 4.3). Although this system has one nuclear spin, the extraction of parameters such as the triplet state lifetimes, the initial polarisation and the hyperfine coupling allow their evaluation with respect to the theoretical proposal.

DEFM was prepared by the procedure reported in reference [CH97]. DEFM powder was dissolved in deuterated toluene-d8 at a concentration of $4.5{\cdot}10^{-4}$ M. The solutions were degassed by five cycles of freeze pump-thaw, flash frozen in liquid nitrogen and sealed off on a high vacuum line.

EPR measurements on the photo-excited paramagnetic state of DEFM were performed at X-band (9.47 GHz) on a Bruker Elexsys 580e spectrometer, equipped with a helium-flow cryostat. Photo-excitation was performed using a 532 nm pulsed Nd-YAG laser with 10 Hz repetition rate, 7 ns pulse length and 10 mJ per pulse.

4.4 Characterisation

4.4.1 Electron spin echo experiments

We perform field sweep (FS ESE) experiments using 16ns and 32ns pulses for the $\pi/2$ and π respectively, separated by time τ = 300 ns and we obtain the spectra shown in Figure 4.4 (blue trace). The ESE field sweep has a polarization pattern of absorption / emission). For the simulation of the ESE field sweep spectra we use Easyspin, a Matlab package [SS06] and we extract the g-tensor, the zero field splitting parameters (ZFS) D, E and the relative population differences between the triplet sublevels. The intensity of the spectrum is proportional to the population difference between the levels involved in the relevant

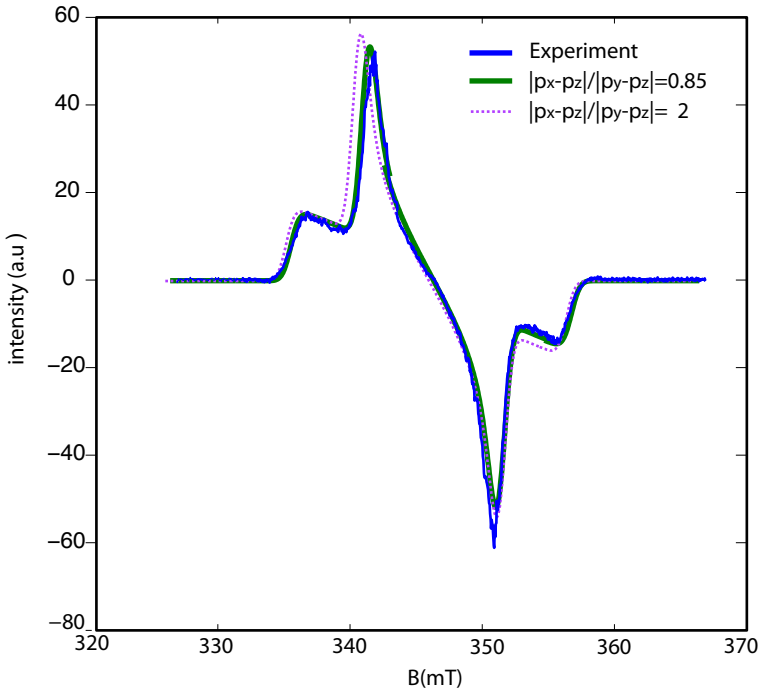


Figure 4.4: (blue trace) Electron spin echo field sweep (ESE FS) of the DEFM system. The spectrum is symmetric and has a polarization pattern of absorption-emission. By fitting the spectrum we are able to determine the $g-$tensor, the ZFS parameters and the zero field population of the triplet sublevels. (green trace) Fitting of the experimental spectrum using a polarization ratio of 0.85 (pink trace).The pink trace is a fitting of the spectrum using the same parameters extracted from our experiment and a polarization ratio of 2, reported in Ref.[BPTM04]. The swap of the population between the x, y sublevels introduces a shift of the center peaks which correspond to molecules with their z axis parallel to the magnetic field.

transitions.

Previous studies employing TREPR methodology on the DEFM have also determined these values. We review these studies and we compare them to our data and to the unfunctionalized fullerene C_{60}.

Comparison with previous studies

In Chapter 2 we discussed the FS spectrum of the fullerene C_{60}. The FS spectrum obtained in crystals in W-band [BHP+98] is asymmetric in high and low fields Figure 2.9.

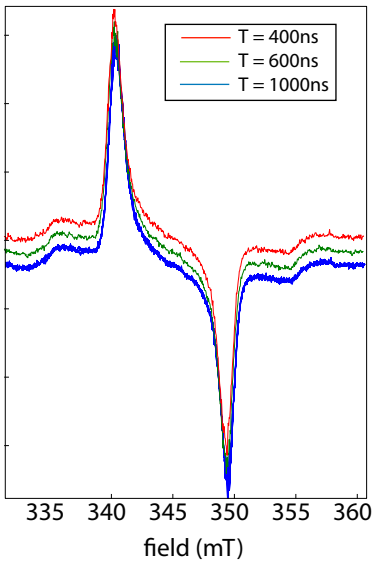


FIGURE 4.5: FS ESE spectra at different delay times after the laser pulse. For delays up to $1\mu sec$ no change in the lineshape is observed.

The DEFM field sweep of TREPR experiments in films and nematic liquid crystals at 240GHz [BPTM04, BFTM06] reveals a similar lineshape to the unfunctionalized C_{60}. The FS spectra extracted from our experiments in contrast to these studies, is symmetric. The symmetric shape of the spectum in X-band compared to the spectra obtained at higher frequencies (240GHz) indicates that the g- anisotropy ($g_{aniso} = 0.0015$) cannot resolved at X-band. A similar behaviour is observed in the fullerene C_{70} in X and W band [DPW^{+}98].

In our studies we adopted the g-tensor reported in Ref. [BPTM04], $g_{xx} = 2.00065, g_{yy} = 2.00115, g_{zz} = 2.00215$ and we determined the zero field splitting parameters, $D = -296$MHz and $E = -6$ MHz. The negative value of the zero field splitting tensor is consistent with the negative D of the fullerene C_{60}. In our study, the slighltly broader spectra is verified by the larger absolute value of the D tensor compared to a $D = -286$MHz of Ref. [BPTM04]. The small value of E reveals that DEFM is largely axially symmetric.

The accurate fitting of the spectra requires knowledge of the population of the triplet sublevels. In the work of Bortolus *et al* [BPTM04], for a negative D the levels are populated

in the following manner: $p_x, p_y > p_z$, similar to the polarization pattern of the fullerene C_{60}. The reported polarization ratio is $|p_x - p_z|/|p_y - p_z| = 2$. In our case the same relation holds for a negative D but the polarization ratio is $|p_x - p_z|/|p_y - p_z| = 0.85$. Since the population of the z sublevel is very small compared to x, y, the above relations indicate that in our experiments the y level is more populated. Considering the above, we compare the effect of the different population ratios to the FS spectra under the same g-tensor and ZFS parameters[2] (Figure 4.4, (pink and green traces)). The swap between the populations of the x and y level in the two experiments, affects more the inner maxima of the spectrum which heavily depend on molecules that their ZFS structure axis x or y is parallel to the magnetic field.

We also perform experiments in which we vary the delay time after the laser flash and we record the echo at 5K. The spectra did not reveal any change at delays up to 1μs (Fig.4.5). Experiments with longer delays would probably gave us better insight about the relative decay of the main and side peaks, like in the case of the phosphine molecule (DFMPH) where we used delay times up to 750 μs (see Chapter 6).

The FS-ESE has also been obtained at various temperatures from 5 to 50K. No lineshape variations were observed indicating that no pseudorotation effects, contribution from other triplets or T_1 relaxation between the triplet sublevels are present.

4.4.2 Relaxation Kinetics

Having characterised the triplet state, we perform relaxation kinetics experiments to extract the absolute population and the decay rates of the triplet state in the presence of a magnetic field. Upon the application of a magnetic field the distribution of the population and the decay rates to the singlet state changes in an orientation dependent manner. The triplet

[2]Using the reported larger D value the spectrum simply gets wider.

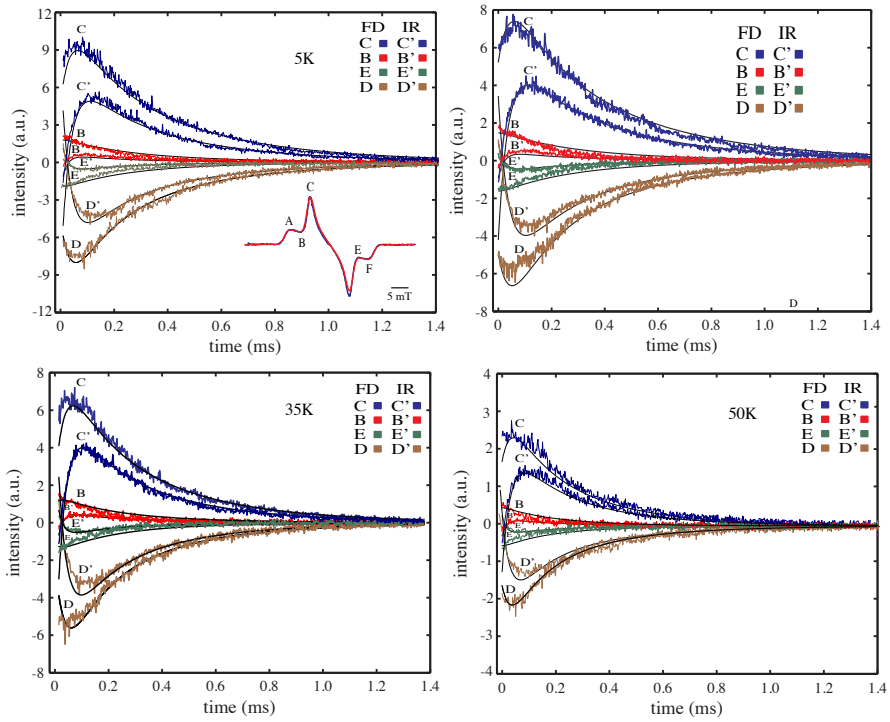


FIGURE 4.6: Decay traces of flash delay (FD) and inversion recovery (IR) experiments and their simulated spectra. The experiments were performed at temperatures from 5-50K and the lineshape remained unchanged whithin this temperature range. This is in agreement with previous studies showing that at low temperatures, spin lattice relaxation effects are negligible. The lifetime of the triplet state is 100 μs.

relaxation kinetics were studied at 5 K, 20 K, 35 K and 50 K, through flash delay-ESE ($hv - T - \pi - t - \pi/2 - echo$) and inversion recovery ($\pi - T - \pi/2 - t - \pi - echo$) experiments, at four different fields in the EPR spectrum (Fig.4.6).

Method

The dynamics were simulated by averaging a weighted contribution of the spins for all the orientations at different magnetic fields, including a variation in the tip-angle of the inversion pulse as a function of off-resonance. Since both the rates and the initial populations are properties of the triplet eigenstates at zero magnetic field we write the

in-field eigenstates in the appropriate basis.

$$|\mathrm{T}_i\rangle = a\,|\mathrm{T}_x\rangle + \beta\,|\mathrm{T}_y\rangle + \gamma\,|\mathrm{T}_z\rangle \tag{4.5}$$

where the coefficients (α, β, γ) used to derive the initial population n_i and decay rates to the single ground state k_i for each triplet sub-level, $n_i = \alpha n_x + \beta n_y + \gamma n_z$ and $k_i = \alpha k_x + \beta k_y + \gamma k_z$. Then, we identify the relevant transitions and multiply the weights of every orientation in each magnetic field. For the simulations we use only one set of $n_{x,y,z}$ and $k_{x,y,z}$ to fit the data for all four fields.

The initial rise of the flash delay curves until about 80 μs reveals that the population difference increases over time as one level decays much faster compared to the other one. After 80 μs the short lived level empties out and a decay is observed. From the fitting we obtain the parameters shown in Table. 4.1.

Temperature (K)	Population $(n_x : n_y : n_z)$	Lifetime (ms) $(1/k_x : 1/k_y : 1/k_z)$
50	0.48 : 0.51 : 0.0	0.25 , 0.45 , 0.015
35	0.46 : 0.54 : 0.0	0.37 , 0.52 , 0.017
20	0.46 : 0.54 : 0.0	0.50 , 0.58 , 0.020
5	0.46 : 0.54 : 0.0	0.45 , 0.58 , 0.018

Table 4.1: We present the relaxation dynamic parameters of the spectra shown in Figure 4.6 at four temperatures. In all cases the levels x and y are more polarized and carry almost equal population. The level y has the longest lifetime which is about 580 μs

The results show that the populations and the decay rates are temperature independent and the lifetime of the triplet state is approximately 100 μs. In the inversion recovery experiments the signal recovers at 150μs. The maximum occurs at a timescale that allows for the application of radiofrequency pulses and the performance of hyperfine studies for the determination of the interaction between the triplet and the ^{13}C.

4.4.3 Hyperfine Studies

We perform Mims ENDOR experiments at six magnetic fields within the X-band EPR spectrum and the obtained spectra together with the corresponding fittings are shown in Figure 4.7. Each spectrum reveals three ENDOR peaks. The main sharp peak which appears at 3.8 MHz represents the Larmor frequency of the ^{13}C and the peak on the left, at $\sim$2.3 MHz is the Larmor frequency of the deuterium nuclei in the solvent (d-toluene). The third peak, which is quite broad compared to the Larmor peaks, is field dependent and results from the hyperfine interaction between the triplet spin and the ^{13}C nuclear spin of the adduct. The peak is broad due to the anisotropy of the hyperfine interaction and the field dependence indicates that a different subset of spins with different orientations is excited in every field position.

By fitting simultaneously all of the six Mims spectra we extract a hyperfine tensor. The hyperfine interaction was found to be axial, $A_{xx} = A_{yy} = 2.6 \pm 0.1$, $A_{zz} = 0.74 \pm 0.02$ MHz and a 20% Gaussian strain is applied to the A values across the sample.

4.5 Ab initio calculations

For an atomic scale understanding of the hyperfine interaction we perform first principle calculations within density functional theory. The isotropic hyperfine coupling constants of the ^{13}C nuclei were determined using the s-wave component of the all-electron spin density at the nuclear sites, according to the method of Ref. [WB93].

Initially we calculate the hyperfine interaction of the mono-DEMF and we compare it to the experimental results. The accuracy of the calculations allows us to go further and perform calculations on the $trans-1$ DEFM, the structure we considered initially and could realise the theoretical scheme.

We consider optical excitations to spin triplet states in the DEFM and $trans-1$ DEFM

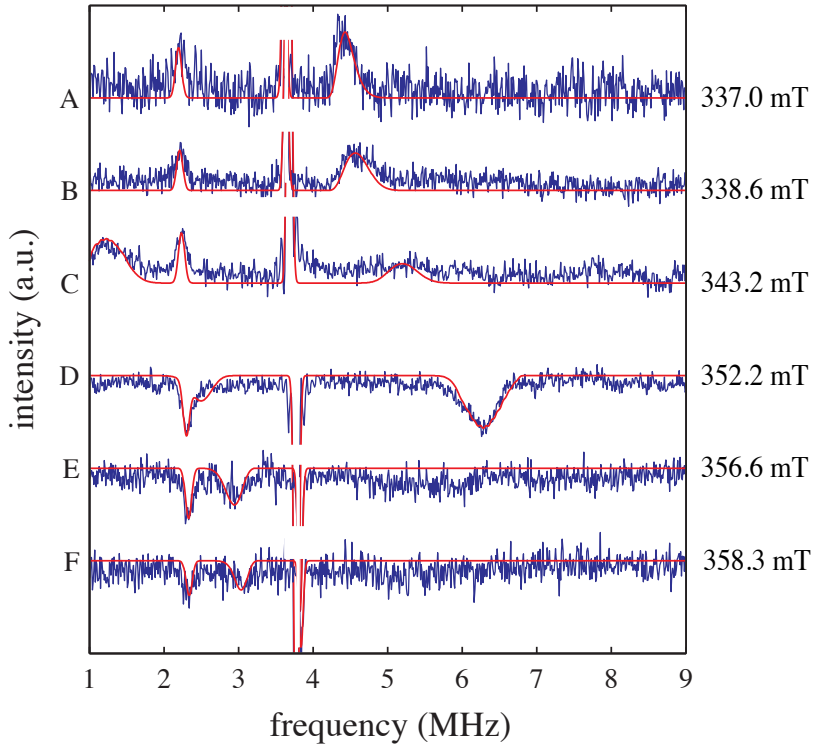


Figure 4.7: Mims ENDOR experiments at six magnetic fields, acquired at 20 K and their corresponding simulations. The most intense peak around 3.8 MHz, represent the ^{13}C Larmor frequency at this field and corresponds primarily to nuclear spin transition frequency within the T_0 subspace. Weak shoulders around this peak are attributed to weak unresolved coupling to ^{13}C in the solvent (d-toluene). Similarly, the peak at 2.3 MHz arises from weak coupling to deuterium nuclear spins in the solvent. Finally, also observed in the ENDOR spectrum is a peak with shows a strong field dependence, arising from the ^{13}C nuclear spin transition in the T_+ and the T_- subspace which is a function of the anisotropic hyperfine interaction.

functionalized fullerenes. The calculations were performed within the local density approximation (LDA) [CA80], [PZ81] and core-valence interaction was taken into account by using norm-conserving pseudopotentials [TM91, FS99].

The electronic wavefunctions were described by a plane wave basis with a kinetic energy cutoff of 60 Ry. We used simulation cells of size 21 Å and 24 Å for DEFM and $trans-1$ DEFM respectively which correspond to an inter-molecular separation of at least 10 Å . For all the calculations we used the Quantum-ESPRESSO package [GBB$^+$09]. We performed

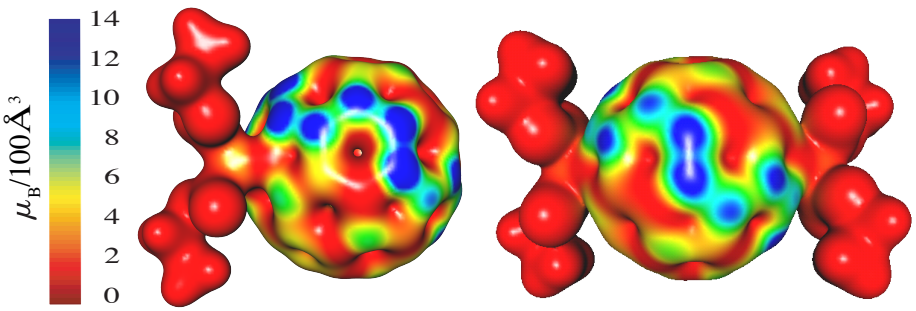


FIGURE 4.8: Spin density in the lowest triplet excited state of DEFM and trans-1 DEFM fullerenes. The chosen charge isosurface has an isovalue of 0.07 electron=$\mathring{A}^3$ and the overlaid color indicates the magnitude of the spin density. The spin density is mostly gathered around the fullerene cage.

calculations in singlet and triplet states and we found that the triplet excitation energies for both structures are 1.30 eV and 1.33 eV and in agreement with previous studies [HCG$^+$94] [SZC96].

To determine the ground-state structural configuration of the mono-diethyl malonate C_{60} we relaxed three different conformations with symmetries C_s, C_2, or C_{2v}. The molecules with C_2 or C_s symmetry were found to be almost degenerate in energy (within 5 meV), and more stable than the molecule with C_{2v} symmetry by 0.32 eV. The excitation to the spin-triplet state was studied in detail for the molecule with C_2 symmetry. The same point group is predicted for DEFM in reference [BPTM04].

By relaxing the $trans-1$ DEFM structure, we found that the lowest energy configuration carries C_2 symmetry. In Figure 4.8 we present the electron density colour mapped with the spin density. On the ^{13}C of the DEFM, the spin polarization although small, is not zero. The spin polarisation is gathered around the fullerene cage while the adducts have almost

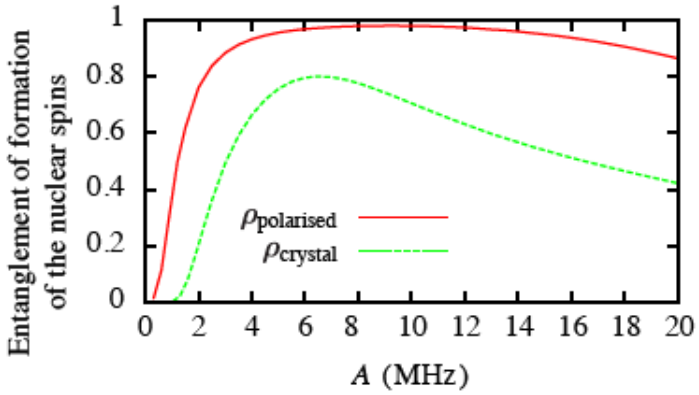


Figure 4.9: a) Entanglement of formation of the nuclear spins after the application of the theoretical protocol. The red trace is the entanglement of formation of a completely polarized T_+ or T_- state. For a maximum entanglement of formation a hyperfine interaction of 6-14MHz is required. The red trace represents the entanglement of formation of the trans-1 DEFM system employing the populations and the decay rates of the DEFM, under the assumption that are quite similar. In this case the partial polarization of the levels T_+ or T_- allow for the application of the protocol twice in succession. For a hyperfine interaction of 3 MHz the maximum entanglement of formation is > 0.5.

zero polarisation. The image was rendered using Gabedit. [Alo]

For the calculation of the hyperfine couplings we determine the spin density which is given as a grid of values. By careful assignment of each value of the grid, to a specific atomic position we are able to obtain the spin densities on the nuclear spin ^{13}C. After the determining the spin density the extraction of the hyperfine interaction in trivial. Using the relation

$$a = \frac{8\pi}{3} g_e \mu_e g_l \mu_l \rho_s(\mathbf{R}), \tag{4.6}$$

where ρ_s is the electron spin density, g_e the free-electron g-factor, μ_e the Bohr magneton, g_l and μ_l are the gyromagnetic ratio and the nuclear magneton, we calculate HF coupling constants of the ^{13}C nuclei in DEFM and $trans-1$ DEFM C_{60} to be 4 MHz and 2.2 MHz, respectively. These values are in approximate agreement with our relatively small measured HF coupling which is 2 MHz for the DEFM.

4.6 Realization of the theoretical proposal

We now examine how the results we extracted from the experiments and the calculations can be applied to the theoretical proposal. For the application of the protocol we derive the in-field populations and the decay rates of the triplet state, T_-, T_0, T_+ . We find that the populations and the lifetimes are $p_- = 0.49$, $p_0 = 0.02$, $p_+ = 0.49$ and $\tau_- = 0.57$ ms, $\tau_0 = 0.02$ ms , $\tau_+ = 0.57$ ms, respectively. We observe that the laser excitation produces a fast relaxing T_0 and partial electronic polarization on the T_- and T_+ sublevels. This polarization pattern indicates that the entangling protocol has to be applied twice in succession for the two states, T_+ and T_-. Initially, a microwave pulse flips the state of the excitation from T_0 to T_+ (we can also start from T_-). Since the entangling dynamics proceed fast in these subspaces entanglement is created in the T_+ before the decay of the triplet state. However in order to avoid unwanted evolution which would unwind the entangling state we apply another microwave pulse which takes us to the quickly decaying T_0 state. The protocol is applied once more for the long lived T_- subspace and after entanglement is generated in another period of time (at another odd integer of t see Fig. 4.2) a microwave pulse is used to swap the population between T_0 and T_-. Ideally after the decay of the excitation a maximally entangled nuclear spin state is generated. As it was mentioned above one of the most important parameters in this scheme is the strength of the hyperfine interaction. Considering the extracted values of the relaxation times as representative values, we first examine the effect of the hyperfine coupling on the entaglement of formation. If we assume a two-nuclear spin system such as the bis-adduct molecule we studied through DFT, we see that a hyperfine coupling of 3 MHz leads to and entanglement of formation of up to $\sim$0.85MHz assuming a fully polarized starting state (see red trace of Figure 4.5). Taking into consideration the finite polarization of the initial state observed in our experiments (green trace of Figure 4.5), this is limited to $\sim$0.5. In general maximum entanglement of

formation can be achieved for hyperfine couplings between 4-14 MHz. In order to optimise the entanglement of formation, we require structures that exhibit higher hyperfine interaction. By regarding the hyperfine interaction as a tunable parameter and we can explore the use of different functional groups in molecular systems to yield gates of greater entangling power.

4.7 Conclusions

Our experiments on the DEFM molecule show the feasibility of the proposal to create entanglement between two nuclear spins through their mutual interaction with a photo-excited mediator. The success of this protocol depends on a balance between the characteristic time required to perform an entangling operation, the lifetime of the triplet exciton, the decoherence time of the entangled state and the in-field population of the triplet levels.

In the next chapter we present a DFT based study of a series of regioisomeric fullerene structures with two nuclear spins for the prediction of a candidate system with the desired properties that could realise best the theoretical proposal.

5

Hyperfine studies for nuclear entanglement in excited states

5.1 Introduction

In the previous chapter we presented a proposal for entangling two nuclear spins using a photo-excited transient electron spin [SFK+10] and we quantified the efficiency of entanglement using the strength of the hyperfine interaction (HFI). We also performed theoretical

calculations using the PAW reconstruction and we calculated the isotropic hyperfine interaction. Here, we are going to present more detailed hyperfine studies using the Gauge Invariant Projected Augmented Wave method (GIPAW) for the extraction of the whole hyperfine tensor. Initially we test the accuracy of our methods by studying small radicals and then we apply these methods to a set of regioisomeric fullerene derivatives. These calculations allow us to screen candidate systems for nuclear spin entanglement prior to their experimental synthesis. Finally, we will discuss our results in the light of the theoretical proposal described in the previous chapter.

5.2 Calculation of the hyperfine tensor from first principles

In Chapter 2 we presented the Hamiltonian of a molecular system in the triplet state and we gave a brief description of the hyperfine interaction term between an electron and a nuclear spin. The coupling of an electron spin $\vec{S}$ to N nuclear spins, $\vec{I_l}$, $l = 1, \dots N$ is described by the following term :

$$\hat{H} = \sum_{l=1,N} \vec{S}^T \mathbf{A}^{(l)} \vec{I_l}, \tag{5.1}$$

where $\mathbf{A}^{(l)}$ is the hyperfine coupling tensor associated with the l-th nucleus at the position $\mathbf{R}_l$. The hyperfine tensor can be written as $A_{ij}^{(l)} = a^{(l)}\delta_{ij} + b_{ij}^{(l)}$, where $a^{(l)}$ is the isotropic hyperfine interaction (Fermi contact term) and $b_{ij}^{(l)}$ the traceless tensor which gives the anisotropic or dipole-dipole hyperfine interaction [Blö94]

$$a^{(l)} = \frac{8\pi}{3} g_e \mu_e g_l \mu_l \rho_{\mathrm{s}}(\mathbf{R}_l), \tag{5.2}$$

and

$$b_{ij}^{(l)} = g_e \mu_e g_l \mu_l \int d\mathbf{r}' \frac{3 r_i' r_j' / r'^2 - \delta_{ij}}{r'^3} \rho_{\mathrm{s}}(\mathbf{r}'). \tag{5.3}$$

$\rho_{\mathrm{s}}(\mathbf{r}) = \rho_{\uparrow}(\mathbf{r}) - \rho_{\downarrow}(\mathbf{r})$ is the electron spin density, g_e the free-electron g-factor, μ_e the Bohr magneton, g_l and μ_l are the gyromagnetic ratio and nuclear magneton of the l-th nucleus, respectively. In Eq. (5.3) $\mathbf{r}' = \mathbf{r} - \mathbf{R}_l$ and $r' = |\mathbf{r}'|$. The anisotropic tensor $b_{ij}^{(l)}$ is conventionally given in terms of its eigenvaules $b_{xx}^{(l)}$, $b_{yy}^{(l)}$, and $b_{zz}^{(l)}$.

The extraction of the HFI parameters using the above equation Eqs. (5.2) and (5.3) requires the calculation of the electron spin density. In the dipole-dipole term $b^{(l)}$, the electron spin-density is weighted by the factor r^{-3} showing that contributions outside of the core region are dominant. The Fermi contact term is proportional to the spin density inside the core region and arises from orbitals of s-character.

5.3 Core Polarization

For the calculation of the Fermi contact term simple pseudopotential methods fail to reproduce accurately the oscillating wavefunction near the nucleus. The neglect of the core electrons in pseudopotential methods in some cases imposes a significant error in the calculation of the Fermi contact term. Early studies using Hartree Fock methods showed the high impact of the the spin polarized states at the nuclei, in systems with singly occupied molecular orbitals (SOMOs) of a non s-like character [FW60, WF61]. Thus, it was early understood that pseudopotential methods need to be modified in order to calculate accurately the core contribution. The PAW method as we mentioned, attempted to reconstruct the full nodal form of AE wavefuncition inside the core region and has been successfully applied to the calculation of hyperfine parameters of systems with s-like SOMO, for example, hydrogen defects in silicon [WB93]. In our calculations we use the perturbative core level polarization (PCLP), approach which incorporates the core polarization and provides

accurate results by taking into account contributions from the core and valence regions [BSK07]. The spin density is given by the following relation :

$$\rho_{\uparrow,\downarrow}(\mathbf{r}) = \rho_{\mathbf{v},\uparrow,\downarrow}(\mathbf{r}) + \rho_{\mathbf{c},\uparrow,\downarrow}(\mathbf{r}) \tag{5.4}$$

where v and c the valence and core contributions. In this method the AE wavefunction is reconstructed by a pseudowavefunction within the frozen core approximation and the new pseudo-AE wavefunctions are used to develop an effective perturbing density functional potential

$$\Delta V_{eff} = \Delta V_{\uparrow} - \Delta V_{\downarrow} = -\frac{2}{\pi}\frac{\rho^{SOMO}(\mathbf{r})}{\rho^{\hat{2/3}(\mathbf{r})}} \tag{5.5}$$

This potential is used to estimate the spin-polarised core levels by a first order perturbation theory

$$\rho_s^c(r) = \rho^{c\uparrow}(\mathbf{r}) - \rho^{\mathbf{c}\downarrow}(\mathbf{r}) = \mathbf{4}\sum_{\mathbf{core}}^{\lambda}\mathbf{Re}[\langle\phi|(\mathbf{r})\sum_{\kappa\neq\lambda}\mathbf{C}_{\lambda\kappa}\langle\mathbf{r}|\phi_{\mathbf{k}}\rangle] \tag{5.6}$$

where $\phi_{\lambda,\kappa}$ are the partial waves of the levels λ, κ with the corresponding eigenvalues $\epsilon_{\lambda,\kappa}$ and $C_{\lambda}\kappa$ is

$$C_{\kappa\lambda} = \sigma\frac{\langle\phi_\kappa|\Delta V_{eff}|\phi_\lambda\rangle}{\epsilon_\lambda - \epsilon_\kappa} \tag{5.7}$$

...but how does the PCLP method work?

From equation Eq. (5.5) we see that V_{eff} depends on the character of the singly occupied molecular orbitals. In s-like orbitals the V_{eff} expands outside the core region and the spin polarization in the core is quite small. In s-like SOMOs there is a dominant isotropic HFI A_{iso}, but A_{aniso} is negligible. However, if the SOMOs have a p- or d- like character, V_{eff} becomes more localized inside the core region creating a large spin polarization among the core orbitals. In this case both core and valence spin-polarized levels contribute to A_{iso}

while the A_{aniso} which depends heavily on the SOMO is not affected by the spin polarized core levels. This shows that in both cases the neglect of core spin polarization does not have a significant impact on the A_{aniso} but for A_{iso}, especially in systems of non s-like character, can produce wrong results. In order to establish the accuracy of our methods, in the calculations that follow we calculate the HFI of small radicals, we discuss the impact of core polarisation correction to the HFI and we compare the results to the experiment.

5.3.1 Computational method

We perform density-functional theory calculations within the generalized gradient approximation of Perdew, Burke, and Ernzerhof (PBE) [PBE96]. The valence electronic wavefunctions are described by using a planewave basis set with a kinetic energy cutoff of 70 Ry and the core-valence interaction is taken into account using Troulier-Martins norm-conserving pseudopotentials [TM91, FS99]. For the calculation of the HFI tensor we use the gauge-including projector-augmented wave method (GIPAW) of Ref. [PM01]. All the calculations are performed using the quantum-ESPRESSO software package [GBB$^+$09]. In addition to pseudopotential calculations, we also perform all-electron density-functional calculations using the PBE exchange and correlation, as implemented in the Gaussian'09 program package [FTHBS$^+$09].

For the all-electron calculatiosn of the HFI tensor we adopt the EPR-II basis, which has been purposely designed to accurately describe the Fermi contact term [Bar96b].

5.4 Calculations on the small radicals

We performed calculations for the following small radicals (Figure 5.1) containing hydrogen and oxygen: CH_2CH_3, CH_2CH, CO_3, H_3CO, HCO, H_2CO^+, and CH_3. For our calculations we use a cell diameter of 12 Å and a cutoff energy of 70 Ry. In order to determine the

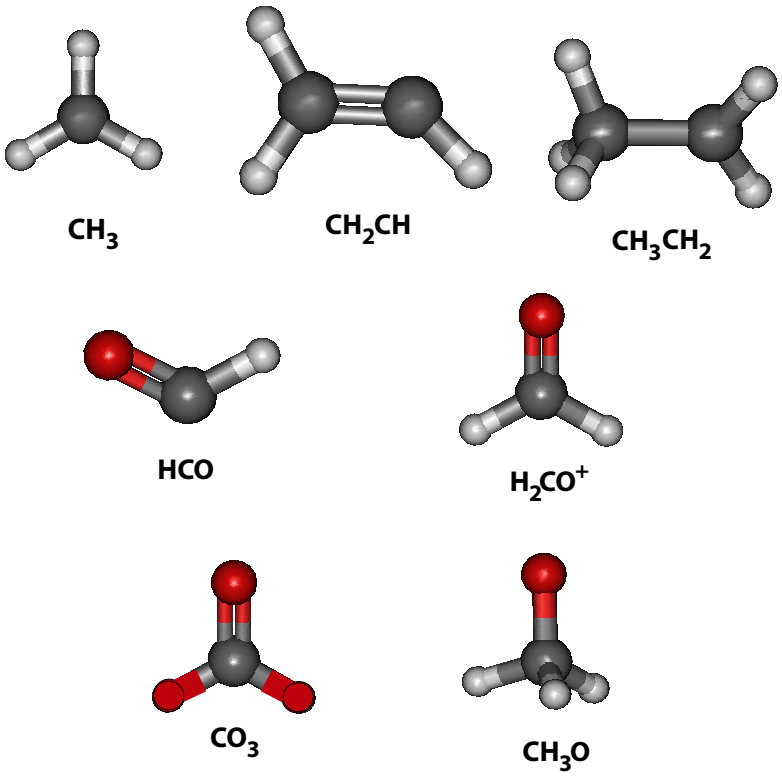


FIGURE 5.1: Schematic illustration of the small organic radicals. The carbons are marked with grey color while hydrogens and oxygens with white and red, respectively.

variations of the hyperfine interaction with respect to the cutoff energy we perform calculations within a range of 30-150Ry. In all cases the hyperfine interaction does not vary by more than 1 MHz.

5.5 Results and Discussion

5.5.1 HFI parameters of small molecules

In Table 5.1 we present the results of our methods and we compare them to the experiment and to all electron methods. For a quantitative analysis we present both pseudopotential plane wave results with (PW-SCP) and without (PW) core polarization correction [BSK07].

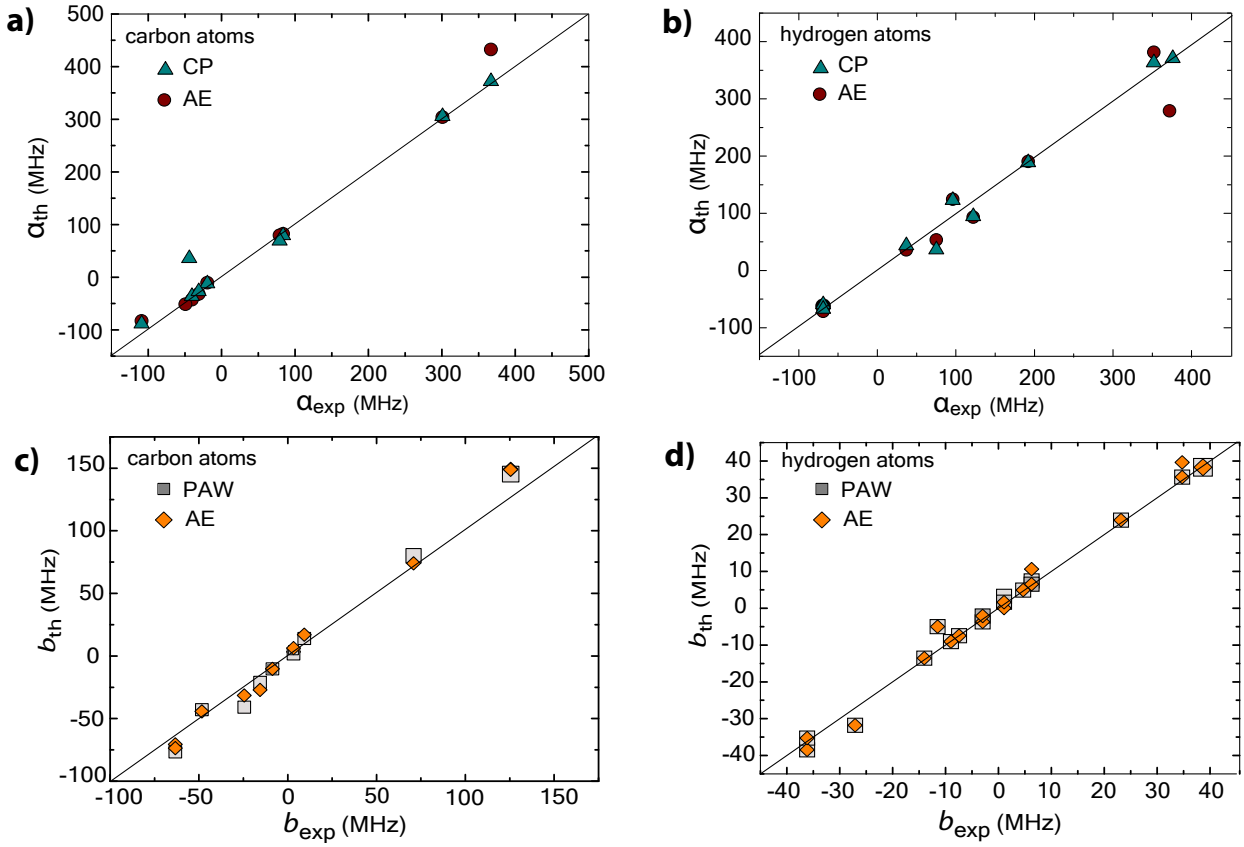


Figure 5.2: Comparison of the hyperfine interaction in AE and PW-SCP methods. The isotropic hyperfine interaction (a,b) and anisotropic (b,c) hyperfine interaction is calculated for carbon and hydrogen atoms. The PW-SCP are in very good agreement with AE calculations and in most cases the results differ only by a few MHz. The average error for the PW-SCP methods is estimated around 12% while the error in AE calculations is 15%.

From the PW calculations we see that in cases like the CH_3 and CH_2CH where the ^{13}C atoms reveal the largest discrepancy with the experiment, the PW-SCP reproduces accurately the experimental measurements. For the ^{1}H no spin polarization effects are observed and a very good agreement holds between theoretical methods and experiment.

In Figure 5.2(a,b) we plot the isotropic hyperfine interaction for the carbon and hydrogen atoms using AE methods and pseudopotential calculations. The results are expected to coincide with the diagonal and the estimated errors using PBE functionals are no more than 8% for PW methods while for AE methods the error is estimated around 15%. We

Molecule	Atom	Fermi contact HFI (MHz)				
		PW	CP	AE	Exp.	
CH_2CH	C	397	305	306	302	[a]
	H	125		124	96	
	H	191		190	192	
	C	-27	-17	-18	-24	
	H	38		43	37	
CH_2CH_3	C	205	81	79	83	[b]
	H	-63		-61	-69	
	C	-40	-38	-34	-38	
	H	51		40	75	
CO_3	C	-31	-31	-28	-32	[c]
H_3CO	H	94		95	122	
	C	-35	44	-37	-44	[d]
HCO	H	379		367	356	
	C	435	428	389	367	[e]
H_2CO^+	H	279		372	372	
	C	-76	-83	-87	-109	[f]
CH_3	C	214	79	72	80	[g]
	H	-69		-66	-69	

Table 5.1: We report calculations using the GIPAW method without accounting for core-polarization effects (PW), calculations within GIPAW including core-polarization corrections (CP), all-electron calculations (AE), and measured Fermi contact parameters. The atoms are listed in the same order they appear in the chemical formula.

[a] Ref.[FS63], [b] Ref.[OW61], [c] Ref.[CHMW62], [d] Ref.[MEHS88],

[e] Ref.[Hol69], [f] Ref.[KS88], [g] Ref.[Chi92].

Molecule	Atom	Dipolar HFI (MHz)				Molecule	Atom	Dipolar HFI (MHz)			
		Axis	PW	AE	Exp.			Axis	PW	AE	Exp.
CH_2CH		b_{xx}	-86	-72		H_3CO		b_{xx}	7	6	
	C	b_{yy}	-64	-56			C	b_{yy}	2	2	
		b_{zz}	148	127				b_{zz}	-9	-8	
		b_{xx}	37	37	38 [h]			b_{xx}	-8	-7	
	H	b_{yy}	-6	-6	-11		H	b_{yy}	-4	-4	
		b_{zz}	-32	-32	-27			b_{zz}	12	12	
CH_3CH_2		b_{xx}	-3	-3		HCO		b_{xx}	-43	-42	-48 [c]
	C	b_{yy}	1	1			C	b_{yy}	-33	-38	-24
		b_{zz}	3	2				b_{zz}	76	80	72
		b_{xx}	-83	-73				b_{xx}	-14	-14	-14
	C	b_{yy}	-82	-72			H	b_{yy}	-8	-7	-8
		b_{zz}	165	145				b_{zz}	23	21	23
		b_{xx}	-4	-5		H_2CO^+		b_{xx}	-25	-21	-15 [k]
	H	b_{yy}	-4	-4			C	b_{yy}	7	6	4
		b_{zz}	8	9				b_{zz}	18	16	10
		b_{xx}	35	38	35 [i]			b_{xx}	-10	-10	-9
	H	b_{yy}	2	0	1		H	b_{yy}	-8	-7	5
		b_{zz}	-38	-38	-36			b_{zz}	18	18	4
		b_{xx}	-4	-4	-3	CH_3		b_{xx}	-70	-74	-63 [l]
	H	b_{yy}	-3	-3	-3		C	b_{yy}	-72	-74	-63
		b_{zz}	7	9	6			b_{zz}	150	148	127
CO_3		b_{xx}	5	4	4 [j]			b_{xx}	-36	-39	-36 [m]
	C	b_{yy}	5	4	4		H	b_{yy}	-1	-1	1
		b_{zz}	-9	-9	-8			b_{zz}	35	39	35

[h] Ref.[IET70], [i] Ref.[SYL74], [j] Ref.[CHMW62], [c] Ref.[Hol69],

[k] Ref.[KS84], [l] Ref.[Fes67], [m] Ref.[JVF71].

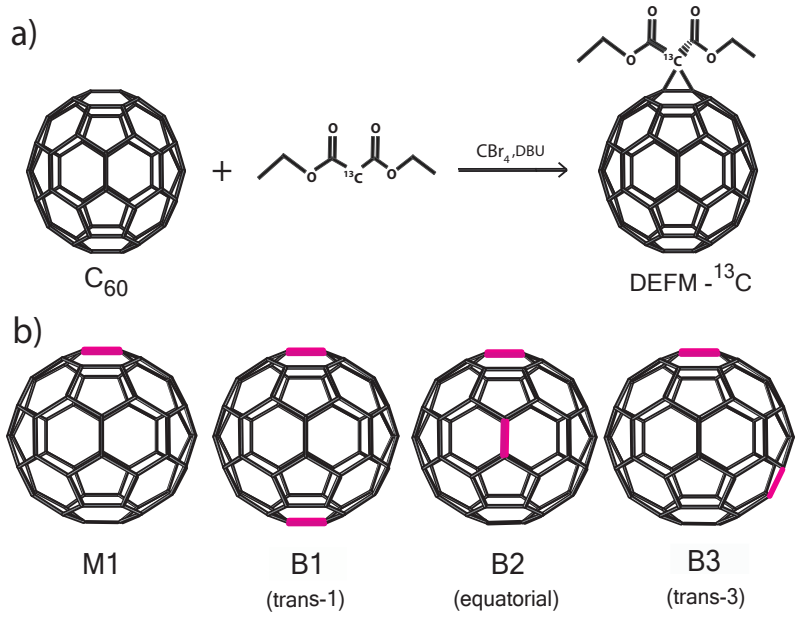


FIGURE 5.3: (a) Left: schematic representation of the diethyl malonate ($C_7H_{12}O_4$) C_{60} mono-adduct (M1). The bridging ^{13}C atom carrying a nuclear spin is indicated, H atoms are not shown. Right: simplified representation with the red bond indicating the anchoring point of the adduct on the C_{60} cage. (b) Simplified representation of three regioisomeric diethyl malonate fullerene bis-adducts (B1-B3).

also calculate the dipolar hyperfine couplings and we report the results in Table 5.2. In this case we observe that the dipolar hyperfine interaction is not affected by the spin polarisation. The error for PW methods is 16%, while for the AE methods the error was estimated around 15%. These results are in excellent agreement with experiment and all-electron calculations as illustrated in Figure 5.2(c,d) for hydrogen and carbon atoms. After establishing the accuracy of our methods we move on to present HFI calculations for a set of fullerene derivatives. We discuss the effect of the adduct position on the HFI interaction and identify the structure that best meets the requirements for nuclear spin entanglement under the scheme of Reference [SFK$^+$10].

Stuctures

In Reference [SFK$^+$10] we reported preliminary calculations of the isotropic component of the HFI tensor of the M1 system and on a related molecule carrying two ^{13}C nuclear spins [model B1 in Figure 5.3a]. Here we complement this work by calculating the entire HFI tensor and also by extending it to fullerene derivatives with various conformations. In fact, while density-functional theory does not describe correctly excited states, the lowest spin-triplet state of C_{60}, with the HOMO and LUMO states singly occupied with parallel spins, is the ground state of the $S_z = 1$ spin configuration [GL76, KG07]. Here we consider the DEFM, M1 Figure 5.3a, as well as the three regioisomeric bis-adducts $trans-1$, (B1), the equatorial, (B2) and the $trans-3$, (B3) DEFM shown in Figure 5.3b.

During the synthesis of the regioisomeric bis-adducts from the diethyl malonate and fullerene molecules, the B1 in Figure 5.3b is produced with the lowest yield (0.8%), while B2 and B3 are produced with the highest yields (16% and 12%, respectively) [HLK94].

For each structure M1-B3 we optimize several initial geometries in both the singlet $S_z = 0$ and triplet $S_z = 1$ configurations using cells of size up to 24 Å and cutoff energies of 70 Ry. For the calculation of the excitation energy we subtract the energy of the optimised singlet state from the energy of a single point triplet calculation. In all cases the excitation energy was 1.31 ± 0.02 eV. This result is in excellent agreement with the measured excitation energy of 1.30 eV of the non-functionalized fullerene C_{60} [HCG$^+$94, SZC96]. Such agreement suggests that our description of the lowest triplet exciton state is correct.

5.5.2 Hyperfine Interaction in Fullerene Derivatives

Before proceeding to the calculation of the hyperfine interaction we plot the distribution of the spin density Fig. 5.4. Since the hyperfine interaction is proportional to the spin

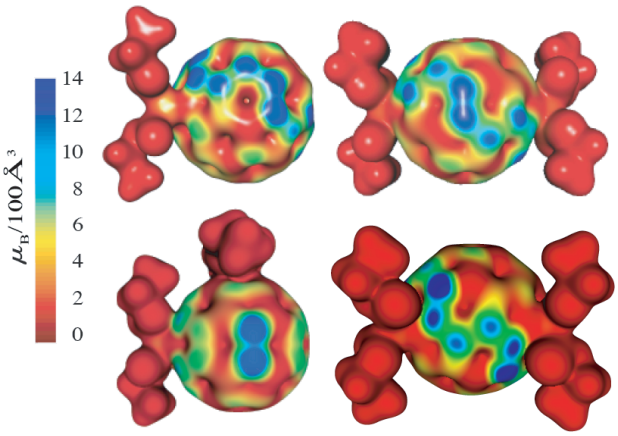


FIGURE 5.4: Spin density in the lowest triplet excited state of the four fullerene derivatives. The isovalue of the spin density isosurface is 0.07 electron/Å^3. The blue color indicates the magnitude of the spin density. In all cases the spin density is mostly gathered around the fullerene cage.

Table 5.3: Hyperfine couplings of the fullerene derivatives in MHz. The HF parameters of M1 are compared to experiment and all-electron (AE) methods. In the case of the B1 the distortion of the structure lifts the symmetry and favours one of the two ^{13}C nuclear spin.

		Dip. Coupl.		
Derivative	a_{iso}	b_{xx}	b_{yy}	b_{zz}
M1(PW)	2.0	-1.6	-2.3	4.0
M1(AE)	1.0	-1.3	-2.0	3.4
M1(Exp.)	2.0	-0.6	-0.6	1.3
B1(1)	1.0	-0.7	-1.2	1.9
B1(2)	1.0	-0.7	-1.2	1.9
B2(1)	0.24	0.03	0.57	-0.59
B2(2)	1.52	-2.3	-2.4	4.7
B3(1)	2.2	-1.21	-1.8	3.1
B3(2)	2.2	-1.21	-1.8	3.1

density we can qualitatively predict the strength of the hyperfine interaction on specific atoms. In Figure 5.4 we observe that the spin density distribution is in all cases localized on the fullerene cage (blue areas) while the adducts carry negligible spin density. This indicates that we should expect, like in the previous work, small hyperfine couplings on the ^{13}C atoms.

The calculations of the full hyperfine tensor using the GIPAW method are presented in Table 5.3. For M1, we also performed all-electron calculations using EPR-II basis. Table 5.3 also shows the isotropic and the principal values of the anisotropic HFI of the three bisadducts.

Table 5.4: Structural details, angles and bond lengths, of the fullerene derivatives in the triplet configuration as shown in Fig.3. The numbers in parenthesis next to the derivatives refer to the two adducts.

Derivative	α, α'	β, β'	γ, γ'	δ	θ	d_1(Å)
M1	125.7°	244.5°	111.6°	112.0°	64.6°	1.58
B1(1)	125.5°	244.9°	111.6°	112.3°	64.5°	1.58
B1(2)	125.5°	244.7°	111.8°	112.5°	64.5°	1.58
B2(1)	125.4°	244.7°	110.5°	110.0°	65.2°	1.60
B2(2)	125.5°	244.9°	110.3°	110.4°	63.7°	1.57
B3(1)	125.5°	245.8°	110.5°	112.8°	64.8°	1.58
B3(2)	124.7°	245.5°	110.5°	112.8°	64.9°	1.58

The different position of the adduct on the fullerene gives rise to different HFI parameters. In the cases of B1 and B3 we observe that the two ^{13}C are equivalent while in the case of B2 one ^{13}C is favoured compared to the other.

In order to explain this finding and investigate the impact of the geometry to the hyperfine interaction we study the different conformations of the C_{60} fullerene, following the notation of the angles and bond lengths of Figure 5.5 (Table 5.4). For the different

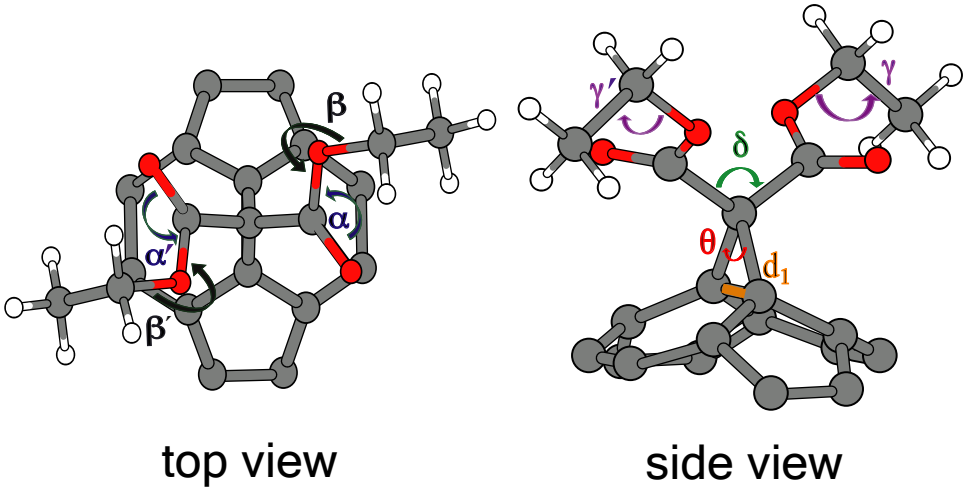


FIGURE 5.5: Representation of the position of the diethyl malonate adduct on a part of the C_{60} fullerene. In Table III we give the values of the angles and the C-C bond length, d_1 for each of the schemes considered, M1 and B1-B3.

fullerene derivatives the adducts are symmetric and the angles vary less than one degree. In most derivatives the C-C bond length of the fullerene where the adduct is attached, is $d_1 = 1.58$Å. In the case of the B2, a slight distortion of the structure yields a larger C-C bond length ($d_1 = 1.60$Å) of one adduct compared to the other ($d_1 = 1.57$Å) showing that one of the two nuclear spins ^{13}C is closer to the fullerene. This is consistent with the larger hyperfine interaction of this atom.The anisotropic hyperfine interaction of M1 using PW methodology coincides with the values from AE methods but it is larger compared to the experimental results.

5.6 Discussion

We can now examine our results in the context of the theoretical proposal that suggests entanglement between two nuclear spins via their coupling to the triplet exciton spin. The optimum value of hyperfine coupling depends on the triplet lifetimes, which likely differ for

the fullerene derivatives we examined here. Nevertheless, using the values extracted for M1 as estimates, it is possible to achieve entanglement of formation > 0.5 when the HFI is in the range 2–16 MHz [15]. An important condition for the entanglement scheme is that the two nuclear spins exhibit very similar coupling to the exciton spin. Our calculations show that the two ^{13}C nuclei exhibit similar HFI with the triplet spin in the case of B1 and B3. In the case of the B2 structure due to a distortion, the HFI strengths differ substantially for the two ^{13}C making B2 not an appropriate candidate for the proposed scheme. These findings indicate the importance of the detailed atomic scale geometry to the definition of the hyperfine couplings. The magnitude of the HFI for B3 ($\sim$2.2 MHz) makes it a promising candidate for nuclear spin entanglement, especially considering that can be produced with high yield of 12% and has equivalent ^{13}C sites.

5.7 Conclusions

In this chapter we presented calculations of the hyperfine interaction in small organic radicals and fullerene derivatives and discussed the results in the context of the generation of nuclear spin entanglement using photo-excited triplets. The calculations support the accuracy of pseudopotential methods in the study of the HFI using the PCLP method. We show that the results obtained from doublet and triplet organic radicals compare well with the experiment and with all-electron methods. After establishing the accuracy of our calculations we determined the HFI in four fullerene derivatives and show that the geometry and the symmetry of the structures play an important role in the determination of the hyperfine couplings. Finally, we identified a particular fullerene derivative structure as an optimal candidate for the realisation of the entanglement of remote nuclear spins using optically excited fullerenes. In general, our work represents a first step towards the synergistic use of DFT-based modelling and electron spin resonance experiments for the design of functional

materials for quantum information technology.

6

Demonstration of entangling gates using the triplet state of DMFPH

In the previous chapters we described how entanglement between nuclear spins could be created in triplet photoexcited states through their mutual interaction with the triplet electron spin, via the hyperfine interaction. Here, we present characterisation studies of the photoexcited triplet state of the phosphine oxide fullerene (DMFPH), a system with two nuclear spins and we show by using quantum state tomography, that an entangling gate between the two nuclear spins can be achieved within the lifetime of the triplet state. For

the characterisation we use EPR and density functional theory to extract the terms of the spin Hamiltonian and the nuclear-nuclear direct coupling is studied through spin electron double resonance (SEDOR) experiments. By employing two different techniques for the implementation of a CNOT gate we show that the nuclear spins can be coupled in very fast timescales, ultimately limited by the duration of a microwave pulse.

6.1 Sample preparation

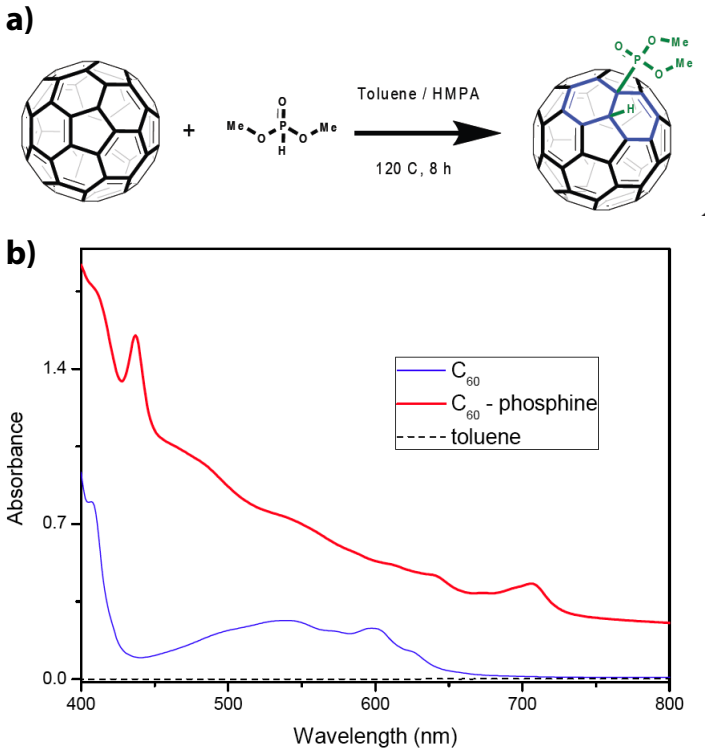


FIGURE 6.1: a) The phosphine oxide fullerene (DMFPH): $(CH_3O)_2P(O)$-C_{60}-H is a fullerene derivative with two nuclear spins directly attached to the fullerene cage, a proton ^1H and a phosphorus ^{31}P. The phosphonate functional group and the proton break the high I_h symmetry of the fullerene. b) The absorption spectra of the DMFPH and the unfunctionalised fullerene C_{60} . The broad absorption band in C_{60} disappears in DMFPH spectra and instead two absorption peaks appear at 430 nm and 710 nm which are characteristic in fullerene derivatives with a saturated double bond (original source: Rizvi Raman, D. Phil thesis 2011).

This Chapter describes a fullerene derivative, the phosphine oxide fullerene (DMFPH), with two nuclear spins, a proton ^{1}H, $I = 1/2$ and a phosphorus ^{31}P, $I = 1/2$, directly attached onto the fullerene cage (Fig. 6.1a).

DMFPH was prepared according to the procedure reported in [ICSN05]. Solutions of DMFPH $4{\cdot}10^{-4}$M concentration in d8-toluene were deoxygenated using five freeze pump thaw cycles, flame sealed under vacuum and flash frozen in liquid nitrogen. EPR experiments of the photoexcited paramagnetic state of DMFPH were performed at Q-band (34 GHz) and X-band (9.7 GHz) on a Bruker Elexys 580e spectrometer equipped with a low temperature helium flow cryostat. A 532 nm pulsed Nd-YAG laser operating at 10 Hz was used as light source for the photoexcitation in X-band, while for the Q-band experiments, an OPO Nd-YAG laser of variable repetition rate was used. In both lasers the pulse width was 7 ns and the power per pulse 10 mJ.

6.2 Time-resolved spectroscopy

The typical energy level diagram of the triplet spin system is shown in Figure 6.2. Upon photoexcitation, the intersystem conversion from the singlet excited state to the triplet state proceeds through a spin orbital coupling mechanism. The ISC mechanism creates an excited state with the population unevenly distributed amongst three non-degenerate triplet sublevels. The three sublevels are split by a zero field splitting and an electron Zeeman interaction. The magnetic field B mixes the zero-field triplet levels resulting in the T_0, T_- and T_+ electron spin states. These states further split due to hyperfine couplings to nuclear spins. As we shall see in this Chapter, despite the fact that the T_0 state has negligible coupling with the nuclear spins, it can be used as a coupling mediator.

For the characterisation of the triplet state, we perform time resolved (TR-EPR) experiments. Time resolved spectroscopy provides information about the triplet state and its

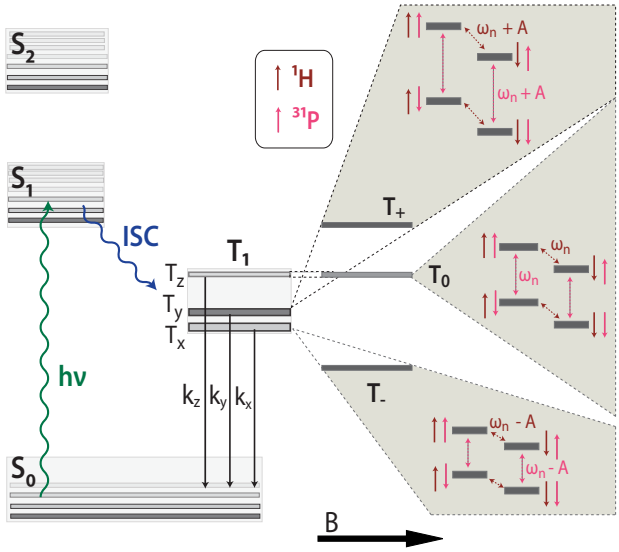


FIGURE 6.2: Upon laser photoexictation the triplet state is populated and the mixing of the zero field levels under the presence of a magnetic field creates three triplet subspaces T_0, T_- and T_+. In DMFPH, these subspaces couple to the two nuclear spins, ^{1}H, ^{31}P causing further splittings due to nuclear Zeeman and hyperfine interactions. The two nuclear spins are marked with red and pink arrows. ω_n is the Larmor frequency of each nuclear spin and A the hyperfine interaction. Although the hyperfine coupling directly distinguishes selective quantum transitions we will see later on that the signal at the $T_-$and T_+ is not sufficient for high-fidelity quantum operations.

dynamics and identifies various interactions, like the mixing between triplet states and its non-phosphorescent nature [FOY97, CMP$^+$95, IFOY96, OYOI94, HOYI95].

The TR-EPR spectra are acquired at set time intervals after the laser pulse and a decay or a buildup of the signal is observed. The time profile of an EPR transient signal, is recorded on CW spectrometers on a digital oscilloscope. In our experimental setup, the decay curves are collected at all resonant magnetic fields in a 2D plot and are recorded on the SpecJet, a transient signal recorder. In Figure 6.3 we show TR-EPR spectra at different delay times after the laser pulse. Initially (for delays 1 - 4μs) the signal decays quickly and then less drastic changes are observed for delays up to 20

The time resolution which is in the order of nanoseconds, corresponds to a relatively large

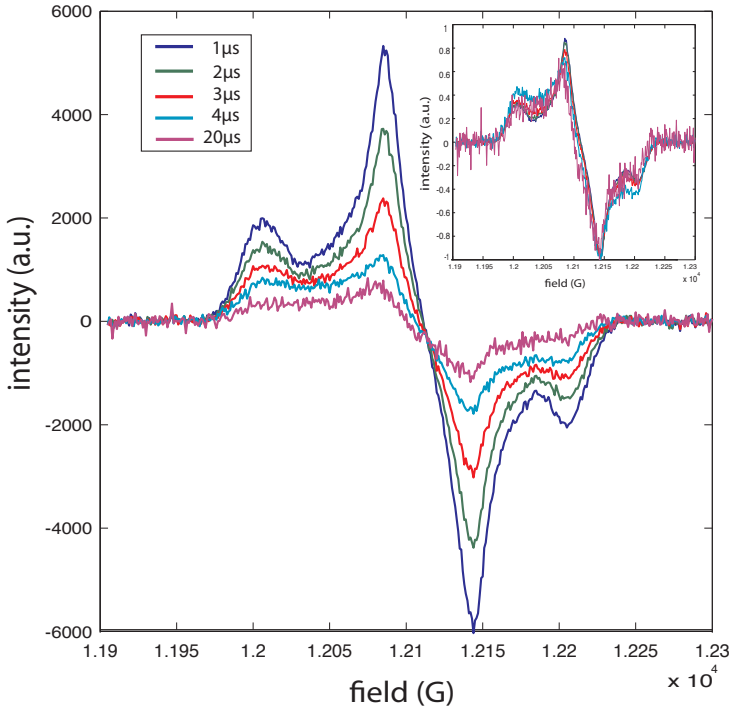


Figure 6.3: Time resolved (TR-EPR) spectra at Q-band 50 K for different delays from the laser pulse. 1μs after the laser pulse the spectra marked with blue reveals two sharp inner maxima and two side peaks of lower amplitude (In TREPR a delay of hundreds of ns is required before the signals builds up characteristic of the time resolution that can be achieved and the the response of the spectrometer) . (inset) After normalising the TR-EPR spectra, it is more pronounced that for longer delays a non uniform decay appears which indicates an orientation-dependence in the triplet relaxation.

bandwidth and low sensitivity. However, in triplet states the low sensitivity is compensated by the high polarisation. The advantage of a time resolved study over pulsed EPR methods is mainly that TR-EPR is free from T_2 artefacts since there is no magnetization decaying in the xy plane. In pulsed EPR experiments, systems with T_2 times shorter than the dead-time cannot be measured (although in DMFPH the T_2 is long enough to use standard pulsed EPR methods). We performed TR-EPR experiments at Q-band and 50K. The experiments have been performed at 680 nm (Fig. 6.1) and 20 Hz repetition rate. The signal was found to be constant in repetition rates of 10 and 20 Hz.

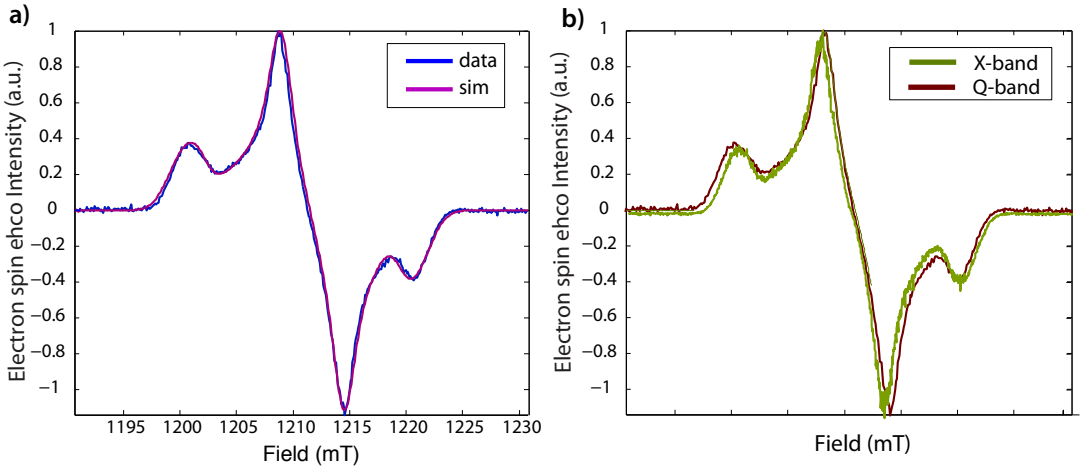


FIGURE 6.4: FS-ESE spectra of DMFPH at 50 K at X-band and Q-band.

The FS-ESE spectrum at X-band looks similar to the TR-EPR spectrum Fig. 6.4, with an absorption-emission pattern and is symmetric in high and low fields. For the simulation of both spectra we used the software Easyspin [SS06]. The fitting is in excellent agreement with the experiment. The g-tensor is $g_{xx} = 2.00076$, $g_{yy} = 2.00224$, $g_{zz} = 2.00274$ with an anisotropy of $g_{zz} - g_{xx} = 0.0019$. Although the g-tensor is slightly anisotropic, the g_{yy} and g_{zz} components could reveal an axial symmetry. To accurately reproduce the experimental spectrum we used a Gaussian g-strain of g_{Sx}= 0.0020, $g_{Sy} = 0.0025$ and $g_{Sz} = 0.0046$. The incorporation of the anisotropic broadening through the Gaussian strain is essential to reproduce the observed lineshape of the outer maxima and is justified by the large g_{Sz} component.

The zero field splitting parameters are $D = -357$ MHz, $E = -57$ MHz and the negative D value is consistent with the negative D value of the fullerene C_{60} . The large E parameter reveals a significant deviation from axial symmetry. The symmetry of the system will be discussed later in more detail, through DFT calculations. We expect that the large E parameter (compared to the E value of DEFM, for example) would give rise to different decay rates of the x and y triplet levels. The inverse of this assumption was made for C_{70}

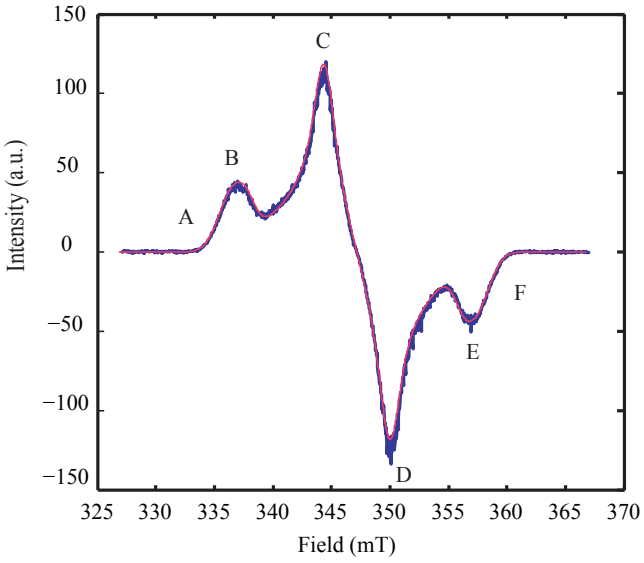


Figure 6.5: FS-ESE spectrum of DMFPH at 50 K, and X-band. Red curve shows the simulation using Easyspin (parameters described in the text).

with regard to its small E value [BDG98]. The population ratio, $|p_x - p_z|/|p_y - p_z| = 0.32$ indicates that the intersystem crossing populates mostly the y sublevel, considering that for a negative D the polarization pattern is $|p_x, p_y| > p_z$.

The FS-ESE spectrum was also acquired in X-band (see Figure 6.6) using selective pulses of 64 ns and 128 ns for the $\pi/2$ and π pulses respectively, but no significant lineshape variations where observed compared to the Q-band FS-ESE. The impact of the g-anisotropy to the FS-ESE spectra is expected to appear at even higher frequencies (> 35 GHz).

FS-ESE experiments (at X-band) were performed for five different delays after the laser flash and we observed significant changes in lineshape. The (normalised) spectra of Figure 6.6 show that for long delays the outer maxima (which correspond to spins with their z axis parallel to the field) decay faster compared to the peaks showing the impact of the T_2 relaxation. This provides evidence of possible field dependence in the relaxation kinetics (at 0.35 T vs 1 T), but to explore this further, identical FS-ESE experiments must be

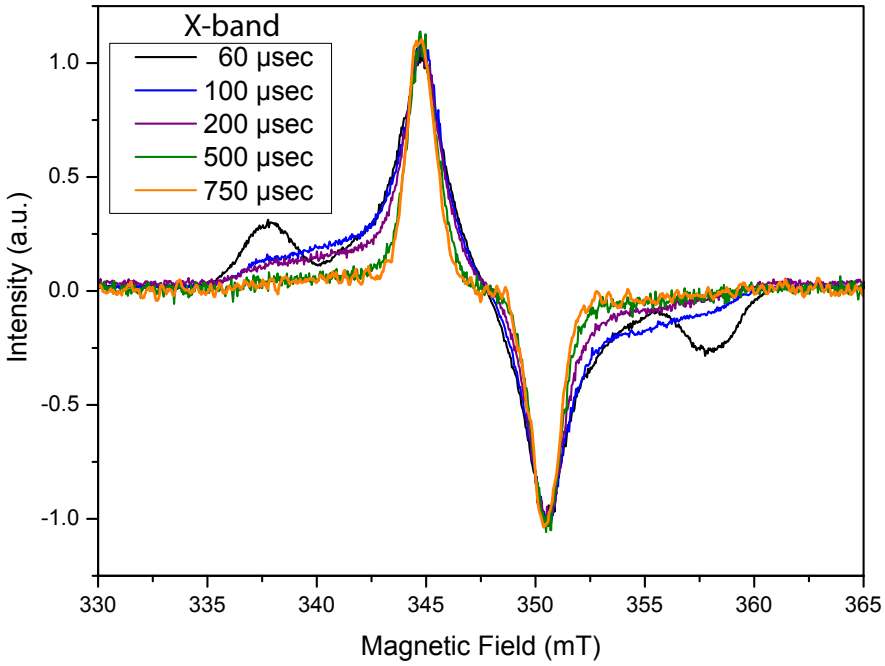


Figure 6.6: Normalized FS-ESE spectra for various delay times after the laser pulse in X-band at 5K. The decay of the side peaks compared to the wings is pronounced as in the 2D TR-EPR spectra. After 750 μs the side have completely disappeared while the peaks are still well resolved.

performed at both Q-band and X-band. The preservation of the symmetric shape of the spectra within this range indicates that no triplet relaxation between the triplet sublevels occur. In the opposite case, any asymmetry that would favour the absorption or emission contributions to the spectra, would indicate that some population is transferred between the levels. The spectra were also recorded at various temperatures from 5–50 K and the lineshape remained the same in the whole temperature range. According to C_{60} studies, any variations of the lineshape with temperature would imply an anisotropic T_2 [BGM95b].

In the FS-ESE spectrum shown in Figure 2.3 with blue and pink we denote the two contributions of the absorption and the emission from the two allowed microwave transitions within the triplet. An interesting point is the existence of two characteristic magnetic fields in which we observe transitions only from emission, $T_+ \rightarrow T_0$ at 345 mT or only from

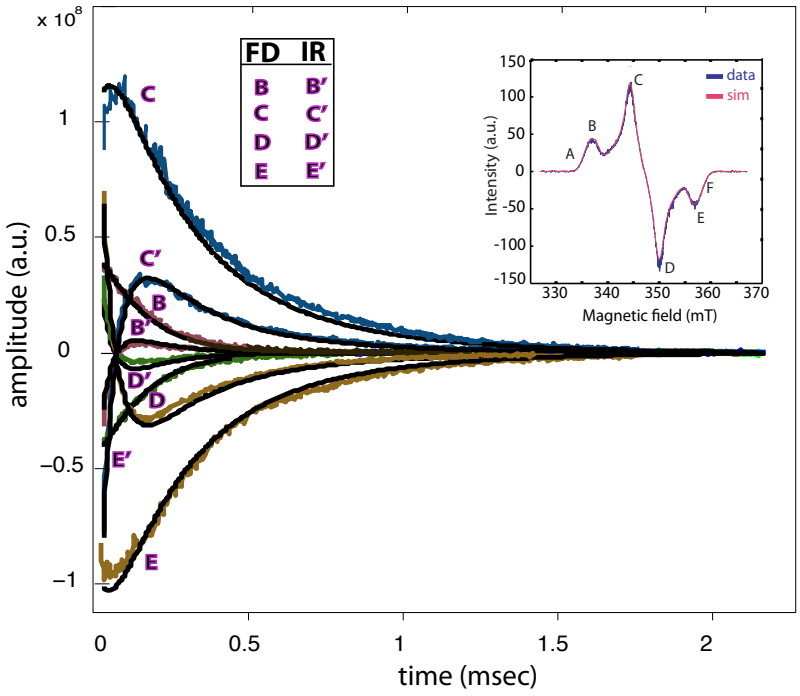


Figure 6.7: Flash-delay (FD) and inversion-recovery (IR) experiments at four magnetic field positions of the FS-ESE spectrum marked B,C,D,E in Figure 6.5. The fittings are in a very good agreement with the experiment and provide the initial populations of the triplet levels and the decay rates to the singlet. The T_y triplet level was most populated and the one that decayed most slowly. In the simulations, no T_1 relaxation between the sub-levels was needed, indicating that the decay of the triplet state occurs in a faster rate compared to the relaxation T_1.

absorption $T_- \rightarrow T_0$ at 348 mT. The ability to concentrate to one the two electronic subspaces will be proven very useful later in our discussion as excitations from both transitions can limit the fidelity of our operations.

6.3 Relaxation Kinetics

Flash-delay and inversion-recovery experiments were performed for the extraction of the decay rates, the lifetime of the triplet state and the populations of the triplet sublevels.

From the simulations we can only deduce that T_1 is longer than any of the observed

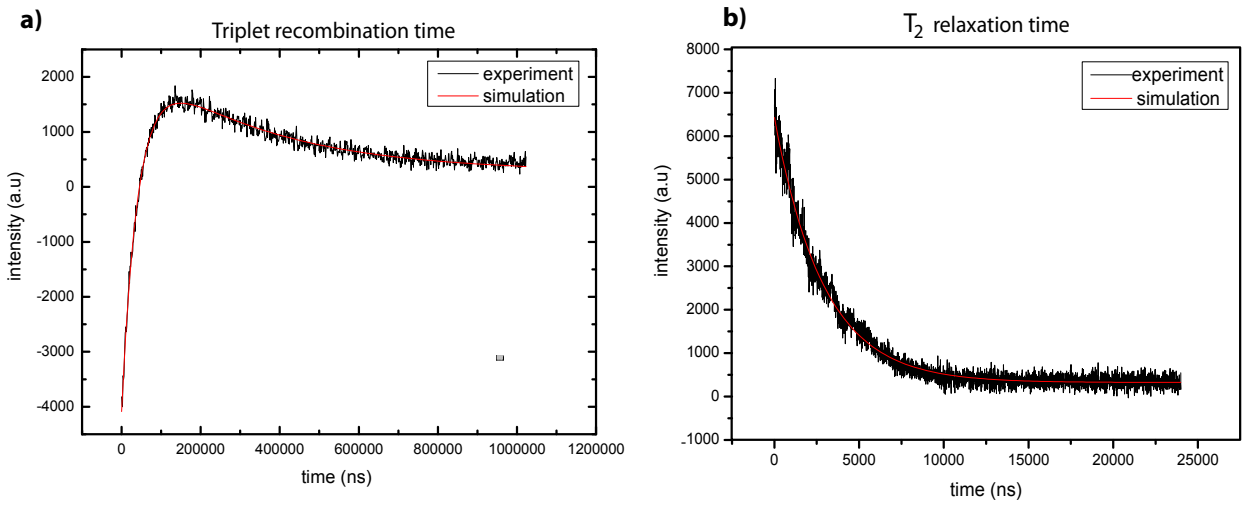


Figure 6.8: a) Fitting of the inversion recovery trace at 350 mT, 5 K to a biexponential gives a slow decay component of 267μs and a fast of 34μs. b) Measurement of T_2 made at the same field and temperature yields a time of about 3 μs.

triplet recombinations times (the longest of which is 267 μs). In contrast, T_2 is much shorter and was measured using a Hahn echo sequence to be $\sim$ 3 μs (shown in Figure 6.8). This was found to be independent of temperature in the range 5 – 50 K. From Figure 6.7 we can see that in a similar way to the DEFM, the ESE intensity rises for the first 100 μs after flash and then decays. The population difference between two triplet sub-levels initially increases due the much faster decay of one of the two levels. It then reaches a maximum and then decays with the decay rate of the more slowly decaying sub-level.

The populations are $p_x = 0.22$, $p_y = 0.71$, $p_z = 0.01$ and the decay rates $k_x = 11000$ s^{-1}, $k_y = 1900$ s^{-1} and $k_z = 28000$ s^{-1}. The lifetime of the triplet state which is an average of the lifetimes of the sublevels is about 200 μs. The populations give a polarisation ratio of 0.33, in good agreement with the polarisation ratio obtained from the ESE-FS. The measured decay rates from the levels T_x and T_y differ by almost an order of magnitude, consistent with the argument we made above regarding the relatively large E.

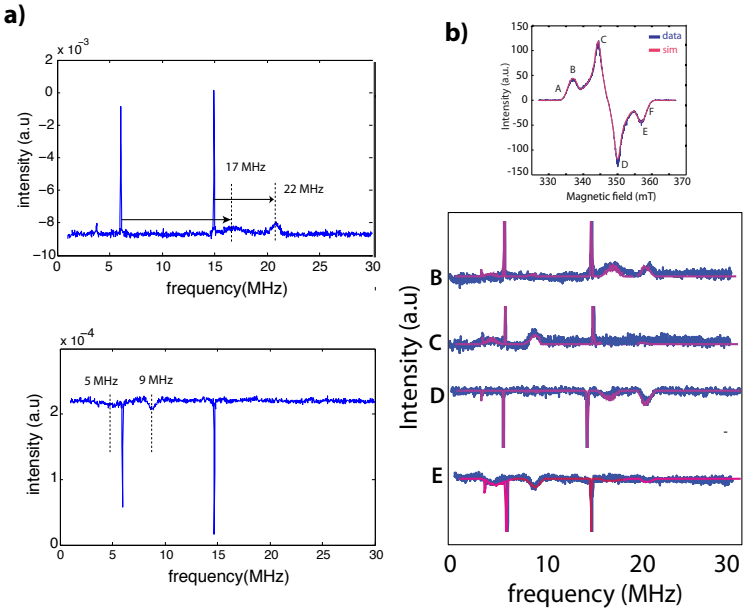


FIGURE 6.9: a) Spectra at 350 mT (field value B) and 344 mT (field value E) . The two most intense peaks the represent the phosphorus and the proton Larmor frequency. The peaks at 5, 9, 17 and 22 MHz arise from the hyperfine interaction of the phosphorus and the proton to the triplet spin. b) Davies ENDOR simulations and experimental data acquired at 5 K at four magnetic fields. The broad, field-dependent ENDOR peaks indicate the hyperfine interaction is anisotropic. From the fitting of the spectra we obtain a hyperfine interaction of 5.9 and 11 MHz for the ^{31}H and ^{1}P, respectively.

6.4 Hyperfine interaction

For the determination of the coupling of the triplet electron to the ^{1}H and ^{31}P nuclear spins we use the Davies ENDOR pulse sequence. We apply soft (selective) microwave pulses of 64 ns and 128 ns duration for the $\pi/2$ and the π pulses respectively and 12 μs RF pulses.

Davies ENDOR spectra at four field positions (B, C, D, E) of the FS-ESE trace are shown in Figure 6.9b. For each EPR transition there are two measurable ENDOR resonance frequencies at

$$\omega_{ENDOR}(0) = \omega_{0,I} \tag{6.1}$$

and, depending on whether the T_+ or T_- level is involved:

$$\omega_{ENDOR}(\pm 1) = \omega_{0,I} \pm A_I. \tag{6.2}$$

where I is the nuclear spin, ω_0 is the Larmor frequency and A_I is the effective hyperfine coupling at a particular magnetic field orientation. From the ENDOR spectra we observe two intense lines at $\omega_{0,P} = 6$ MHz and $\omega_{0,H} = 15$ MHz which correspond to the Larmor frequencies of the ^{31}P and ^{1}H. The weakly resolved peak at 3 MHz is the Larmor frequency of the ^{13}C (arising from nuclear spins in the fullerene cage or in the solvent). In Figure 6.9a we plot separately the two ENDOR spectra at fields B, E, in order to demonstrate the high intensity of the ENDOR peaks which corresponds to an ENDOR efficiency of 90–100%.[1] The integrated amplitude of these transitions demonstrates the quality of state initialisation in the triplet subspace thus the T_0 subspace permits high fidelity nuclear operations.

The magnitude of the hyperfine interaction is directly obtained from the shift of the hyperfine lines compared to Larmor frequencies. In the ENDOR spectra at each magnetic field, we observe two less intense field-dependent peaks (e.g. at 17 MHz and 21 MHz when measured at 350 mT). These represent the hyperfine coupling of the two nuclear spins to the triplet state (Fig. 6.9b). The broad hyperfine peaks indicate an anisotropic hyperfine interaction and the fact that one peak appears to be sharper than the other indicates different degrees of anisotropy. This observation will be also discussed in the DFT section later on in this Chapter. The field dependence is attributed to the subset of spins with different orientations that are excited at a particular field.

The assignment of these two peaks to the nuclear spins can be done through Eq.6.2, which indicates that ENDOR peaks should appear symmetrically around the Larmor frequency. For example, an ENDOR peak appears at about 21 MHz at 350 mT and at about

[1]The efficiency can be calculated by adjusting the baseline of the pulse sequence to coincide with the zero of the digitizer.

9 MHz at 344 mT (shifted in each case by about ±6 MHz from the ^{1}H Larmor frequency at 15 MHz). Similarly, hyperfine peaks arising from the ^{31}P appear at about 17 MHz and 5 MHz, shifted by ±11 MHz from the Larmor frequency of 6 MHz..

After roughly assigning the hyperfine peaks to each of the two nuclear spins, we move on to simulate the ENDOR spectra. Fitting the ENDOR traces in all four different field lines we determine the hyperfine interaction of the ^{1}H and ^{31}P to be A(^{1}H) = 5.9 MHz and A(^{31}P)= 11 MHz. The z axis of the ZFS tensor coincides with the hyperfine tensor so no additional orientations were required for the fitting of the spectra. The extraction of these spectra was a time demanding task as long scans, up to 6 hours, were essential for the resolution of the small hyperfine peaks. This was a limiting factor that didn't allow us to collect more ENDOR spectra at different field lines and extract the whole hyperfine tensor.

We also performed studies on the ENDOR linewidth of the narrow ^{1}H (Larmor frequency) line by varying the length of the RF_H pulse. Starting from a pulse duration of 12 μs we go up to 80 μs and we manage to reduce the linewidth of the free proton line to 10 kHz at Q-band. At X-band according to the inversion recovery spectra we have a maximum window of about 250 μs for the application of an RF pulse. Using pulses up to 230 μs we achieve very narrow linewidths around 4 kHz, but we still limited by the excitation bandwidth of the RF pulse. The broader line at higher magnetic field may arise from small contributions to the Hamiltonian such as the nuclear dipole-dipole interactions (1–100 kHz) and the chemical shift anisotropy (0.1–10 kHz). Such narrow linewidths provide an indication of the long nuclear spin T_2 times (linewidth $\sim 1/T_2$) which are described later on in this Chapter.

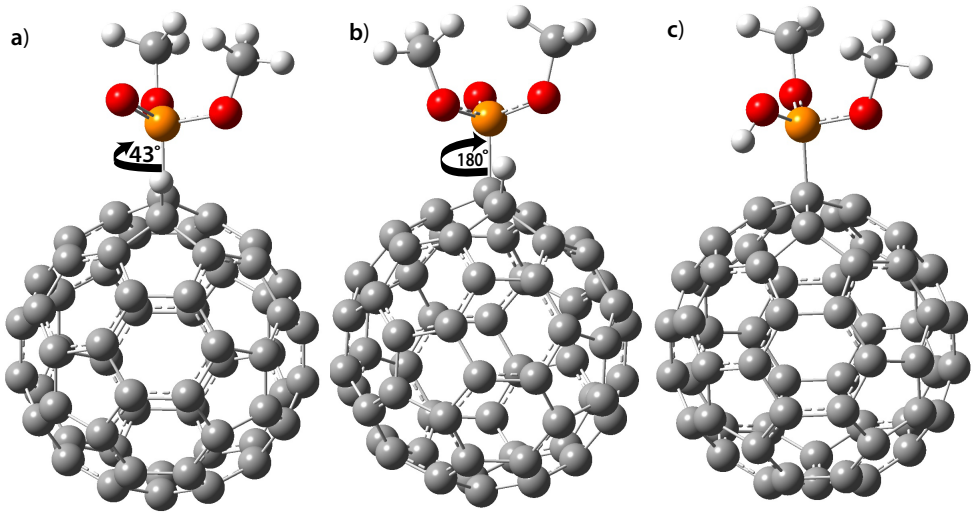


Figure 6.10: Three optimized geometries of the DMFPH. The dihedral angle of the doubly bonded oxygen is (a) 43° and (b) 180°. The structure b) has a C2v symmetry but higher energy compared to (a). The conformation (c) is a radical where the single proton that was attached on the cage is now bonded to the oxygen. This geometry has the highest energy of both and an energy difference of 0.5eV from best optimised geometry (a). Images were rendered using Gaussview.

6.5 DFT

We performed AE DFT calculations for the determination of the g-tensor and the hyperfine interaction of the two nuclear spins, $A(^1\mathrm{H})$ and $A(^{31}\mathrm{P})$ with the triplet state. We used an unrestricted Kohn Sham calculation as implemented by the program package ORCA, a tool for quantum chemistry, which is based on Gaussian type orbitals [Nee07]. We optimised the DMFPH geometry in the singlet and triplet states using def2-SVP basis . We started from several different conformations which mainly concern the relative position of the phosphonate adduct with regard to the nuclear spin ^{1}H. Preliminary calculations showed that the position of methyl groups on the phosphonate adduct doesn't affect significantly the calculated parameters.

In the starting geometries we varied systematically the dihedral angle of the doubly bonded oxygen with respect to the proton on the fullerene cage from 0° to 180° in steps of

30°, where 0° corresponds to the oxygen facing the proton. We also explored the possibility of an attached proton to the phosphonate adduct as this conformation can be formed under specific conditions. These geometries have been further optimised with larger basis def2-TZVP sets [WA05] and the final geometries are shown in Figure 6.10. The radical had the highest energy compared to the other conformations (Fig. 6.10c). Interestingly, the six initial geometries converged to two geometries with dihedral angles 42-45° and 170-180°. The conformation with a digedral angle of 43° has the lowest energy and differs energetically from the 180° by 0.3eV (Fig. 6.10 a,b). The length of the P-C bond was found 1.87Å .

For the best optimised geometry (Fig. 6.10a) in the triplet state, we calculated the g-tensor and the hyperfine interaction using the IGLOIII basis which improves the description of the core orbitals (EPR II basis for P is not available in ORCA).

The value of the$g$-tensor is

$$\mathbf{g_{theory}} = \begin{pmatrix} 1.999 & 0 & 0 \\ 0 & 2.0018 & 0 \\ 0 & 0 & 2.0027 \end{pmatrix} \tag{6.3}$$

and the anisotropy g-aniso is 0.0018. The result is in a very good agreement with the experiment ($g_{xx} = 2.00076$, $g_{yy} = 2.00224$, $g_{zz} = 2.00274$), and also predicts correctly that the g_{zz} is the largest component. The theoretical results don't reveal any axial symmetry since g_{yy} is much smaller than g_{zz}. This is also verified by the non symmetric geometry which is consistent with the large E value. A simulation of an EPR spectra using the calculated g-tensor, produces a very good fitting since the g_{zz} component which is responsible for the shape of the spectra agrees in theory and experiment. The difference between the g_{xx} components introduces a shift of the spectra on the x axis by 0.4 mT. Despite the fact that the field was correctly calibrated, even small differences can account for this shift so this deviation may be within the experimental error.

For a visual representation the strength of the hyperfine interaction over the whole

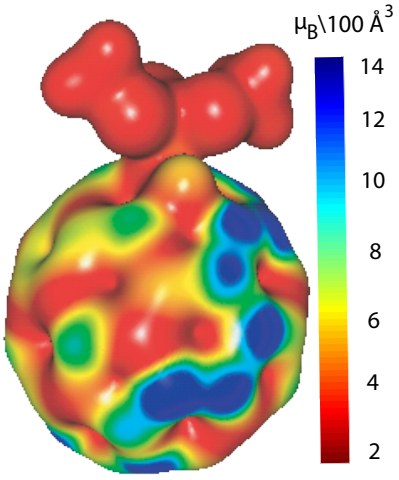


Figure 6.11: Spin density in the lowest triplet excited state of the DFMPH fullerene. The chosen charge isosurface has an isovalue of 0.07 electron/Å ^{3} and the overlaid color indicates the magnitude of the spin density. The spin density is mostly gathered around the fullerene cage. Images rendered using GABEDIT [Alo].

molecule, we calculate the spin density distribution. We observe that the spin density is localized around the fullerene cage while negligible density appears on the adducts (Figure 6.11). The calculations of the isotropic hyperfine interaction gave $A_{iso,H} = 7.6$ MHz [2] and $A_{iso,P} = 13.5$ MHz. The hyperfine tensors for the ^{1}H and the ^{31}P are

$$\mathbf{A_H} = \begin{pmatrix} 7.0 & 0 & 0 \\ 0 & 7.3 & 0 \\ 0 & 0 & 8.6 \end{pmatrix} \tag{6.4}$$

$$\mathbf{A_P} = \begin{pmatrix} 12.3 & 0 & 0 \\ 0 & 12.4 & 0 \\ 0 & 0 & 16 \end{pmatrix}. \tag{6.5}$$

The isotropic interaction is in good agreement with the experimental values of the isotropic hyperfine interaction, $A_{exp,H} = 6$ MHz and $A_{exp,P} = 11$ MHz. The hyperfine

[2] The $A_{iso,x}$ values are given by the trace Tr $(A_x)/3$, where x = H,P

tensor of the ^{1}H is less anisotropic compared to the ^{31}P an observation that is consistent with the slightly sharper peak of the ^{1}H. The small deviation of $\sim$2 MHz could be improved with larger basis sets for the optimisation of the structures since the hyperfine interaction is quite sensitive to variations of the bond lengths as it was demonstrated in Chapter 5. The discrepancies may also originate from the use of GTOs instead of STOs. These calculations show that the hyperfine interaction is axially symmetric for both the ^{1}H and the ^{31}P.

In general, an insight into the origin of the type of anisotropy of the g and A tensors can be provided through a detailed study of the orbitals which carry large spin densities and their association to particular atoms. An example of this type of study on the Sc@$C_8$2 fullerene revealed that although the system has an axially symmetric hyperfine interaction the g-tensor is anisotropic [MHL$^+$05].

Additional calculations using plane wave methodology and norm conserving pseudopotentials have been performed but despite the fact that the hyperfine interaction of the ^{1}H was found 6.5 MHz, the hyperfine interaction of the ^{31}P was found to be about twice the experimentally observed value. These values depend a significantly on the P-C distance. Structure optimisation reveals that the P-C bond is broken or weakened by the triplet. For weak bonds DFT is not very accurate and this can be the reason for the discrepancy with experiments.

6.6 Relaxation Studies

For the determination of the time evolution of a nuclear coherence of the ^{1}H and ^{31}P spins we perform T_{2n} experiments.

The pulse sequence for a T_{2H} experiment is shown in Figure 6.12 and is marked by the shaded area.

Initially the electron polarization is transfered to the nuclear subspace by the application

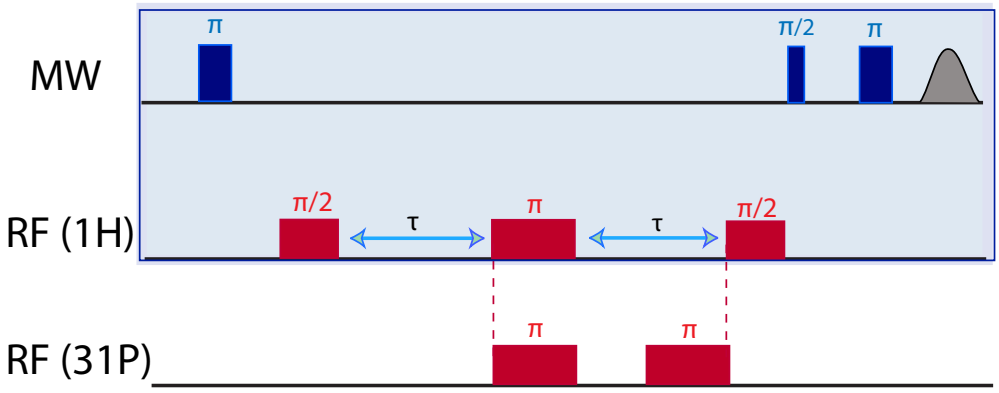


Figure 6.12: (shaded area) Measurement of $T_{2\mathrm{H}}$. We monitor the decay of the echo created by the first two RF pulses by varying the time τ. The second RF^{π}_{H} which is applied on the nuclear echo transfers the coherence to electron polarization. The total pulse sequence shown in the figure corresponds to a SEDOR experiment. After the generation of the nuclear coherence the application of an RF^{π}_{P} pulse simultaneously with an RF^{π}_{H} pulse avoids refocusing the dipolar coupling allowing it to be observed. The time required for the dipolar coupling to perform a π pulse is 170 μs.

of a microwave π pulse. The radiofrequency $\pi/2$ pulse generates a nuclear coherence and its decay is monitored as a function of the time τ. The application of the second $\pi/2$ at the position of the nuclear echo transfers the nuclear coherence back to electron polarization.

For the extraction of the relaxation times we perform preliminary measurements where we define the upper and lower bounds which correspond to the absence and presence of population on the electronic triplet level. The absence of population occurs through population transfer from the electronic level to the nuclear subspace through the application of an RF π pulse. Using the middle point of these high and low values, which correspond to a completely dephased coherence, to be the baseline for each nuclear spin, we fit the T_{2N} traces. This procedure is applied to each individual nuclear spin and the relaxation times for the ^{1}H was 0.54 ms and for the ^{31}P was 1.2 ms at 5 K.

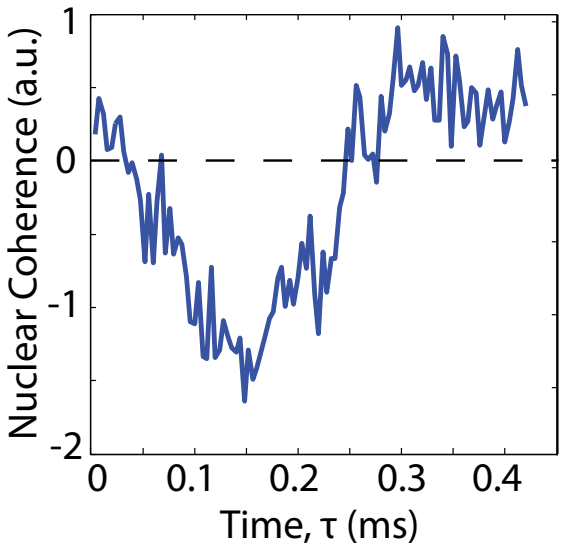


FIGURE 6.13: The SEDOR sequence produces an oscillation in the nuclear coherence as τ is swept, corresponding to a dipole coupling of 3 kHz.

6.7 SEDOR

Spin Echo Double Resonance or SEDOR is an NMR technique developed to determine small nuclear-nuclear dipolar couplings [EHK60]. In EPR, the principle of an NMR SEDOR experiment is combined with electron manipulation for initialization and readout. The SEDOR pulse sequence is shown in Figure 6.12. Similarly to a T_{2n} experiment the selective microwave π pulse transfers the polarisation to the nuclear subspace and the $RF_H^{\pi/2}$ pulse creates a nuclear coherence. The nuclear coherence evolves for some time and then a refocusing RF_H^{π} pulse is applied simultaneously with an RF_P^{π} pulse.The ^{1}H spin evolves under the influence of the ^{31}P spin and their mutual interaction is the direct nuclear coupling. By applying refocussing π pulses simultaneously to both spins, the nuclear coupling is not refocussed, and the ^{1}H spin picks up some net phase over the course of the sequence. The second RF_P^{π} pulse is applied in order to reverse the polarisation transfer achieved by the first RF_P pulse. The last $RF_H^{\pi/2}$ pulse is used to rotate the nuclear coherence along $\pm z$ depending on the state of the second nuclear spin. Specifically, if the second nuclear

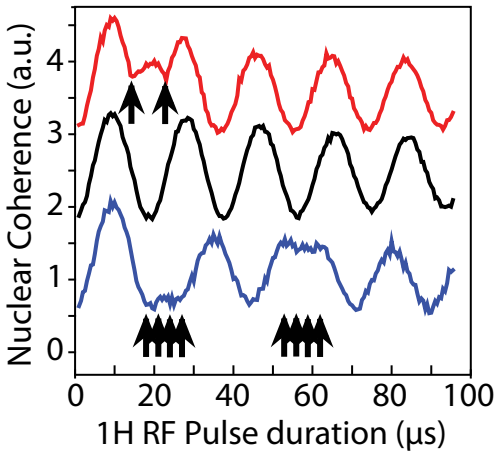


Figure 6.14: Rabis oscillations for the demonstration of an ultrafast ^1H phase gate. The black trace represents the typical uninterrupted Rabis oscillations. Application of a 2π phase gate (arrows) on resonance with an electronic transitions while driving the evolution of the state on the Bloch sphere with an RF pulse, allows for the generation and retention of an arbitrary phase.

spin is up, the first nuclear spin will evolve positively and the last $\pi/2$ pulse will return the magnetization onto $+z$. The opposite happens if the second nuclear spin points down. The above sequence produces an oscillation in the nuclear coherence shown in Figure 6.13. The observed oscillation corresponds to a nuclear coupling of about 3 kHz.

In quantum information, the SEDOR pulse sequence is equivalent to a CNOT operation.When the qubits are in the $|00\rangle$ state or the $|01\rangle$ state the second qubit depending if its up or down will flip the state of the first qubit ($|00\rangle \xrightarrow{CNOT} |00\rangle$ and $|01\rangle \xrightarrow{CNOT} |11\rangle$). The gate time of the CNOT corresponds to the minimum in the SEDOR experiment: about $170\mu s$.

The ground state indirect J-coupling was measured through NMR experiments and was found 30 Hz one hundred times smaller than the coupling in the photoexcited state. The coupling time in this case is 17ms. The enhancement of the coupling upon photoexcitation and its relatively small coupling time allows for CNOT operations within the lifetime of the electron.

6.8 Phase gates

In Chapter 1 we discussed an implementation of phase gates similar to the Aharonov-Anandan phase gate achieved by driving an electron spin around a 2π rotation. In Figure 6.14 we demonstrate such ultrafast phase gates (C-PHASE) on the ^{1}H nuclear spin, through manipulation of the triplet electron spin and its use for the demonstration of bang-bang decoupling. The most crucial point in this operation is that no population is transferred between the states and only a phase variation in introduced.

Initially a preparation pulse π is applied to transfer the thermal polarization of the electron spin to the nuclear subspace. Nuclear Rabi oscillations on the ^{1}H (black trace) were obtained as a reference. The decoupling is achieved by applying microwave 2π pulses (256 ns duration) every 2 μs (Fig 6.14 black arrows). While the decoupling microwave pulses are being applied, the nuclear spin is trapped at a particular state, and continues to evolve only after they have ceased. Since these phase gates are implemented using the electron spin, they are much faster than what could be achieved using direct nuclear excitation. The C-Phase gate used here is approximately 10^5 times compared to NMR analogues.

6.9 Summary of characterisation

In this chapter we performed EPR and ENDOR experiments to describe the triplet state of the phosphine oxide fullerene (DMFPH) and identify the relevant conditions under which quantum operations of high fidelity can be applied and specifically operations related to the demonstration of entanglement through quantum tomogrpaphy.

Decay kinetics on the triplet state revealed that the signal of the EPR persists for times up to 500 μs. Since this characterises the available time to perform quantum operations we need to ensure that the pulse sequences do not exceed this limit. This can be achieved by

keeping fixed the length of the experiments between the initial optical pulse and readout.

Another point is that the triplet levels T_0, T_+ and T_-, are distinguished by the different nuclear spin couplings. Thus, applying microwave pulses act selectively on one nuclear spin sub-space is possible. The weak intensity of the hyperfine-coupled ENDOR peaks result in low fidelity nuclear spin operations within the T_+ and T_- subspaces. Therefore, for high-fidelity control operations we consider nuclear spins transitions within the T_0 triplet subspace in which we can obtain high ENDOR efficiency.

The coupling observed between the two nuclear spins upon photoexcitation indicates that the implementation of a CNOT operation, which is the first ingredient towards the generation of entanglement, is possible within the lifetime of the triplet state. Because the electron spin T_2 time is shorter than an RF π pulse, nuclear coherences cannot be mapped into a microwave coherence for observation. Instead the nuclear coherences are projected onto a population difference by the application of a second CNOT gate.

In the introduction we mentioned that an alternative type of CNOT can be implemented by the application of two Hadamard gates and a C-PHASE gate. After demonstrating the feasibility of a C-PHASE gate, we will discuss how this phase gate can be of great use towards the demonstration of entanglement.

6.10 Quantum State Tomography

A combination of all the above lifetimes, ENDOR efficiencies and hyperfine couplings provides a solid ground for high-fidelity quantum operations. For the generation and the readout of a nuclear spin (pseudo-)entangled Bell state, we use the pulse sequence shown in Figure 6.15. The details on the implementation of these pulse sequences and the quantum tomography schemes are described in the dissertation of Stephanie Simmons (2011).

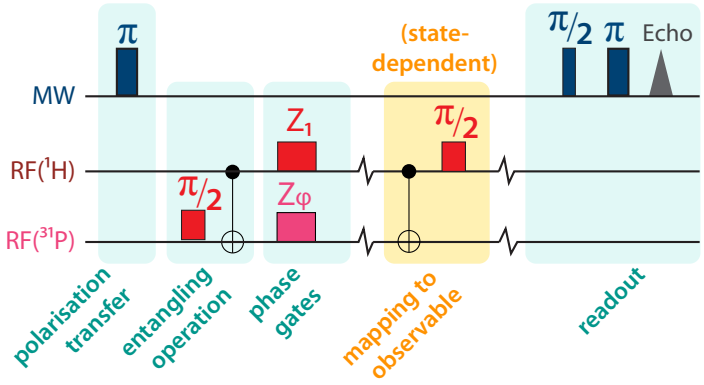


Figure 6.15: Pulse sequence for the extraction of the element of the density matrix. The CNOT representations correspond to entangling gates using a)SEDOR and b)C-PHASE operations. The read out is changed according to the measured density matrix element.

For the extraction of the elements of the density matrix of this two nuclear spin (four-level) system through quantum state tomography we apply the method that was presented recently and demonstrated entanglement in Si:P though geometric Z rotations [SBR+11] (the basic concept of this method was presented in Chapter 1).

Quantum tomography using the direct nuclear coupling to implement the CNOT, gave a density matrix fidelity with respect to an ideal Bell state of 56 % (taking into account the measured T_{2n} times). The low fidelity is attributed to the long entangling gate times which are associated with the weak nuclear coupling and long CNOT duration. The application of two CNOT operations of 170 μs approaches the 500 μs limit, in which a large fraction of the triplet signal has almost decayed.

In order to minimize the entangling gate time we turn to a different approach which incorporates the use of phase gates. The implementation of a CNOT gate through C-PHASE operations reduces the coupling time down to 440 ns. This time is the length of the 2π pulse which imparts a phase onto the two states involved in the operation. This coupling time is five orders of magnitude faster compared to the coupling time in the ground state. In combination with the two Hadamard gates, the total CNOT time is 24.6 μs. The

fidelity of this alternative CNOT is 69% and is much higher than the fidelity obtained by using a CNOT based on the direct nuclear coupling. The improvement of the fidelity underlines the impact of the reduction of the coupling time.

6.11 Conclusions

In this Chapter we presented a method for generating entanglement of nuclear spins using triplet photoexcited states. The characterization of the system provides the ground to understand the system and identify these requirements which could allow for the application of quantum tomography schemes. By using three different methods: coupling through NMR (ground state),dipolar coupling through SEDOR and coupling through C-PHASE gates (photoexcited state), we manage to reduce the coupling time to hundreds of nanoseconds which is five orders of magnitude compared to the ground state. The reduction of the coupling time reflects upon the fidelity of our operations. A further improvement of the fidelity can be achieved by using instead of frozen solutions, single crystals with specific orientation selection. This work motivates studies on controlled de-excitation of the triplet state and nuclear quantum operations not relying on the triplet state in order to remove the electron as a source of nuclear decoherence strength.

7

Conclusions

Entanglement plays a key role in quantum computation and quantum communication. A number of studies have demonstrated entangling operations in systems like NV centers, endohedral fullerenes, malonic acid crystals, quantum dots, photons and donor spins in silicon. In this thesis we considered electron and nuclear spins as representations of qubits. The difficultly of manipulating spin couplings directly led to schemes which propose coupling control through photo-excited mediators. Mediated coupling has been discussed in defects in semiconductors, quantum dots, superconducting qubits, electron spins and many more.

Here, we go a step further and we demonstrate how nuclear-nuclear entangling gates can be generated via a triplet photo-excited mediator. We explored two different cases: homonuclear fullerene systems with equal hyperfine couplings to the control electron spin (symmetric case) and a heteronuclear fullerene system with unequal coupling strengths (asymmetric case). The control system in both cases was the delocalized electron spin over the fullerene cage generated upon photo-excitation.

In Chapter 4 we presented a theoretical scheme for symmetric systems, which identifies the hyperfine interaction as the key parameter for the generation of entanglement. We tested the feasibility of this proposal by performing experiments on a candidate system, the diethyl fullerene malonate (DEFM), a molecule with one nuclear spin. We conducted EPR experiments to fully characterise the system and determined the hyperfine interaction through ENDOR methodology and density functional theory. We were able to extract the terms of the Hamiltonian, the decay kinetics of the triplet and the populations on each sub-level. According to the proposal, the maximum entanglement of formation can be achieved in highly polarised systems. However, our experimental results show that there is partial polarization as the population of the triplet state is equally distributed between two out of the three triplet levels. This requires the application of the protocol twice. Given a two nuclear spin system that exhibits a hyperfine coupling similar to that observed in our test molecule (3 MHz), entanglement of formation of 0.5 can be generated. In the ideal case of a hyperpolarised triplet state the hyperfine interaction of 3 MHz would lead to entanglement of formation higher than 0.8. For a maximum entanglement hyperfine couplings between 5–12 MHz are required.

Since the hyperfine coupling is a tunable parameter which depends on the functional groups, in Chapter 5 we explored a set of regioisomeric fullerene derivatives to investigate the impact of the position of the adduct to the hyperfine interaction and identify a structure that best meets the requirements for the feasibility of the above proposal. We studied

three regioisomeric DEFM derivatives with two nuclear ^{13}C as well as the DEFM molecule, for completeness, using the generalized gradient approximation (GGA) to DFT. For the extraction of the hyperfine interaction we used GIPAW methods including core polarization correction. We optimized the structures in singlet and triplet configurations and for the best optimised geometry in the triplet state we calculated the hyperfine tensors. Our results showed that out of the three fullerene derivatives the B3 (*trans* - 3) molecule exhibits the largest hyperfine interaction, equal hyperfine strengths which are essential for the feasibility of the above proposal and also can be produced with high yield. This work motivates DFT studies of homonuclear systems, with two or more nuclear spins coupled equally to the photo-excited mediator. In Chapter 6 we studied a heteronuclear system, the phosphine oxide fullerene C_{60} (DMFPH) and we identified the requirements that permit high fidelity entangling operations. We performed EPR experiments and all electron DFT calculations to characterise the structure and gain understanding of the interactions. The calculation of the g-tensor and the hyperfine interaction through DFT was in very good agreement with the experimental results. By conducting relaxation kinetic studies we determined the maximum available time to perform quantum operations before the triplet state decays away. The 90-100% ENDOR efficiency of the Larmor frequencies indicates that for high fidelity nuclear operations we must consider nuclear spin transitions within the T_0 subspace. SEDOR experiments for the determination of the nuclear-nuclear J-coupling revealed that photo-excitation enhances the coupling from 30Hz (ground state through NMR) to 3kHz. This enhancement allows for CNOT operations within the lifetime of the triplet state. For the extraction of the final state we perform quantum state tomography. Since we are T_2 limited though, we are forced to perform projective measurements by mapping the nuclear coherence onto populations. We demonstrated entangling gates using the enhanced J-coupling and C-PHASE gates. CNOT gates using J-coupling were of limited fidelity (56%) due to the long entangling times associated with the weak J-coupling and the long

CNOT duration of 170μs. Exploitation of an ultrafast CPHASE gate allows for quantum operations of higher fidelity as the use of the electron spin accelerates the generation of entanglement. In this case the coupling time was only 440 ns, five orders of magnitude faster compared to the coupling time in the ground state and the fidelity was 70%. Further studies in this direction that could demonstrate quantum gates of even higher fidelity and finally lead us to true entanglement require crystals with better orientation selection rather than disordered frozen solutions. Another thought would be the use different methods to systematically transfer and build up polarization on the nuclear spin for better initialization. Additionally, this work motivates the further study of controlled de-excitation of the triplet state, rather than relying on the random decay process which can cause the decoherence of the entangled state. This can be achieved by the application of a second laser pulse of different wavelength which excites the system to higher excited state with shorter lifetime. Studies on the nuclear-nuclear spin entanglement can be defined through NMR

Once in the singlet ground state, NMR tomographyof the nuclei could be used to test for the presence of ground state nuclear entanglement. Beneficial would also be other electron-mediated ultrafast nuclear quantum operations that do no depend on J-coupling strengths.

References

[AB03] D. V. Averin and C. Bruder. *Phys. Rev. Lett.*, 91, 057003, (2003).

[ACP96] G. Agostini, C. Corvaja, and L. Pasimeni. *Chem. Phys.*, 202, 349, (1996).

[AG78] A. Abragam and M. Goldman. *Rep. Prog. Phys*, 41, 395, (1978).

[Alo] A. Alouche. http://gabedit.sourceforce.net/.

[AvSW+94] A. Angerhofer, J. U. von Schutz, D. Widmann, W. H. Muller, H. U. ter Meer, and J. Sixl. *Chem. Phys. Lett.*, 217, 403, (1994).

[Bar96a] A. Barenco. *Contemp. Phys.*, 37,375, (1996).

[Bar96b] V. Barone. Recent advances in density functional methods. (1996).

[BDG98] M. V. Bronsvield, X. R. L. Dauw, and E. J. J. Groenen. *Chem. Phys. Letters*, 293, 528, (1998).

[Ben82] P. Benioff. *Physical Review Letters*, 48, 23,1581, (1982).

[BFTM06] M. Bortolus, A. Ferrarini, J. Van Tol, and A. Maniero. *The Journal of Physical Chemistry B*, 110, 3220, (2006).

[BG09] M. Brustolon and E. Giamello. *Electron Paramagnetic Resonance, Wiley and Sons, New Jersey.* (2009).

[BGM+92] M. Bennati, A. Grupp, M. Mehring, K.-P Dinse, and J. Fink. *Chem. Phys. Lett.*, 200, 440, (1992).

[BGM95a] M. Bennati, A. Grupp, and M. Mehring. *Chem. Phys. Lett.*, 102, 9457, (1995).

[BGM95b] M. Bennati, A. Grupp, and M. Mehring. *J. Chem. Phys.*, 102, 22, (1995).

[BHP+98] G. J. B. Van Den Berg, D. J. Van Den Heuvel, O. G. Poluektov, I. Holleman, G. Meijer, and E. J. J. Groenen. *Journal of Magnetic Resonance*, 131, 39, (1998).

[Blö94] P. E. Blöchl. *Phys. Rev. B*, 50, 17953, (1994).

[Boy50] S.F. Boys. *Proc R. Soc*, 525, A 200, (1950).

[BPTM04] M. Bortolus, M. Prato, J. Van Tol, and A. L. Maniero. *Chem. Phys. Lett.*, 398, 228, (2004).

[BSK07] M. S. Barhamy, M. H. F. Sluiter, and Y. Kawazoe. *Phys. Rev. B*, 76, 035124, (2007).

[CA80] D. M. Ceperley and B. J. Alder. *Phys. Rev. Lett.*, 45, 566, (1980).

[CDF+03] T. Calarco, A. Datta, P. Fedichev, E. Pazy, and P. Zoller. *PHYSICAL REVIEW A*, 68, 012310, (2003).

[CFH96] D. G. Cory, A. F. Fahmy, and T. F. Havel. *PhysComp 96 (T. Toffoli, M. Biafore and J. Leao, Eds.), pp. 8791, New England Complex Systems Institute*, (1996).

[CH70] M. L. Cohen and V. Heine. *Solid State Physics*, 24, 37, (1970).

[CH97] X. Camps and A. Hirsch. *J. Chem. Soc., Perkin Trans. 1595*, 1997.

[Chi92] D. M. Chipman. *Theor. Chim. Acta.*, 82, 93, (1992).

[CHMW62] G. W. Chantry, A. Horsfield, J. R. Morton, and D. H. Whiffen. *Mol. Phys.*, 5, 589, (1962).

[CMP+95] C. Corvaja, M. Maggini, M. Prato, G. Scorrano, and M.J. Venzin. *J. Am. Chem. Soc.*, 117, 8857, (1995).

[CO97] C. C. Chancey and M. C. M. O'Brien. *The Jahn Teller effect in C_{60} and other Icosahedral Complexes*, Princeton University Press, New Jersey, (1997).

[CY95] I. L. Chuang and Y. Yamamoto. *Phys. Rev. A*, 52, 3489, (1995).

[CZ02] Z-B. Chen and Y-D. Zhang. *Phys. Rev. A*, 65(4B), 441021, (2002).

[Dau02] X. L. R. Dauw. *Dissertation : Excited states of C_{60} and C_{70}*, (2002).

[Dav74] E.R. Davies. *Phys. Lett. A*, 47, 1, (1974).

[DBD+80] M. Deimling, H. Brunner, K. P. Dinse, K. H. Hausser, and J. P. Colpa. *J. Magn. Reson*, 39 185, (1980).

[Deu85] D. Deutsch. *Phil. Trans. R. Soc.*, 400:97,, (1985).

[Deu89] D. Deutsch. *Proc. Roy. Soc. Lond. A*, 425, 7390, (1989).

[DMM07] M. D'Avezac, N. Marzari, and F. Mauri. *Phys. Rev. B*, 76, 165122, (2007).

[DPW+98] X. L. R. Dauw, O. G. Poluektov, J. B. M. Warntjes, M. V. Bronsveld, , and E. J. J. Groenen. *J. Phys. Chem. A*, 102, 3082, (1998).

[DvdBvdH+00] X. L. R. Dauw, G. J. B. van den Berg, D. J. van den Heuvel, O. G. Poluectov, and E. J. J. Groenen. *J. Chem. Phys.*, 112, 16, 7202, (2000).

[DWLY00] F. Yamaguchi D. W. Leung, I. L. Chuang and Y. Yamamoto. *Phys. Rev. A*, 61, 042310, (2000).

[EHK60] M. Emshwiller, E. L. Hahn, and D. Kaplan. *Physical Review*, 2, 118, (1960).

[Fes67] R. W. Fessenden. *J. Phys. Chem.*, 71, 74, (1967).

[Fey82] R. P. Feynman. *Int. J. Theor. Phys.*, 21, 467,, (1982).

[FOY97] J. Fujisawa, Y. Ohba, and S. Yamauchi. *J. Phys. Chem. A*, 101, 434, (1997).

[FS63] R. W. Fessenden and R. H. Schuler. *J. Chem. Phys.*, 39, 2147, (1963).

[FS99] M. Fuchs and M. Scheffler. *Comput. Phys. Comm.*, 119, 67, (1999).

[FTHBS+09] M. J. Frisch, G. W. Trucks, G. E. Scuseria H. B. Schlegel, M. A. Robb, J. R. Cheeseman, G. Scalmani, B. Mennucci V. Barone, G. A. Petersson, H. Nakatsuji, M. Caricato, H. P. Hratchian X. Li, A. F. Izmaylov, J. Bloino, G. Zheng, M. Hada J. L. Sonnenberg, M. Ehara, K. Toyota, R. Fukuda, J. Hasegawa, T. Nakajima M. Ishida, Y. Honda, O. Kitao andH. Nakai andT. Vreven, J. E. Peralta J. A. Montgomery, Jr., F. Ogliaro, M. Bearpark, J. J. Heyd, and V. N. Staroverov andR. Kobayashi andJ. Normand E. Brothers, K. N. Kudin, J. C. Burant S. S. Iyengar J. Tomasi M. Cossi N. Rega J. M. Millam andM. Klene andJ. E. Knox J. B. Cross

V. Bakken C. Adamo J. Jaramillo and R. Gomperts R. E. Stratmann O. Yazyev A. J. Austin R. Cammi K. Raghavachari, A. Rendell, R. L. Martin K. Morokuma V. G. Zakrzewski C. Pomelli, and J. W. Ochterski, and J. J. Dannenberg G. A. Voth, P. Salvador, Farkas J. B. Foresman J. V. Ortiz J. Cioslowski S. Dapprich, A. D. Daniels, and D. J. Fox. *Gaussian 09, Revision A.1, Gaussian, Inc., Wallingford CT.* (2009).

[FW60] A. J. Freeman and R. E. Watson. *Phys. Rev Let.*, 5, 489, (1960).

[GAK69] S. P. Glynn, T. Azumi, and M. Kinoshita. Molecular spectroscopy of the triplet state. *Prentice Hall Inc, New Jersey*, (1969).

[GBB+09] P. Giannozzi, S. Baroni, N. Bonini, M. Calandra, D. Ceresoli R. Car, andC. Cavazzoni, G.L. Chiarotti, M. Cococcioni, S. Fabris I. Dabo, andA. Dal Corso, G. Fratesi, andR. Gebauer S. de Gironcoli, C. Gougoussis U. Gerstmann, A. Kokalj, M. Lazzeri, L. Martin-Samos, R. Mazzarello N. Marzari, F. Mauri, S. Paolini, A. Pasquarello, S. Scandolo G. Sclauzero A. P. Seitsonen A. Smogunov P. Umari L. Paulatto, C. Sbraccia, and R. M. Wentzcovitch. *J. Phys. Condens. Matter*, 21, 395502, http://www.quantum-espresso.org, (2009).

[GL76] O. Gunnarsson and B. I. Lundqvist. *Phys. Rev. B*, 13, 4274, (1976).

[GMC99] T. Gregor, F. Mauri, and R. Car. *J. Chem. Phys.*, 111, 1815, (1999).

[GPM+92] E.J. J. Groenen, O. G. Poluektov, M. Matsushita, J. Schmidt, and Meijer Van der Waals. *Chem. Phys. Lett.*, 197, 314, (1992).

[GRMS09] U. Gerstmann, M. Rohrmuller, F. Mauri, and W. G. Schmidt. *Physica Status Solidi*, 7, 157, (2009).

[Gro99] L. K. Grover. *Int. J. Theor. Phys.*, 101695, (1999).

[GRSL08] E. M. Gauger, P. P. Rohde, A. M. Stoneham, and B. W. Lovett. *New Journal of Physics*, 10 073027, (2008).

[GSC+10] U. Gerstmann, A. P. Seitsonen, D. Ceresoli, F. Mauri, H. J. von Bardeleben, J. L. Cantin, and J. Garcia Lopez. *Phys. Rev. B*, 81, 195208, (2010).

[Har28a] D. R. Hartree. *Proc. Cam. Phil. Soc.*, 24, 89, (1928).

[Har28b] D. R. Hartree. *Proc. Cam. Phil. Soc.*, 24, 111, (1928).

[HCG+94] D. J. Van Den Heuvel, I. Y. Chan, E. J. J. Groenen, E. J. J. Schmidt, and G. Meijer. *Chem. Phys. Let.*, 231 , 111, (1994).

[HE99] A. Hirsh and M. Prato (Eds.). *Topics in Current Chemistry, vol. 199, Springer Verlag, Berlin, Heidelberg,*, (1999).

[HK64] P. Hohenberg and W. Kohn. *Phys. Rev.*, 136, 864, (1964).

[HLK94] A. Hirsch, I. Lamparth, and H. Karfunkel. *Angewandte Chemie*, 33, 437, (1994).

[HLSW90] A. Henstra, T. S. Lin, J. Schmidt, and W. Wenckerbackh. *Chem. Phys. Lett.*, 185, 6, (1990).

[HM61] C.A. Hutchison and B.W. Mangum. *J. Chem. Phys.*, 34, 908, (1961).

[Hol69] R. W. Holmberg. *J. Chem. Phys.*, 51, 3255, (1969).

[HOYI95] R. Hanaishi, Y. Ohba, S. Yamauchi, and M. Iwaizumi. *J. Chem. Phys.*, 103, 4819, (1995).

[HSC79] D. R Hamann, M. Schluter, and C. Chiang. *Phys. Pev Lett.*, 43, 1494, (1979).

[ICSN05] H. Isobe, A-C Chen, N. Solin, and E. Nakamura. *Organic Letters*, 7, 5633, (2005).

[IET70] M. Iwasaki, B. Eda, and K. Toriyama. *J. Chem. Phys.*, 52, 3837, (1970).

[IFOY96] K. Ishii, J. Fujisawa, Y. Ohba, and S. Yamauchi. 118, 13079, (1996).

[IST+95] M. Iinuma, I. Shake, R. Takizawa, M. Daigo, H. M. Shimizu, Y. Takahashi, A. Masaike, and T. Yabuzaki. *Phys. Lett. A*, 208, (1995).

[Jen07] F. Jensen. *Introduction to Computational Chemistry, Wiley and Sons, Chichester.* (2007).

[JK99] J. A. Jones and E. Knill. *J. Magn. Reson.*, 141,322, (1999).

[JVF71] J. Janecka, H. M. Vyas, and M. Fujimoto. *J. Chem. Phys.*, 54, 3229, (1971).

[JYPB08] S. A. Joyce, J. R. Yates, C. J. Pickard, and S. P. Brown. *J. Am. Chem. Soc.*, 130, 12663, (2008).

[Kan98] B. E. Kane. *Nature*, 393, 133, (1998).

[KBdR+01] K. Kordatos, S. Bosi, T. da Ros, A. Zambon, V. Lucchini, and M. Prato. *J. Org. Chem.*, 66, 2802, (2001).

[Ker80] G. P. Kerker. *J. Phys. C, Solid State Phys.*, 13, 189, (1980).

[KG07] Y. Kanai and J. C. Grossman. *Nano Letters*, 7, 1967, (2007).

[KGTW01] C.W. M. Kay, U. Gromadecki, J. T. Törring, and S. Weber. *Molecular Physics*, 99,1413, (2001).

[KKL88] H. Kurreck, B. Kirste, and W. Lubitz. Electron nuclear double resonance spectroscopy of radicals in solution,new york: Vch publishers. (1988).

[KLMT63] A. V. Kessenikh, V. I. Lushchikov, A. A. Manenkov, and Y. V. Taran. *Sov. Phys. Solid State*, 5, 321, (1963).

[KP76] A. E. W. Knight and C. S. Pamrenter. *Chem. Phys.*, 15 , 85, (1976).

[KS65] W. Kohn and L. J. Sham. *Phys. Rev.*, 140, A 1133, (1965).

[KS84] L. B. Knight and J. Steadman. *J. Chem. Phys.*, 80, 1018, (1984).

[KS88] L. B. Knight and J. Steadman. *J. Chem. Phys.*, 88, 5338, (1988).

[KVM97] C. W. M. Kay, M. Di Valentin, and K. Möbius. *J.Chem.Soc, Perkin Trans.*, 2, (1997).

[KYW+10] G. Kothe, T. Yago, J-U Weidner, G. Link, M. Lukaschek, and T.-S. Lin. *J. Phys. Chem. B*, 114, 14755, (2010).

[LCW97] D. Lidar, I. L. Chuang, and K. B. Whaley. *Phys. Rev. Lett.*, 81, 25942597, (1997).

[Lev08] M. H. Levitt. *Basics of Nuclear Magnetic Resonance, Wiley and Sons, Ltd.*, 2nd Edition, (2008).

[Llo93] S. Lloyd. *Science,*, 261(5128),1571, (1993).

[LMM+92] H. Levanon, V. Meiklyar, A. Michaeli, S. Michaeli, and A. Regev. *J. Phys. Chem.*, 96, 6128, (1992).

[Low78] J. P. Lowe. *Quantum Chemistry, Academic Press, New York, pp 509-519*, (1978).

[LWS+03] X. Li, Y. Wu, D. Steel, D. Gammon, T. H. Stievater, D. S. Katzer, D. Park, C. Piermarocchi, and L. J. Sham. *Science*, 301, 5634, (2003).

[LYP88] C. Lee, W. Yang, and R.G. Parr. *Phys. Rev. B*, 37, 785, 1988.

[MDPC99] C. H. Tseng J. C. Gore A. F. Fahmy T. F. Havel M. D. Price, S. S. Somaroo and D. G. Cory. *J. Mag. Res*, 140,(317), (1999).

[MEHS88] T. Momose, Y. Endo, E. Hirota, and T. Shida. *J. Chem. Phys.*, 88, 5338, (1988).

[MFG+93] M. Matsushita, A.M. Frens, E. J. Groenen, D. Poleuektov, J. Schmidt, G. Meijer, and M.A Verheijen. *Chem . Phys. Lett.*, 214, 349, (1993).

[MHL+05] G.W. Morley, B. J. Herbert, S. M. Lee, K. Porphyrakis, R. Scipion T. J. S. Dennis, D. Nguyen-Manh, J. Van Tol, A.P. Horsfield, A. Ardavan, D.F. Pettifor, J. C. Green, and G. A. D. Briggs. *Nanotechnology*, 16, 2469, (2005).

[Mim65] W. B. Mims. *Proc R. Soc. Lond. A Math. Phys. Sci.*, 283, 452, (1965).

[MMS03] M. Mehring, J. Mende, and W. Schere. *Phys. Rev. Lett.*, 90, 153001, (2003).

[MPL96] F. Mauri, B. G. Pfrommer, and S. G. Louie. *Phys. Rev. Lett.*, 77, 5300, (1996).

[MS75] M.A.El-Sayed. Double resonance and the properties of the lowest excited triplet state of organic molecules. (1975).

[MSW04] M. Mehring, W. Scherer, and A. Weidinger. *Phys. Rev. Lett.*, 93(20), 206603, (2004).

[MTA+06] J. J. L. Morton, A. M. Tyryshkin, A. Ardavan, S. C. Benjamin, K. Porfyrakis, S. A. Lyon, and G. A. D. Briggs. *Nat. Phys.*, 2, 40-3, (2006).

[NBM06] M. J. Sellars N. B. Manson, J. P. Harrison. *Phys. Rev. B*, 74:104303, (2006).

[Nee07] F. Neese. *ORCA An ab Initio, Density Functional and Semiempirical Program Package, version 2.7.0.* (2007).

[NHY+07] A. O. Niskanen, K. Harrabi, F. Yoshihara, Y. Nakamura, S. Lloyd, and J. S. Tsai. *Science*, 316, 5825, 723-7263, (2007).

[NKN+10] P. Neumann, R. Kolesov, B. Naydenov, J. Beck, and F. Rempp. *Nat. Phys.*, 6:24953, (2010).

[NLB+04] A. Nazir, B.W. Lovett, S. D. Barrett, T. P. Spiller, and G. A. D. Briggs. *Phys. Rev. Lett.*, 93, 15, 150502, (2004).

[NMR+08] P. Neumann, N. Mizuochi, F. Rempp, P. Hemmer, H. Watanabe, V. Jacques S. Yamasaki, T. Gaebel, F. Jelezko, and J.Wrachtrup. *Science*, 320, 5881, 1326, (2008).

[Ove53] A. W. Overhauser. *Phys. Rev.*, 92, 411, (1953).

[OW61] D. W. Ovenall and D. H. Whiffen. *Mol. Phys.*, 4, 135, (1961).

[OYOI94] S. Ohkoshi, S. Yamauchi, Y. Ohba, and M. Iwaizumi. *Chem. Phys. Lett.*, 224, 313, (1994).

[PBC+03] E. Pazy, E. Biolatti, T. Calarco, I. DAmico, P. Zanardi, F. Rossi, and P. Zoller. *J. Supercond.*, 16, 383, (2003).

[PBE96] J. P. Perdew, K. Burke, and M. Ernzerhof. *Phys. Rev. Lett.*, 77, 3865, (1996).

[PCD+03] E. Pazy, T. Calarco, I. DAmico, P. Zanardi, F. Rossi, and P. Zoller. *Journal of Superconductivity: Incorporating Novel Magnetism*, 16, 2, (2003).

[Per86] J. P. Perdew. *Phys. Rev. B*, 33, 8822, (1986).

[PGHM07] J. H. Plantenberg, P. C. De Groot, C. J. P. M. Harmans, and J. E. Mooij. *Nature*, 447(7146) 836, (2007).

[Phi58] J. C. Phillips. *Phys. Rev.*, 112, 685, (1958).

[PK59] J. C. Phillips and L. Kleinman. *Phys. Rev.*, 116, 287, (1959).

[PM01] C. J. Pickard and F. Mauri. *Phys. Rev. B*, 63, 245101, (2001).

[PM02] C. J. Pickard and F. Mauri. *Phys. Rev. Lett.*, 88, 086403, (2002).

[PW86] J. P. Perdew and Y. Wang. *Phys. Rev. B*, 33, 8800, (1986).

[PZ81] J. P. Perdew and A. Zunger. *Phys. Rev. B.*, 23, 5048, (1981).

[RGM95] A. Regev, D. Gamliel, and V. Meiklyar. *J. Chem. Phys.*, 102, 9457, (1995).

[RMPF05] S. Rossano, F. Mauri, C. J. Pickard, and I. Farnan. *J. Phys. Chem. B*, 109, 7245, (2005).

[RZB09] M. Radmark, M. Zukowski, and M. Bourennane. *Phys. Rev. Lett.*, 103(15), 150501, (2009).

[SB92] K. Schwarz and P. Blaha. *Z. Naturforsch. Teil A*, 47, 197, (1992).

[SBR+11] S. Simmons, R. M. Brown, H. Riemann, N. V. Abrosimov, P. Becker, H. J. Pohl, M. L. W. Thewalt, K. M. Itoh, and J. J. L. Morton. *Nature*, 470, 69, (2011).

[SFG03] A. M. Stoneham, A. J. Fisher, and P. T. Greenland. *J. Phys.: Condens. Matter*, 15, 27,447, (2003).

[SFK+10] M. Schaffry, V. Filidou, S. D. Karlen, E. M Gauger, S. C. Benjamin, H. L. Anderson, A. Ardavan, G. A. D. Briggs, K. Maeda, K. B. Henbest, F. Giustino, J. J. L. Morton, and B. W. Lovett. *Phys. Rev. Lett.*, 104, 20, 2010.

[Sho95] P. W. Shor. *Phys. Rev. A.*, 52, 2493, (1995).

[Sho99] P. Shor. *Proceedings of the 35th Annual Symposium on Foundations of Computer Science*, (1999).

[SJ01] A. Schweiger and G. Jeschke. *Principles of Pulse electron paramagnetic resonance*, Oxford University Press, (2001).

[SLG11a] M. Schaffry, B. W. Lovett, and E. M. Gauger. *arXiv:*, 1106.4958, (2011).

[SLG11b] M. Schaffry, B. W. Lovett, and E. M. Gauger. *manuscript in preparation*, (2011).

[SM08] W. Scherer and M. Mehring. *J. Chem. Phys.*, 128(5):052305, (2008).

[SS06] S. Stoll and A. Schweiger. *J. Magn. Reson.*, 178, 42, (2006).

[Ste95] A. M. Steane. *Phys. Rev. Lett.*, 52, 2493, (1995).

[Ste97] A. M. Steane. *App. Phys. B*, 64(6), 623, (1997).

[SUN94] P. R. Surjan, L. Udvardi, and K. Nemeth. *J. Mol. Struct.(Theochem)*, 311, 55, (1994).

[SYalW84] D-J. Sloop, H.-J Yu, and T.-S. Lin andS l. Weirssman. *J.Chem Phys.*, 75, 3746, (1984).

[SYL74] T. Shiga, H. Yamaoka, and A. Lund. *Z. Naturforsch.*, 29a, 653, (1974).

[SYT07] L. Shao, J. R. Yates, and J. Titman. *J. Phys. Chem. A*, 111, 13126, (2007).

[SZC96] A. Sassara, G. Zerza, and M. Chergui. *Chem. Phys. Let.*, 261, 213, (1996).

[TCT+10] E. Togan, Y. Chu, A. S. Trifonov, L. Jiang, J. Maze, L. Childress, M. V. G. Dutt, A. S. Soerensen, P. R. Hemmer, A. S. Zibrov, and M. D. Lukin. *Nature*, 466(7307), (2010).

[THSS92] M. Terazima, N. Hirota, H. Shinohara, and Y. Saito. *Chemical Physics Letters*, 195(4):333 – 338, (1992).

[TM91] N. Troullier and J. L. Martins. *Phys. Rev. B*, 43, 1993, 1991.

[TPB07] L. Truflandier, M. Paris, and F. Boucher. *Phys. Rev. B*, 76 , 035102, (2007).

[TTT04] K. Takeda, K. Takegoshi, and T. Terao. *The physical society of Japan*, 73, 8, 2313, (2004).

[TYH85a] M. Terazima, S. Yamauchi, and N. Hirota. *Chemical Physics Letters*, 120, 321, (1985).

[TYH85b] M. Terazima, S. Yamauchi, and N. Hirota. *The Journal of Chemical Physics*, 84, 3679, (1985).

[Van90] D. Vanderbilt. *Phys. Rev. B*, 41, 7892, (1990).

[VdBS79] P.J.F. Verbeek, H.J. den Blanken, and J. Schmidt. *Chem. Phys. Letters*, 60, 358, (1979).

[VDS78] P. J. F. Verbeek, A. I. M. Dicker, and J. Schmidt. *Chem. Phys. Letters*, 56, 585, (1978).

[VKGM96] M. Di Valentin, C.W. M. Kay, G. Giacometti, and K. Möbius. *Chem. Phys. Let*, 248, 434, (1996).

[VKL99] L. Viola, E. Knill, and S. Lloyd. *Phys. Rev. Lett.*, 82 241721, (1999).

[WA05] F. Weigend and R. Ahlrichs. *Phys. Chem. Chem. Phys.*, 95, 2571, (2005).

[WB93] C. Van De Walle and P. E. Blöchl. *Phys. Rev. B*, 47, 4244, (1993).

[WF61] R. E. Watson and A. J. Freeman. *Phys. Rev.*, 123, 2027, (1961).

[WOL+91] M. R. Wasilewski, M. P. Oneil, K. R. Lykke, M. J. Pellin, and D. M. Gruen. *J. Am. Chem. Soc.*, 113, 2774, (1991).

[Woo98] W. K. Wootters. *Phys. Rev. Lett.*, 80, 2245, (1998).

[YLKL07] T. Yago, G. Link, G. Kothe, and T. Lin. *The journal of chemical physics*, 127 114503, (2007).

[YTHR05] O. V. Yazyev, I. Tavernelli, L. Helm, and U. Röthlisberger. *Phys. Rev. B*, 71, 115110, 2005.

[YWL+07] T. Yago, J. U. Weidner, G. Link, T.-S. Lin, and G. Kothe. *Chemical Physics Letters*, 438, 351, (2007).

[Zan99] P. Zanardi. *Phys. Lett. A*, 258, 77-82, (1999).

[ZPA09] E. Zurek, C. J. Pickard, and J. Autschbach. *J. Phys. Chem. A*, 113, 4117, (2009).

[ZR97] P. Zanardi and M. Rasetti. *Phys. Rev. Lett.*, 79, 33063309, (1997).

[ZZF00] P. Zanardi, C. Zalka, and L. Faoro. *Phys. Rev. A*, 62, 030301, (2000).